POLITECNICO
MILANO 1863

Politecnico di Milano
Department of Energy
Doctoral Programme in
Energy and Nuclear Science and Technology

Investigation of advanced carbon-based films for application in radiation detectors

Doctoral Dissertation of:
Federica Inzoli

Supervisors:
Prof. Matteo Passoni
Dott. Francesco Ghezzi

Tutor:
Prof. Carlo E. Bottani

The Chair of the Doctoral Programme:
Prof. Carlo E. Bottani

Year 2017 - Cycle XXX

Abstract

Diamond detectors are attracting great attention lately, because of their outstanding performance in harsh radiation environments such those of fusion facilities and particle accelerators for high energy physics experiments. However, their production cost competitive on a large scale is still limited by some technological issues. First, the artificial synthesis of the material, that nowadays still represents a widely investigated topic. Growing diamond is difficult, and this is even more true for the single-crystal material, that needs specific tailored process conditions in order to avoid crystallographic defects. Additionally, only few substrates can be used for single-crystal diamond deposition. Polycrystalline diamond is a relatively cheaper material, easier to be produced, having less requirements on the choice of the substrate material and deposition conditions. Particularly, polycrystalline diamond with grain size less than 100 nm (i.e. nanocrystalline diamond) are of interest for several applications (from the mechanical to the biomedical one), not just for the nuclear field. However, the lower crystalline quality influences the properties of the polycrystalline (and thus nanocrystalline) diamond-based device, resulting in worse performance. This fact widely justifies the research activity devoted to completely understand the nucleation and growth process of nanocrystalline diamond in order to produce a cheaper material (than the single-crystal one) but with a tailored structure such that outstanding properties comparable to those of a single-crystal diamond device can be obtained. Besides the material production, the other main features influencing the detector performance are i) the fabrication of optimized electrodes and ii) a complete knowledge of the device performance under irradiation, since diamond behavior in harsh radiation environments for which is thought to be employed is not well known.

The main goal of this thesis is to explore all the relevant issues highlighted above. Particularly, the investigation of nanocrystalline diamond growth dynamics was carried on with an experimental approach using a direct-current micro-plasma deposition set-up: the focus was on the early stages of growth on different substrate materials, that were not pre-treated in order to investigate the growth on the native elements. Deposition parameters were optimized and a detailed characterization was performed, finding that the dynamics of the early stages of diamond growth is governed by the spontaneous deposition of a graphitic layer prior to diamond growth. Also, an experimental activity devoted to fabricate graphitic electrodes on polycrystalline diamond substrate was started. Finally, the investigation of diamond detector modifications in the crystalline structure after α and neutrons irradiations was performed, with a methodological approach aiming at introducing a characterization strategy suitable for the goal of the work.

The main findings of this Ph.D thesis work are of interest for the understanding of artificial nanocrystalline diamond synthesis on different substrates, as well as useful for addressing in a methodological and rigorous way some delicate aspects influencing the device performance.

Sinossi

I rivelatori al diamante sono oggetto di studio da parte della comunità scientifica per via delle loro incomparabili performance in campi di radiazione particolarmente intensi e peculiari, come quelli prodotti dagli impianti finalizzati allo studio della fusione nucleare o vicino agli acceleratori di particelle per esperimenti di fisica delle alte energie. Tuttavia, la loro produzione su larga scala e ad un costo competitivo è limitata da alcuni fattori tecnologici. Innanzitutto, la sintesi del materiale, che ad oggi rappresenta uno degli aspetti più investigati. Crescere diamante artificiale è difficile, e questo è vero a maggior ragione per il diamante monocristallino, che necessita di condizioni di processo specifiche per evitare difetti cristallografici. In aggiunta, solo pochi materiali possono essere impiegati come substrati. Il diamante policristallino è un materiale relativamente più economico e più semplice da fabbricare, dal momento che ci sono meno aspetti stringenti riguardo la scelta del materiale substrato e delle condizioni di processo. In particolare, il diamante policristallino con dimensione dei grani inferiore a 100 nm (cioè nanocristallino) è interessante per molte applicazioni (da quelle meccaniche a quelle biomediche), non solo per il settore nucleare. Tuttavia, la minor qualità cristallina influenza le proprietà del rivelatore policristallino (e quindi anche nanocristallino), dando come risultato minori performance. Tale questione giustifica ampiamente quel ramo di ricerca scientifica volto a comprendere completamente i processi di nucleazione e crescita del diamante nanocristallino, allo scopo di produrre un materiale più economico (rispetto al monocristallo di diamante) ma con una struttura cristallina ben precisa e in grado, a sua volta, di dare al materiale delle performance comparabili a quelle del rivelatore monocristallino. Oltre alla fabbricazione del materiale di base, gli altri aspetti che principalmente influenzano le performance del rivelatore di particelle sono i) la fabbricazione di contatti ottimizzati e ii) una comprensione completa delle performance del diamante a fronte dell'irraggiamento, dal momento che il comportamento del rivelatore al diamante in campi di radiazione intensi per i quali è oggetto di studio, non è completamento noto.

Il principale obiettivo di questa tesi è esplorare gli aspetti rilevanti menzionati nel precedente paragrafo. In particolare, lo studio delle dinamiche di crescita di diamante policristallino è stato condotto con un approccio sperimentale, utilizzando un set-up di deposizione al plasma noto come microtorcia in corrente diretta: il focus è stato sui primi stadi di crescita su diversi materiali substrato, non sottoposti a pre-trattamenti per studiare la crescita sull'elemento nativo. I parametri di deposizione sono stati ottimizzati per lo scopo del lavoro ed è stata effettuata una caratterizzazione dettagliata dei campioni, osservando come la dinamica dei primi stadi di crescita sia governata dalla deposizione spontanea di un layer grafitico, che avviene prima della crescita del diamante. Inoltre, si è cominciata un'attività sperimentale volta a investigare la possibilità di fabbricare contatti grafitici su substrati di diamante policristallino. Infine, è stato condotto uno studio sulle modificazioni della struttura cristallina di un rivelatore al diamante a seguito di irraggiamenti con α e neutroni, con un approccio metodologico volto ad introdurre una strategia di caratterizzazione adatta agli scopi del lavoro.

I principali risultati di questo progetto di dottorato sono interessanti per la comprensione dei meccanismi di sintesi artificiale di diamante nanocristallino su diversi substrati, come pure sono utili per comprendere come indagare in modo metodologico e rigoroso alcuni delicati aspetti concernenti le performance del rivelatore di particelle.

Contents

III Diamond detectors performance: an investigation of electrodes fabrication and irradiation

Preface

Diagnostic and measurement of complex radiation fields are extremely important, not just for safety issues, but also to control and characterize them, in order to acquire a deeper understanding of main reactions involved. Nowadays, with fusion facilities and high particle experiments (such as LHC) becoming a reality, the comprehension and control of such radiation environment as the one that these facilities produce is a subject of great interest. For this reason, performing radiation detectors are required, able to withstand the extreme conditions and irradiation damages induced by harsh radiation fields. Particularly, when ionizing radiations are involved, solid-state detectors based on silicon technology represent a widely used solution, thanks to their desirable properties of high energy resolution, compact size and relatively fast timing characteristics. However, when a complex and intense ionizing radiation field is involved (e.g. in fusion reactors), still a lack of performance is found, due to material degradation when withstanding such kind of harsh radiation environment. This leads to a decrease in the overall detector performance. For this reason, alternative solutions are under investigation, looking for innovative and more performing materials. In this framework, diamond solid-state detectors seem to represent the most suitable for this case, thanks to the outstanding properties of this material conferring it a high radiation hardness and excellent detection capabilities. However, for being truly competitive, some issues must be factual data. First, the material must be available on a large scale and at affordable costs. Second, the device fabrication must be properly optimized, which means either the electrodes and the electronic chain must be able to acquire the event coming from the diamond - radiation interaction, amplify it and produce a measurable signal. Finally, the device behavior under peculiar irradiation conditions such those mentioned above must be verified and known.

Regarding the material, being diamond the metastable phase of carbon, its artificial synthesis is challenging. Suitable substrates and specific tailored deposition conditions are required. Some issues still need to be overcome in order to completely understand the dynamics of growth, especially in the first stages, being the nucleation of the first diamond grains on non-diamond substrates a process other than simple and spontaneous. Controlling the whole synthesis process means being able to grow diamond with tailored features either at a microscopic and macroscopic scale. First attempts were made in the early 1970s, and since then many scientists around the world devoted lots of efforts in understanding the mechanisms behind the nucleation and growth processes of diamond, apparently not governed by standard rules of thermodynamics. Nowadays many questions have been addressed, but some open points are still found, and diamond still represents an expensive material not available at a large-scale. Either single-crystal and polycrystalline diamond can be used for radiation detection and, despite the lower performance of the polycrystalline material (having more defects in its crystalline structure), the less expensive processes required for its synthesis with respect to the single-crystal one justify the interest in such structure. Depending on the grain size, different kind of polycrystalline diamond can be synthesized, and nowadays nanocrystalline diamond (with grain size less than 100 nm) are attracting great attention for a wide range of applications, not just for nuclear purposes. Besides the material itself, as already introduced, also the whole device fabrication is essential to obtain a performing technology. Particularly, the creation of proper electrodes with a ohmic behavior is essential, since they are responsible for an efficient collection of charge carriers created after diamond - radiation interaction and bringing information about the incoming radiation. Several solutions have been adopted, mainly involving metallic conductive alloys, but in the last years the idea of an all carbon-based detector is earning much attention, since graphite is the stable allotropic phase of carbon, easy to be deposited and with excellent electrical properties. Finally, diamond detectors are thought for harsh radiation environments, where common silicon-based technology shows to be unsuitable for such complex radiation fields detection and because of the need of changing too often the detectors (due to material degradation affecting and lowering the detection performance). However, being diamond detector a relatively new technology, its behavior in such peculiar and intense radiation environments is not completely known and understood. For instance, a *polarization effect* has been recorded under α and neutron irradiations, decreasing the device detection capability.

This PhD thesis aims to explore all these relevant issues related to the diamond detector technology with a material science approach. It is an experimental work that addresses two main subjects. The first one is devoted to the investigation of the dynamics of the first stages of growth of nanocrystalline diamond on different substrate materials, making use of laboratory equipments for diamond deposition and characterization. The second one regards features related to the diamond detector. Particularly, introductory and investigative experiments were made with the goal of producing graphitic contacts on polycrystalline diamond substrates suitable to be used as diamond detectors. Additionally, a preliminary and methodological study was made in order to propose a characterization strategy aiming at understanding the *polarization effects* observed in diamond detector during α and neutron irradiation. The present doctoral dissertation is organized in four parts, as follow:

I. Introduction and aims. In the first part, the basic concepts underlying the diamond material, its unbearable properties and all the relevant technological applications are presented, with focus on the application of polycrystalline diamond as radiation detectors. Some important features related to diamond particle detectors such as those mentioned above (i.e. electric contacts and behavior under irradiation) are introduced and discussed. Also, the artificial synthesis of polycrystalline diamond is presented. An overview of the main deposition techniques adopted for polycrystalline diamond synthesis is given, with specific focus on the direct-current micro-plasma set-up (DC-μP) used in this work. Additionally, common diamond characterization techniques are presented, where Raman spectroscopy worths a special mention, being the characterization tool mainly employed in this work. Finally, the main goals of this thesis work are presented.

II. Growth of nanocrystalline diamond (NCD) with DC-μP. This second part is dedicated to introduce the methodology adopted for the investigation of NCD growth dynamics on several substrate materials, and the most important results obtained from this study. Additionally, a part of the work was devoted to produce diamond films with the DC-μP set-up, in order to evaluate the possibility of producing diamond samples with relevant thickness for diamond detector development.

III. Diamond detectors performance: an investigation of electrodes fabrication and irradiation effects. In this part, graphitic electrodes fabrication and diamond behavior under α and neutron irradiation are the two topics investigated. The methodology used is presented, with relevant results. For graphitic electrodes production, a procedure is individuated, where carbon films with amorphous structure are firstly deposited by the pulsed laser deposition technique and subsequently graphitized; both thermal and laser annealing treatments are investigated. For diamond behavior under irradiation, single-crystal diamond detectors are irradiated with α and fast neutrons. With a material science approach, a methodological and systematic characterization strategy of samples able to be a valuable tool for the comprehension of some issues related to irradiation effects is presented.

IV. Conclusions and perspectives. Finally, this part presents the main conclusions that can be drawn from this PhD thesis, together with some possible future developments of the topics here addressed.

The original contents of this PhD thesis have led to the publication of the following peer-reviewed papers on specific scientific international journals:

- F. Inzoli, D. Dellasega, V. Russo, R. Caniello, C. Conti, F. Ghezzi and M. Passoni, *Nanocrystalline diamond produced by direct current micro-plasma: investigation of growth dynamics*, Diamond and Related Materials 74 (2017), 212-221.
- F. Inzoli, D. Dellasega, V. Russo, F. Ghezzi and M. Passoni, *Early stages of diamond growth on substrates with different carbon diffusivity*, Diamond and Related Materials 80 (2017), 69-75.

Also, the subject of this thesis was presented in several international conferences and summer schools, listed below:

- F. Inzoli, *Development of advanced carbon-based film for application in neutron detectors*, 54th Summer School on Atoms and Plasmas in Super-Intense Laser fields, Erice (Italy), July 2015. Poster presentation.
- F. Inzoli, F. Ghezzi, R. Caniello, D. Dellasega, V. Russo and M. Passoni, *Nucleation of diamond films grown by direct-current micro-plasma technique*, 26th International Conference on Diamond and Carbon Materials, Bad Homburg (Germany), September 2015. Poster Presentation.
- F. Inzoli, *Development of advanced carbon-based films for applications in neutron and photon detectors*, PhD Fusenet event, Prague (Czech Republic), November 2015. Poster Presentation.
- F. Inzoli, *Development of diamond films for application in neutron detectors*, Summer School on Neutron Detectors and Related Applications, Riva del Garda (Italy), July 2016. Poster presentation.
- F. Inzoli, F. Ghezzi, R. Caniello, D. Dellasega, V. Russo and M. Passoni, *Nucleation and growth of polycrystalline diamond films produced by direct-current micro-plasma technique*, 27th International Conference on Diamond and Carbon Materials, Montpellier (France), September 2016. Oral Presentation.
- F. Inzoli, F. Ghezzi, R. Caniello, D. Dellasega, V. Russo and M. Passoni, *Nanocrystalline diamond produced by direct-current micro-plasma: dynamics of the early stages of growth*, 11th New Diamond and Nano Carbons Conference, Cairns (Australia), May 2017. Oral Presentation.

This doctoral thesis work was born from a collaboration between the Micro- and Nanostructured Materials Laboratory of the Department of Energy of Politecnico di Milano (Milan, Italy) and the Institute of Plasma Physics of the National Research Council (Milano, Italy). This work was supervised by Prof. Matteo Passoni (Politecnico di Milano) and Ing. Francesco Ghezzi (Institute of Plasma Physics) and was carried on with the collaboration of Dott. Valeria Russo (Politecnico di Milano), Dott. David Dellasega (Politecnico di Milano), Dott. Luca Giacomelli (Institute of Plasma Physiscs) and Prof. Marco Tardocchi (Institute of Plasma Physics).

Part I

Introduction and aims

Chapter 1

Diamond film: a promising material for radiation detectors application

1.1 Introduction

Over the last few decades, the material science earned much importance and raised increasing interest for the scientific development of functioning, efficient and cost effective technologies, in all fields. Its unique ability relies in the capability of binding materials properties with functionality, creating always new performing materials, not just single-crystal and polycrystalline films, but also coatings with precise and controlled nanostructure, preserving or even improving properties typical of the bare material. The approach is unmatched and completely new: tuning their atomic properties to control the macroscopic overall performance.
In this framework carbon-based materials started to be considered for different applications, thanks to their interesting properties that allow to design them for every kind of requirement [1, 2]. Indeed, depending on the hybridization of the carbon atoms bonded together, three different allotropes can be obtained, with completely different properties:

- the sp^3 hybridization gives rise to a tetrahedral structure: this is the case of diamond;

- the sp^2 hybridization is responsible for a planar structure, that for instance can be found in graphite, fulleren and carbon nanotubes (CNTs);

- the sp hybridization, that in turn gives place to a linear structure, metastable exotic form nowadays synthesized only in laboratory.

The main feature of these structures is that they can present completely different properties, and thus technological applications. Indeed, where diamond is for instance a very hard material and with the highest band gap (being so an insulator), on the contrary graphite is soft and a good electric conductor at room temperature. Particularly, diamond is becoming even more interesting in the scientific scenario, because showing properties that are outstanding among all materials. For years considered fascinating in the form of gems for the luxury industry, nowadays the possibility of synthesizing different structures of this material even in the form of coating opens up to an incredible range of applications [2].
The following chapter will focus especially on this topic. First of all, in section 1.2, an overview of the possible applications of diamond films is provided, in order to elucidate the outstanding properties of this material and to justify the global interest in its production. Then, in section 1.3, the specific case of the application as a radiation detector is explained, discerning from the case of single-crystal diamond (SCD) and polycrystalline diamond (PCD), and showing why it is considered as one of the best candidates for measurements in the nuclear fields. Finally, in section 1.4, the application of diamond detectors in the nuclear fusion environment is presented, being this the driving force of the development of this material as a radiation detector.

1.2 Overview of applications of diamond films

All possible applications of diamond in such various fields are strongly motivated by its unique properties. Indeed its chemical structure, with atoms arranged in a tetrahedral configuration (see fig. 1.1) with very strong covalent bonds (347 kJ mol^{-1}), leads to special mechanical, electrical, structural and optical properties. Considering the ideal and peculiar case of a natural SCD as a reference, for any given property of a

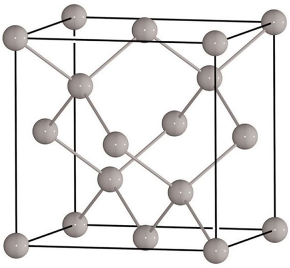

Figure 1.1: *Diamond crystalline structure.*

material the value associated with diamond almost always represents an extremity [2, 3]. From a mechanical point of view, it is extremely hard (around 90 GPa), with a low friction coefficient and the highest Young modulus (1.2 x 10^{12} N m^{-2}). Additionally, it is chemical inert, it possesses the highest thermal conductivity (2 x 10^{3} W m^{-1} K^{-1} at room temperature) with a very low thermal expansion coefficient (0.8 x 10^{-6} K^{-1}), and the highest band gap (5.47 eV). From an optical point of view it has a broad transparency from the deep UV to the far IR region of the electromagnetic spectrum. Last but not the least, diamond electrical properties are still countless. Indeed, diamond has a high carrier mobility (2400 cm^{2} V^{-1} s^{-1} for electrons, 2100 cm^{2} V^{-1} s^{-1} for holes), breakdown field ($\sim$ 2 x 10^{7} V cm^{-1}), electrical resistivity (can reach 10^{15} Ω cm) and saturation velocity (2 x 10^{7} cm s^{-1} for electrons and 10^{7} cm s^{-1} for holes), it is an electrical insulator but can be doped thus becoming a wide band gap semiconductor. Of course moving from the natural SCD to the synthetic SCD and then PCD film, all these values can slightly change, depending on the microstructure of diamond itself. However, it is in this sense that material science proves to be an efficient tool: the possibility of producing diamond in the form of film or coating still able to preserve bulk diamond properties [4], but more versatile than the single-crystal material, would allow not only to tune its properties during the growth thanks to an appropriate deposition process, but also to cut down the high costs typical of this material.

In light of these observations, applications of diamond are innumerable. For its mechanical properties and chemical inertness, it is a perfect candidate for cutting tools and wear resistance coatings. Being simultaneously an excellent thermal conductor and electrical insulator it seems so much natural its use for a variety of thermal management applications, such as heat spreaders for high-power electronic and opto-electronic devices or substrate material for multi-chip modules. Thanks to its optical properties, diamond finds applications also in optics, for instance as a free-standing plate for use as an UV or IR window in harsh environments. For its bio-compatibility and the possibility to have its surface functionalized, diamond is also an excellent candidate in biomedical applications (e.g. drug and protein delivery, bone and dental implants, cancer therapy etc.). Last but not the least, for its electrical properties it is clear why diamond is considered the ideal candidate for high-power and high-frequencies electronic devices. To date, some diamond-based devices have already been developed such as transistors, high-temperature diodes, electron emitters in flat-panel displays and solid-state detectors. Particularly, among all the possible interesting applications mentioned, a strong focus is nowadays on the idea of using diamond as a "wide band gap semiconductor" for radiation measurements, as shown in the following.

1.3 Diamond detector: a novel wide band gap semiconductor for radiation measurements

Among the above mentioned applications of diamond, great attention is paid on the possibility of using this material as a particle detector in harsh radiation environments [5–7]. Belonging to the family of solid-state detectors, its design is similar to that of conventional semiconductor detectors. A schematic of the configuration is depicted in fig. 1.2.

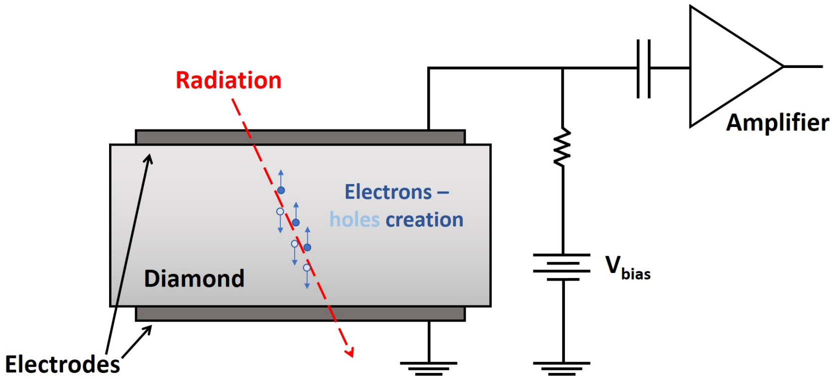

Figure 1.2: *Schematic sketch of a typical solid-state diamond detector: the active volume of the material (i.e. the diamond) is closed between two planar electrodes that, in turn, are connected to the electronic chain. Also, a depiction of the interaction with ionizing radiation is represented.*

Being the general needs the measurement and quantification of an electric signal derived from the interaction with an incoming radiation, it is composed by a layer of diamond, i.e. the active volume in which the interaction with the radiation occurs, with variable thickness, closed between two electrodes, whose function is collecting the charge carriers created by the diamond - radiation interaction. To be thorough, this is not the only electrode configuration possible, depending on the electrode material, as will be shown later. The electrodes are linked to an electronic circuit that acquires the carriers creating a current and translates the signal into information about the measured radiation. Both diamond synthesis and electrodes fabrication are fundamental for achieving an efficient device.

Generally speaking, its detection properties are globally better than that of common silicon technology. The low read-out noise due to the low leakage current (high band gap), the fast signal collection time due to the high electron and hole mobilities and the high radiation hardness (with respect to silicon technology) due to the very high knock-on energy (up to 50 eV for diamond, vs. 15 eV for silicon) are just some of its strengths for application in severe radiation fields. Moreover, being tissue-equivalent (atomic number Z = 6), diamond is a perfect material for radiation dosimetry in medical applications. For these reasons, in the last years several laboratories around the world are programming dedicated experiments for testing diamond detectors and improve both performances and cost production. Both SCD and PCD films can be used for radiation detector applications, as will be elucidated later.

In light of these considerations, the global interest for such technology is fully justified. In the last years indeed, the scientific development of high-energy physics experiments such as the Large Hadron Collider (LHC) where hadron fluences of $\sim 10^{15}$ cm^{-2} are expected, or in future fusion facilities where a neutron flux of about 10^{24} cm^{-2} s^{-1} is foreseen in the most critical regions of the reactor, pointed out that a novel technology is essential, to face the extremely severe radiation environments and to monitor them [8]. Common solid-state detectors made of semiconductor materials (i.e. silicon technology) function very well in relatively low-radiation environments, being not radiation hard. A lot of efforts have been made in engineering them to broaden their field of application, but still limits in high-radiation environments are found. On the contrary, diamond seems to offer a valuable alternative for such kind of application.

1.3.1 Diamond – radiation interaction

Being a solid-state detector, diamond can be used for measurements of ionizing radiation as well as UV, γ-ray and neutrons [9]. Regarding ionizing radiations such as α, β or electrons, the main interaction channel relies on the excitation power of the incoming radiation, able to create electron - hole pairs in the active volume of the material. Through an electric field and conveniently designed electrodes, these pairs can be collected and measured: their number is linked to the number of incoming ionizing particles. For what concern UV and γ-rays indeed, exploiting the correlation between photo-current and dose equivalent, due to the low Z of diamond, Compton scattering is the predominant interaction channel, even at energies as low as 20 keV [10]. Electrons generated by Compton carry a small fraction of the photon energy, but large resistivity of diamond gives rise to very low dark currents and allows the measurements of very low photo-currents. Finally, in common with γ-rays, neutrons carry no charge and therefore can not interact by means of the Coulomb force: their interaction is directly with the nuclei of the detector. As a result of this interaction, the neutron path and energy can either slightly be influenced (elastic scattering), or significantly change in energy and direction (inelastic scattering) or even the neutron can disappear and be replaced by secondary radiation (nuclear interaction). The relative probabilities of the various kind of neutron interactions are strongly dependent upon the neutron energy, see fig. 1.3 [11]. Since with elastic or inelastic interactions neutron loses energy in steps and may get scattered out of the detector without losing all of its energy, nuclear reactions in which neutron is fully absorbed and resulting charged particles (with relatively very small range in detector volume) can be detected are preferred.

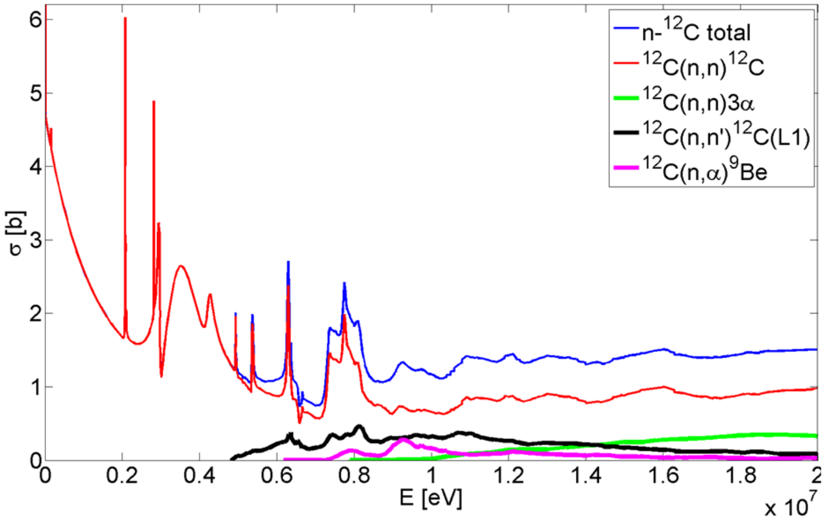

Figure 1.3: *Cross sections of various interaction processes of neutrons with carbon as function of neutron energy [12].*

However, despite the many appealing properties, diamond detectors are not free of drawbacks, that can be improved with a dedicated manufacturing work on the material, in order to enhance the performance. Few examples of limits in the use of diamond detectors will be shown in the following.

Structural damage under neutron irradiation

Among the possible radiations, neutrons are probably the most difficult to be detected. Having no charge, their path can not be controlled with magnetic fields and they do not interact with the Coulombian force. Their interaction is mainly with the nuclei and, depending on the incident energy, they can displace atoms from their lattice position, creating the so-called *displacement-per-atom* (DPA). In general, if a neutron have sufficient energy to dislocate atoms from their position, then a sequence of lattice defects in the materials can be created, i.e. vacancy (that can be either mono or di-vacancy), dislocations, interstitials, dumbbell-type defects, etc [13–15]. Having diamond a minimum average energy of 43 eV needed to create a single vacancy-interstitial, thermal neutrons do not have a noticeable effect [16]. On the contrary, irradiation with fast neutrons leads to a change in the material crystalline structure resulting in enbrittlement and material properties degradation. Additionally, this permanent damage can further worsen the device detection properties, due to the arising of a *polarization effect*, as will be explained in the next section. Finally, for the specific case of diamond, being the metastable form of carbon, a transition to sp^2 hybridization can be promoted, inducing the graphitization of the material. All these effects must be taken into account when considering the use of diamond for radiation measurements in intense neutron fields. Indeed, even if diamond is radiation hard with respect to other semiconductor devices, prolonged used of this material under irradiation can affect the overall detection performances.

Polarization effect under α and fast neutrons irradiation

Diamond detectors are known to be subjected to the *polarization effect*, a space charge stability issue caused by defect concentrations within the material [17, 18]. Generally speaking, the interaction of diamond with ionizing radiation results in the formation of charge carriers in the detector. Under the presence of an electric field, these charges start drifting to the electrodes, and can be either collected thus producing a measurable signal, or be lost because of the progressive filling of deep levels in the band gap, causing space charge buildup. This last effect in turn leads to a change in the space charge distribution: if the rate of charge trapping is grater than the rate of detrapping, an internal electric field distorting the actual applied field is created. The net result is a decrease in charge collection efficiency during the irradiation. Either α particles and fast neutrons are responsible for such effect. For the specific case of α particles, being ionizing radiation with a reduced mean free path ($\approx 12\ \mu$m in diamond for $E_\alpha = 5.5$ MeV [19]), there is a *localized* charge carriers generation near the surface (and thus near the electrodes) of the detector. A localized reduction of the electric field is obtained, in turn decreasing the local charge drift velocity. This implies a reduction in the pulse height due to the increased probability of trapping. With fast neutrons, a *uniform* trapping occurs, since charge carrier creation happens throughout the material [20]. Indeed, as a result of neutrons interaction with carbon, also ^{4}He and Be nuclei are produced, that in turn produce displacements and high ionizing tracks when moving throughout the diamond film. Since at the end of any recoil range non-ionizing events are prevailing, in such a way agglomerates of defects are created. Particularly, being ^{4}He bubbles not mobile, they affect permanently the detection performance [16]. The charge buildup is thus diluted throughout the material. Subsequently, for stable operations, an increase in the applied electric field to compensate the space charge buildup is required [20]. As can be deduced, this effect is dependent on the concentration of excitations within the detector: for this reason is more evident with α particles, creating a large amount of charge carriers near the surface of the detector, but devices can suffer from this effect even for more penetrating neutrons creating, after the interaction with diamond nuclei, secondary ionizing particles. Also, on the contrary of α particles, neutrons create a permanent damage in the diamond crystalline structure, and this influences the *polarization effect* duration. Additionally, being the detrapping time dependent upon both the temperature and the energetic location of the trap within the material band gap [21], for a wide band gap material as diamond is, the deep level trap energy value can be quite large (even higher than 0.7 eV): this can result in long detrapping time at room temperature. To avoid this effect, some solutions have been investigated. As it is true that applying a bias during irradiation starts the polarization, at the same time removing the bias has proved to recover the detector, due to carrier retrapping and neutralization rather than to detrapping [22], and the same was observed applying reverse bias [23]. Also, light illumination with visible or near-visible wavelength can depolarize the detector, since light provides sufficient energy to depopulate traps [24], and thermal annealing around 500 °C has proved to restore the detector too [16]. However, all these solutions are temporal, since the *polarization effect* restarts as the irradiation and bias are imposed again on the material. Alternatively, a *priming process* can be exploited to stabilize the *polarization effect*, that consists of irradiating the detector to high doses such that electrons and holes created are captured by deep level traps [25, 26]. Being the trapped charges immobile for relatively long time, stable responses can be obtained. However, in such way only deep levels are occupied, and the *polarization effect* due to shallow traps is still present.

1.3.2 Single-crystal diamond detectors vs. polycrystalline diamond detectors

In the diamond detector technology two different kind of diamond detectors can be identified: single-crystal diamond detectors (SDDs) and polycrystalline diamond detectors (PDDs). Both detector types have advantages and disadvantages, depending on the use. The main difference relies in the crystalline quality of the material, that in turn influence the general performance of the device. SDDs are usually made of either natural or synthetic single-crystal diamond and, by virtue of their nature, are free of crystallographic defects in their active volume: this implies outstanding charge collection properties and efficiency. However, limits in their fabrication and availability are found, that in turn influence the cost: natural diamond is indeed rare and expensive, whereas synthetic single-crystal diamond impose several strict requirements on the production process, in order to obtain crystalline perfection. Moreover, their fabrication in large size with variable thickness is still an issue. However, if small area devices are acceptable, the extraordinary energy resolution features of SDDs can make them perfect candidate for monitoring harsh radiation environments such as the one found near particle accelerators or fusion facilities, where the plasma diagnostic is crucial [27, 28]. On the other side, PDDs can represent a valuable alternative: unless having by nature many grain boundaries and defects in their active volume limiting the charge collection efficiency (charge carriers bringing radiation information can indeed be trapped in these defects), less requirements on the fabrication process are found, thus making them available at a large scale with a cost effective process [29]. Additionally, PDDs show good timing resolution and can be successfully used as position sensitive devices [30], even if energy resolution performances are not outstanding: this makes them suitable for a range of applications such as medical dosimetry and particle physics tracking where the limited spectroscopic performance is not crucial [31]. Moreover, as coatings they can be designed in large size wafers with a variable thickness, surpassing the limitations imposed by SDDs.

In light of these observations, the strong and growing interest in PDDs fabrication is easily justified: the possibility of producing PCD films exploiting a cheap process at a large scale and with performances not far from that of SDDs is for sure an appealing goal, especially because it is generally believed that, at high levels of radiation damage, the PDDs' performances are not expected to be much lower than those of the SDDs [16, 32]. However, this purpose requires specific and dedicated surface science techniques for both fabrication and characterization of samples, since several open points are found, from the complete control of the fabrication process to the possibility of depositing diamond on substrates different from diamond itself. Because of the obvious importance, a dedicated discussion about aspects linked to PCD synthesis will be presented in chapter 2.

1.3.3 "All-carbon" detectors with graphitic contacts

In the design of a solid-state detector, a lot of attention must be paid to electrical contacts fabrication. Indeed, their main goal is the collection of charge carriers created by diamond - radiation interaction, in order to produce a measurable signal bringing information about the incoming radiation. It is then clear why a conductor material is needed, in order to achieve the complete collection of charge carriers. Historically, metal contacts have always been used for electronic applications, mainly based on aluminum, titanium, gold or other conductive materials, and created via processes of metalization or sputtering deposition [33]. However, an interfacial layer to guarantee a good adhesion between diamond and the electrodes is always deposited, that can act as a dead layer and significantly affect the detection performance [34]. For this reason, in the last years, the concept of an "all-carbon based detector" is achieving popularity [35]: diamond, with its already mentioned outstanding properties, would be the active volume of the detector, whereas graphite would be the main material

for electrical contacts. On the basis of this, significant effort has been made to optimize diamond interfacing with conventional electronics [36]. An advantage of graphite contacts over metal electrodes would be the fact that, being graphite the stable form of carbon, graphitic structures can be deposited easily with common deposition processes, or created directly on the diamond sample through various techniques such as ion implantation [37] or laser writing [38]. Particularly, graphite contacts can be of two types. In the first case, they can be created on both the front and the rear surface of diamond, such that a "sandwich" structure is obtained [39]. However, the charge collection efficiency is one of the weak point of PDDs when a standard scheme with sandwiched planar electrodes is used. For this reason, a second kind of graphite electrodes is nowadays widely studied: the so-called "3-D electrodes" [40]. They consist of thin, columnar electrodes written in the diamond bulk by means of laser, and orthogonal to the surface of the detector, whose inter-distance can be about one order of magnitude shorter than the device thickness. In such a configuration, a reduction of the inter-electrodes distance can be achieved, enhancing the charge collection efficiency of the device. However, graphitic structures buried in the diamond bulk show a resistivity even two orders of magnitude higher than the amorphous graphite, and their fabrication can lead to mechanical cracks in the diamond bulk [41].
Concluding, if all-carbon based detectors will be the protagonists for radiation measurements in harsh radiation environments, it is fundamental for some issues to be overcome, from the implementation of PCD deposition processes resulting in high quality material, to the fabrication of perfect ohmic contacts able to efficiently connect diamond to the electronics.

1.4 Diamond detectors in nuclear fusion environment

Nowadays, with the growing interest for novel energy sources able to satisfy the global energy demand with environmental sustainability, fusion energy is becoming a fact. Many laboratories around the world are devoting efforts in making the exploitation of fusion energy a reality, and several promising results have already been obtained. Basing on the idea of extracting energy from the fusion reaction between deuterium and tritium, the two isotopes of hydrogen, the first goal is to make these atoms collide, since the Coulombian repulsive force would tend to distance them. For this reason, a lot of energy must be furnished, and the solution adopted implies to bring the deuterium-tritium fuel mixture to a plasma state at high temperature. Being the plasma composed not only of neutral atoms, but also of charged particles, neutrons and ions, magnetic fields are used to confine the plasma. As can be seen, several kinds of particles and radiation play a crucial role, and a strong and intense radiation field is obtained, whose temperature and composition are directly related to the plasma. Controlling this environment plays a pivotal role, either for plasma diagnostic and safety issue. At this purpose, several detectors have been tested, but with insufficient appealing results. Thanks to their already mentioned properties, diamond detectors are supposed to be the best candidates for this kind of application. SDDs are already employed as common radiation detectors in plasma facilities such as JET [42], and PDDs proved to have good overall performances too [11]. Particularly, diamond detectors proved to be suitable for fast neutron spectroscopy. The fusion reaction between deuterium and tritium $D + T \rightarrow n + \alpha$ creates a population of fast neutrons (i.e. neutrons with energy beyond 0.5 eV [9] and, for this specific case, around 14 MeV) that, being not subjected to the magnetic field confinement, can escape the system. The functioning of diamond detectors for fast neutron spectroscopy is based on the $^{12}C(n,\alpha)^{9}Be$ reaction, whose energy threshold is 6 MeV. Thanks to this nuclear reaction, ionizing particles are created (i.e. α and ^{9}Be), that in turn create electron - hole pairs collected at the electrodes, resulting in a measurable signal event.

However, several issues must be overcome in order to make diamond detector an indisputable technology, especially for fusion applications. Firstly, the performance of the detector must be completely verified: fusion facilities nowadays are still not able to reproduce the real plasma conditions foreseen for future fusion reactors. Additionally, the device fabrication should be cheap and available at a large scale. This means that investigations on the deposition process in order to perfectly control it and obtain a valuable material are still fundamental. Moreover, since SDDs are an expensive technology, a growing interest is put in the realization of PDDs with performances not far from that of the SDDs, but having the material less requirements on its crystalline structure, easier and cheaper synthesis processes can be exploited for their fabrication. Since the macroscopic performance of the material is strongly linked to its microscopic properties, the deposition process must be optimized and controlled.

This will be the main topic of the next chapter, where main issues related to PCD synthesis process will be elucidated.

Chapter 2

Polycrystalline diamond (PCD) films

2.1 Introduction

As shown in the previous chapter, diamond outstanding properties open the possibility of employing this exceptional material in a broad field of applications. However, many issues limit this fact, starting from the cost and scarcity of the material itself. Additionally, diamond is the metastable form of carbon, being kinetically stable but not thermodynamically stable, and a large activation barrier separates this carbon allotrope from the stable one (i.e. the graphite), although their standard enthalpy of formation differs for only 2.9 KJ mol^{-1} [2].

The strong interest in the applications of diamond films has driven for more than 50 years the development of a variety of techniques for diamond films synthesis, either based on physical and chemical processes, aiming at finding the conditions in which diamond is stable upon graphite. The main result came from the exploitation of thermal decomposition of carbon-containing gases under reduced pressure, with chemical vapor deposition (CVD) processes. However, first attempts led to poor results, with simultaneous deposition of diamond and graphite. The breakthrough came in the late 1960s, with the discovery that the presence of atomic hydrogen during the deposition process would lead to preferential etching of graphite, thus preserving the deposited diamond. CVD is nowadays the main process exploited to obtain synthetic diamond, even in its variation where a plasma is used to produce the gas precursors, in the so-called plasma-enhanced CVD (PECVD) technique [43].

Diamond films can be grown on both bulk diamond and non-diamond substrates, and the choice of the substrate itself plays a fundamental role, as will be shown in the following. Briefly, when bulk diamond is used, the resulting film undergoes an homoepitaxial growth and the result is a SCD, since the growing film already finds a proper atomic template and therefore carbon atoms just arrange in the right tetrahedral configuration. When a non-diamond substrate is used, a PCD is grown. As already anticipated in chapter 1, PCD growth is easier and cheaper than single-crystal one: less requirements are found on the deposition procedure (no need of crystalline perfection), and the possibility of growing the PCD film on different substrates permits to expand the range of applications [44]. Additionally, with a properly designed deposition process, PCD features such as quality, microstructure, morphology and level of doping can be tuned.

However, even if the general growth mechanism of diamond is pretty much undisputed, still several contrasting observations are found about what happens in the first stages of growth. For instance, it is widely believed that, without proper substrate pre-treatments furnishing high energy sites acting as nucleation sink, nucleation of diamond on non-diamond substrates would not occur or at least would result in a prolonged, unbearable incubation time. Additionally, different substrates can have diverse interaction properties with carbon, resulting in the formation of a carbon-based interlayer prior to diamond deposition, and there is no general common observation about the nature of this interlayer. A deep understanding of issues related to the growth of PCD on different substrates is therefore desirable, since it is by controlling the deposition process in all its aspects that diamond films with tailored properties can be grown [3]. For reaching this goal, a complete and adequate diamond film characterization is fundamental too, and several characterization techniques can be employed, as will be shown later in this chapter.

In light of these observations, the PCD synthesis is the main topic of this chapter. In section 2.2 the two steps towards PCD synthesis are presented, i.e. nucleation and growth. In section 2.3 the main process parameters influencing diamond synthesis with CVD techniques are elucidated. After this, in section 2.4, main CVD and PECVD diamond synthesis techniques are introduced, with a dedicated section about the direct-current micro-plasma (DC-μP) device as a powerful PECVD technique for diamond studies. To conclude, in section 2.6 diamond characterization is discussed.

2.2 Two steps towards PCD synthesis: nucleation and growth

Polycrystalline diamond synthesis on non-diamond substrates can be sketched in two steps: nucleation and growth. CVD and PECVD are the most used processes, as already shown in section 2.1, in which the activation of specific gaseous species makes the growth possible thanks to the formation of radicals acting as diamond precursors [3]. How the activation is achieved makes the difference: a hot filament is used in the standard CVD, with precursors remaining in the gas phase, whereas a plasma generating system such as microwave or electric discharge is used for PECVD. However, the growth mechanism is the same, and here in after all considerations about diamond growth mechanism will be valid for CVD and PECVD as well.

The diamond deposition goes on in a gas environment that is carbon under-saturated with respect to diamond: this is the main feature, resulting in an apparent violation of the chemical thermodynamic principles [45]. Of course, no actual violation occurs, as will be shown in the following. Once the gas chemical dissociation is done, chemical species containing carbon precursors can diffuse in the substrate and react with it. At this point, the first step of diamond synthesis can take place, i.e. the nucleation. This is the critical step, occurring only on non-diamond substrates, where an atomic template such that of diamond is not present. A controlled nucleation is fundamental since it can influence the adhesion, structure, grain size, roughness and orientation of the diamond film [46]. Moreover, having diamond a high surface energy with respect to other materials ($\approx$ 6 J cm^{-2} [47]), conditions for nucleation on non-diamond substrates are anything but trivial. For this reason, an initial period of incubation before diamond nucleation sets on can be prohibitively long. Carbon atoms from the gas phase start impinging the substrate, diffuse and saturate it. Then, by finding high energy sites acting as preferential nucleation sink, diamond can nucleate. After conditions for diamond to nucleate are reached, the first diamond grains are formed, and the second step, i.e. the growth, can start. It is at this point that hydrogen plays the major role. As already introduced, diamond growth is an apparently paradox form a thermodynamic point of view. However, if diamond growth is thought as a chemical process resembling polycondensation rather than a normal crystal growth, a solution to the thermodynamic paradox is given [48]. Polycondensation consists in the growth of macromolecules of polycyclic saturated hydrocarbons generally called polymantanes. Some examples are adamantane ($C_{10}H_{16}$), diamantane ($C_{14}H_{20}$), triamantane ($C_{18}H_{24}$) etc. This concept is not unreasonable: polymantanes macromolecules are indeed identical to diamond single-crystal in structure except for the fact that, on the surface, they have H-terminated bonds. That being said, the CVD growth process can be summarized in the following three cycling reactions:

1. chemisorption of carbon in the gas phase C(g) on the surface of an H-terminated diamond seed crystal $H(C_{dia})$ (polymanatanes macromolecules seeds), resulting in the formation of unsaturated (i.e. containing only sp^2 bonds) clusters $C_2H_2(2C_{dia})$:

$$2H(C_{dia}) + 2C(g) \Leftrightarrow C_2H_2(2C_{dia}) \tag{2.1}$$

2. hydrogenation of the unsaturated clusters, i.e. conversion of the unsaturated clusters $C_2H_2(2C_{dia})$ into saturated ones $C_2H_4(2C_{dia})$ (i.e. containing sp^3 bonds) thanks to the impact of the atomic hydrogen H(g):

$$C_2H_2(2C_{dia}) + 2H(g) \Leftrightarrow C_2H_4(2C_{dia}) \tag{2.2}$$

3. coalescence of saturated clusters into a new layer of sp^3 carbon with diamond structure (C_{dia}), with simultaneous recreation of the hydrogen-terminated surface:

$$C_2H_4(2C_{dia}) \Leftrightarrow 2C_{dia} + 2H(C_{dia}) + H_2(g) \tag{2.3}$$

   where H_2(g) represents gaseous molecular hydrogen.

The overall reaction obtained by combining these three steps is:

$$C(g) + H(g) \Leftrightarrow C_{dia} + 0.5H_2(g) \tag{2.4}$$

that is of course not complete but useful for calculation, since it contains quantities with very well defined and easily available thermodynamics properties.

As previously mentioned, in this growth process the hydrogen makes the difference. Therefore it is worth spending some words on the role of H(g). Looking at reaction (2.2) it is clear that, for being shifted to the right, the concentration of atomic hydrogen in the gas phase reaching the growth surface should be several orders of magnitude higher than the concentration of atomic hydrogen in the gas phase that would be at equilibrium at the substrate temperature. Additionally, only unsaturated clusters chemically bonded to the growth surface are converted into saturated clusters that subsequently coalesce and finally form a new diamond layer; other unsaturated clusters and sp^2 carbon structures, e.g. graphite, which can form on the growth surface but are not chemically bonded to it, are not converted into diamond but are etched from the surface by free hydrogen atoms. If the deposition rate is faster than the etching rate, the remaining portion of sp^2 structures is incorporated into the diamond film as a second phase. For all these reasons, H(g) is called *super-equilibrium atomic hydrogen*, and its task is dual: firstly, it etches away preferentially sp^2 with respect to sp^3 carbon, subsequently it goes through the so-called process of hydrogen abstraction

$$H(C_{dia}) + H(g) \longrightarrow C_{dia} + H(g) \tag{2.5}$$

that is fundamental for stabilizing the sp^3 network [49].

Once a network of sp^3 carbon is formed, PCD grains can grow in dimension and coalesce, and a columnar growth starts. The final features such as morphology and structure are strongly dependent on many process parameters such as temperature, pressure, gas composition, precursors etc. Particularly, depending on the structure, PCD can be classified as in the following [50]: microcrystalline (MCD, grains dimension from one to hundreds of μm), nanocrystalline (NCD, grain size normally less than 100 nm) and ultra-nanocrystalline (UNCD, grain dimension around 3 - 5 nm). Again, NCD can be either flat or ballas-like, depending on the specific morphology. All these kinds of PCD share one peculiarity, that is the presence of grain boundaries, considered as defects where carbon with sp^2 sites can be found. The cristallinity degree of diamond strongly influences its features, determining the field of use.

2.3 Process parameters influencing PCD synthesis with chemical vapor deposition (CVD) techniques

Of course, many parameters can influence the PCD synthesis with CVD techniques, determining the overall quality, morphology and structure of the resulting film [50]. In this section, a focus on main parameters common to all CVD techniques is given. Particularly, pressure, temperature and gas composition are discussed, and a special attention to the substrate and the substrate pre-treatment is paid too.

2.3.1 Temperature, pressure and gas composition

The substrate temperature. The temperature is the first parameter introduced. Historically, diamond was grown under sever conditions of both pressure and temperature, following observations about how diamond is formed deep underground. However, the development of vacuum technology together with the possibility of synthesizing diamond in less extreme conditions allowed to reduce the temperature of the deposition process. In the nucleation step, fixing all the other deposition parameters, an increase in the substrate temperature leads to an increase in the nucleation density: that is because the surface diffusion length of the species changes, together with the adsorption state, from a physical to a chemical adsorption [51]. In the growth step, an increase in the substrate temperature is responsible for an increase in the deposition rate, and a different morphology is achieved (and thus a different cristallinity degree): well-faceted diamond microcrystals for higher temperature, and ballas-like nanocrystalline morphology for lower deposition temperature. Particularly, the change in the deposition rate is justified by the fact that the growth rate follows an Arrhenius behavior:

$$G = A\, e^{\frac{-E}{RT}}$$

where A, E, R and T are respectively the pre-exponential factor, the activation energy for growth, the universal gas constant and the absolute temperature.

The pressure. During the nucleation step, the pressure dependence of the nucleation density is a result of the competition between two factors: at higher pressure there is a higher formation of energy sites but, at the same time, increasing in atomic H etching (that, in turn, limits the nucleation rate). Regarding the growth step, high pressure normally increases the growth rate, because of the presence of more radicals near the substrate surface.

The gas composition. Gas composition is another fundamental parameter for diamond growth. As already stated, gas mixture must be composed by a carbon precursor (e.g. methane, acetylene, etc) and hydrogen. Increasing the relative amount of carbon precursor in the gas would mean enhancing radicals concentration such as CH_3 and C_2H_2, resulting in a higher nucleation density. At the same time, relative quantities of sp^3 and sp^2 incorporated in the diamond film depend upon the carbon / hydrogen concentration in the gas mixture. Also, additives as N_2 and O_2 can be used to control the morphology of the grown diamond. For instance, the presence of N_2 proved to have beneficial effect in the synthesis of NCD, whereas a certain amount of O_2 (even as CO_2) permits to achieve low temperature deposition. Finally, when halogenated compounds are present in the gas, the growth rate can increase to the detriment of the phase purity of diamond film: this is supposed to depend on the lack of etching of graphitic phase by halogens such as chlorine and fluorine.

2.3.2 Substrate material and pre-treatment

The substrate material. The substrate material is one of the key points for a successful growth of diamond films. Some criteria must be satisfied for a substrate to be an eligible candidate for diamond growth. Firstly, the substrate must have a melting point, at the process pressure, higher than the temperature required for diamond growth. Additionally, the substrate should have a thermal expansion coefficient comparable with that of diamond, to avoid significant compressive stresses in the diamond film once the substrate is cooled. Finally, material should be in some way able to chemically interact with carbon, to guarantee adhesion. On the basis of this, substrate materials suitable for diamond growth can be organized into three main families, depending on carbon/surface interactions, namely: materials having a little or no solubility or reaction with C (e.g. copper, silver and gold), materials showing a mutual solubility or weak reaction with C (e.g. platinum, palladium, nickel and iron) and materials with strong carbide formation tendency (e.g. titanium, molybdenum, tungsten, silicon and so on). Additionally, it is widely believed that nucleation of diamond on non-diamond substrates usually occurs via an intermediate carbon-based layer [52]. This layer may be the result of the interaction with the substrate during the deposition process, or an intentional controlled deposition before diamond synthesis (i.e. a pre-treatment of the substrate surface, see below). To date, diamond films have been grown on carbide layer [53–55], graphite [56–60], diamond-like amorphous carbon and carbon oil [61–65]. However, even if the theory of diamond growth mechanism is generally well agreed [66–68] there are still several contrasting observations on what happens during the nucleation and the early stages of growth. Moreover, evidence of diamond nucleation either in the gas / plasma phase or directly on the substrate has been recently reported [69, 70]. As already shown, the overall properties of the grown films are strongly dependent upon the dynamics of the first stages of growth, and it is essential a complete understanding of the interfacial mechanism between the diamond film and the substrate.

The substrate pre-treatment. As previously mentioned, the nucleation on non-diamond materials is a crucial step towards the deposition of diamond. The period needed for diamond grains to nucleate can result in prohibitively long incubation time, and a successful and uniform coverage of the substrate surface with a diamond film is not even guaranteed. For this reason, several surface pre-treatment methods have been tested and refined. The general idea starts from the consideration that one of the main difficulties towards diamond nucleation relies on its high surface energy. Therefore, the main goal of substrate pre-treatments is furnishing to carbon atoms impinging the surface several "nucleation sinks" acting as high energy sites, e.g. carbon-rich particles, defects such as scratches, grain boundaries, edges and so on. It is commonly believed that, without substrate pre-treatment, slow, irregular or even no nucleation would occur [71–74].

One of the most exploited and simple methods of surface nucleation enhancement is the mechanical scratching of the substrate [75]. In this way, defects are created on the substrate surface and a certain number of surface bonds are broken, resulting in dangling bonds at sharp edges. Abrasives used for scratching include diamond itself, silicides, nitrides and carbides [76]. Nucleation density is influenced by abrasive particle size and number of defects created. Also, seeding the substrate with diamond or carbon-based compounds can help achieving a higher nucleation density [77]. The residual seeds are sinks for nucleation. Several seeding procedures are used, such as dipping, spraying, ultrasonic bath and electrophoretic seeding. However, both scratching and seeding can cause surface contamination and damage, and for this reason they are not the preferential methods when an extremely smooth and clean surface is required. Biasing the substrate is another used mechanism for substrate

pre-treatment. In this case, the net effects are the suppression and removal of the surface oxides and overcome of the energy barrier by activating efficiently the substrate surface. Both positive and negative biasing are demonstrated to help achieving a higher nucleation density, and a particularly effective way is the so-called bias-enhanced nucleation (BEN), where an *in-situ* surface bombardment under an applied negative bias is performed on a conductive substrate [78, 79]. Also surface covering was found to be effective for surface nucleation enhancement [62, 64, 80]. Briefly, the substrate surface is covered by thin films of carbon-based compounds or materials able to undergo strong bonds with carbon: this interlayer can have different thickness and besides providing high-energy sites for nucleation, it can easily promote carbon saturation of the substrate surface. Both biasing and coating of the substrate are effective way to enhance diamond nucleation without affecting the substrate with damages. Finally, ion implantation is another example of substrate pre-treatment [81]. By implanting ions of the same chemical specie of the substrate, surface structure is changed with the formation of high-energy sites, and no chemical contamination is promoted.
Of course, all these methods can significantly influence the morphology and structure of the diamond films, and thus it is essential to tune the pre-treatment features in detail depending on the application in mind for the diamond film.

2.4 Overview of main CVD techniques for PCD deposition

As already explained in section 2.2, for a successful deposition with a CVD process, the first essential step is the activation of the gas. Depending on the activation method, three main families can be identified: thermal CVD, combustion flame-assisted CVD and plasma-ehnanced CVD (PECVD), where the plasma generating system can be microwave, direct-current (DC) or radiofrequency (RF). Basing on this classification, the main deposition methods for PCD synthesis are described below.

Hot-filament CVD. A schematic diagram of hot-filament CVD (HFCVD) deposition technique is depicted in fig. 2.1, inset a). This is the earliest method used to grow diamond [82], and belongs to the first family. In this method, diamond is deposited on a substrate from a gas mixture of methane and hydrogen undergoing thermal dissociation due to the presence of a high-temperature filament (usually tungsten or tantalum) placed near the substrate. The filament working temperature can reach 2200 °C, and the main role of the filament relies in the dissociation of molecular hydrogen into atomic hydrogen. However, it was found that during deposition the metal filament reacts with methane, undergoing

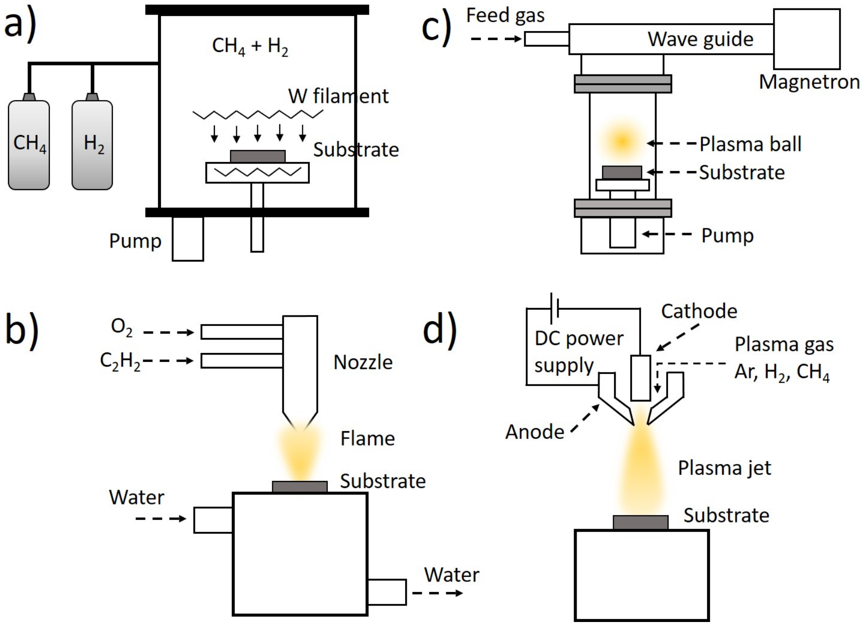

Figure 2.1: *Schematic sketch of the deposition techniques mainly used for synthetic diamond production: a) hot-filament CVD, b) combustion flame-assisted CVD, c) microwave and RF plasma CVD and d) DC plasma-assisted CVD.*

carburization. Besides changing the filament resistivity making it brittle (reduction of lifetime), this leads to a significant loss of precursors resulting in a certain incubation period before nucleation. Additionally, the upper limit of the filament temperature sets a boundary in the amount of hydrogen production. For this reason, low growth rates are achieved. However, being simple and cost effective, HFCVD is widely used for diamond production.

Combustion flame-assisted CVD. This is an atmospheric pressure working method (see inset b) of fig. 2.1) [83]. The activation of gas is achieved through combustion flames from an oxygen-acetylene brazing torch. The ratio of acetylene to oxygen ($C_2H_2/0_2$), which is very critical for the formation of the oxy-acetylene flame and for the diamond deposition, is usually close to unity. Diamond crystals form where the tip of the bright interior part of the flame is in contact with the substrate, in a temperature range around 800 - 1500 °C. Among the advantages there are for sure the simplicity and cost effectiveness of this device, due to the lack of power supply system and vacuum equipment, the high growth rate and the possibility of covering large areas. However, it is quite difficult to control the deposition, and this implies the formation of inhomogeneous diamond films, both in morphology and microstructure.

Microwave and RF plasma CVD. Microwave and RF plasma CVD (MWCVD and RFCVD respectively) were the first techniques used in which the activation of gas was made with an electrical discharge [84]. Both are plasma-assisted methods (PECVD) belonging to the third family, where the excitation frequency is 2.45 GHz for the microwave plasma and 13.56 MHz for the RF plasma. A schematic of this deposition method is represented in the inset c) of fig 2.1. Despite the expensive equipment required for these deposition techniques, the growth rate significantly increases with respect to the HFCVD. Moreover, the possibility of tuning MW power allows to finely control the deposition. All these features make these deposition techniques the most used and preferred.

DC plasma-assisted CVD. With the expression "plasma-jet", a high-pressure plasma discharge is intended in which the convection plays a significant role in transport processes (see inset d) of fig. 2.1) [85, 86]. Electrical energy is converted into kinetic and thermal energy of a flowing gas mixture through an electric arc discharge. Common methane - hydrogen mixtures are used, in a range of temperature for the plasma around 1000 - 1500 K. Since the electric discharge is sustained between a concentric cathode rode and a surrounding cylindrical anode, a nearly fully ionized plasma is achieved, and thus extremely high growth rates can be obtained.

In the family of the plasma-assisted CVD, the micro-hollow discharge is attracting great attention lately. Thanks to the simplicity, cost effectiveness, high growth rate and versatility with respect to plasma generating system, gas precursors and substrate material, this technique has found lots of applications not just in the nanomaterial fabrication, but also in many micrometric processes where a precise and controlled method is required, such as direct patterning of electronic materials, nanoparticles synthesis and excimer emission [87–89]. Also, its application to diamond deposition has been successfully proved.

2.5 PCD produced with direct-current microplasma (DC-μP) technique

As anticipated in the previous section, microplasma devices are attracting great attention lately, especially for precision applications where an accurate and strictly controlled process is required. A number of geometric configurations such as cylindrical cavities, micro-tubes and microslots have been experimentally investigated by many research groups

[90].

Most of the existing plasma technology for nanomaterial synthesis normally operates at low pressure, which means expensive vacuum equipment and limited investigation range for process parameters. Additionally, the spatial scale of the reaction volume involved in these reactors is always large, leading to difficulties in controlling temperature uniformity and concentration and residence time distribution environment for particle nucleation and growth [88]. In the micro-hollow cathode discharge configuration, a stable, non-equilibrium plasma in a small volume and either at low and high pressure can be produced; because of the high density of active species, increased surface-to-volume ratio and intense radiation produced, the exploitation of this device for nanomaterials synthesis is earning much popularity. Due to the sub-millimeter dimension of the discharge (hollow-cathode around 200 μm), a diagnostic of either the discharge process and the characteristics is extremely difficult and challenging, but by modeling and simulation many detailed characteristics have already been extrapolated [91, 92].

The preferred configuration for materials deposition is the flow geometry, where species produced near the hollow-cathode (that is also the tube for gas inlet) are transported to the substrate, placed in front of the cathode on a substrate holder, acting also as the anode (parallel electrodes geometry). A direct-current source is used to obtain the plasma, which means that in this configuration only conductive substrates can be used. In this geometry, the breakdown of the gas is achieved by applying a direct-current electric field between the eletrodes. Then, electrons in the gas feel the acceleration and start oscillating and ionizing the gas through collisions. Once the breakdown of the gas is achieved, a glow discharge is obtained whit a typical current-voltage (I-V) characteristic, and the gas becomes conductive. Paschen law describes the voltage V$_b$ at which breakdown occurs:

$$V_b = \frac{Bpd}{\ln Apd - \ln\left[\ln 1 + \frac{1}{\gamma}\right]} \tag{2.6}$$

where A and B are gas parameters, d is the electrodes distance, p the chamber pressure and γ the Townsend secondary electron emission coefficient for the cathode. As can be seen from eq. 2.6, the breakdown voltage depends particularly on the "pd" product, and plots of the V$_b$ values versus "pd" are known as Paschen curves. Example of Paschen curves for different gases and a given cathode material are reported in fig. 2.2.

At this point, a range of values for the "pd" product can be identified, in which the so-called hollow-cathode effect is sustained, that is at the basis of the DC-μP functioning for diamond deposition [93, 94]. Several mechanisms have been suggested to explain the hollow-cathode effect, e.g. photon induced secondary emissions, electron pendular motion, ionization in the cathode fall region and enhanced ion collection, and they all

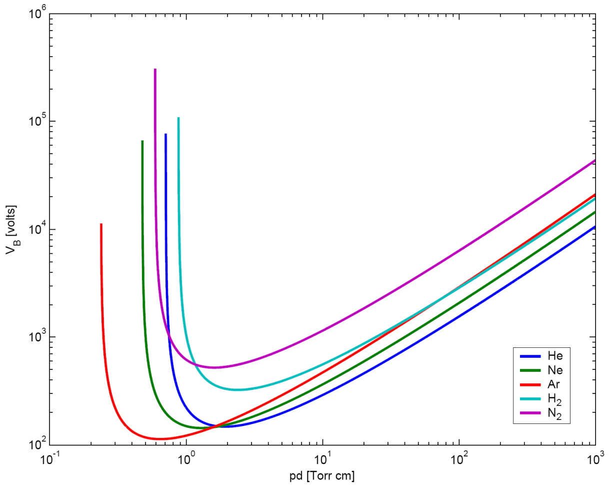

Figure 2.2: *Paschen curves for different gases representing the breakdown voltage as a function of the "pd" product between the pressure p and the elctrode distance d.*

contribute to the hollow-cathode effect, with the predominance of one of them depending on the cathode dimension and discharge conditions [95]. However, it is generally accepted that the pendular motion of high energy electrons and the efficient collection of ions are key elements. Values permitted for the "pd" product in order to achieve the hollow-cathode effect lie in the range 1 - 5 Torr cm. In this interval of values, two pressure ranges can be defined, and at a given pressure range there is a predominant mechanism sustaining the hollow-cathode effect. At lower pressure (i.e. around 1 Torr cm), the plasma column formed starts acting as a virtual anode, causing a modification of the electric field distribution in the hollow, i.e. from the initially axial electric field to a radial one. At this point, electrons are accelerated radially towards the axis and for a pressure p such that the mean free path for ionization is on the order of the hole radius, the electrons gain enough energy to oscillate through the plasma. For this reason they are called *pendulum electrons*. Their oscillation is such that a drastic increase in the ionization events is produced. In this way, a high-density plasma is achieved (electron density around 10^{16} cm^{-3}), with high-energy electrons (energy $>$ 10 eV), and the hollow-cathode effect is achieved. At higher pressure, the cathode fall region in which electrons are accelerated is higher than the actual cathode dimension, and the *pendulum effect* is inhibited by collisions; however, positive ions created behave the same as electrons, being accelerated and involved in collisions themselves, that are responsible for further ionizations. When the ions strike the cathode, electrons are liberated from the metal surface (secondary electron emission). In such a way, even at higher pressure an entire avalanche of electrons is formed, sustaining the hollow-cathode effect.

Thanks to the versatility that this device shows regarding the possibility of working even at higher pressure with respect to conventional deposition methods, a cost effectiveness in vacuum equipment is obtained, together with the possibility of exploiting wider range of process parameters. Additionally, this system provides few heating power at the substrate, and thus no cooling system is required as for the case of many PECVD set-up, and this further simplifies the deposition apparatus.

2.5.1 Use of DC-μP for diamond and other carbon allotropes deposition

Besides the many possible applications, the DC-μP has already proved to be particularly efficient ad versatile for the deposition of diamond and other forms of carbon.

The first demonstration was made by Sankaran et al. [96], where a film of microcrystalline diamond continuous over a 500 μm diameter area was deposited. The substrate used was untreated Mo, with the common CH_4/H_2 gas mixture with abundance of hydrogen, and 2 - 4 hours of growth time were set. Temperature was set at 800 °C and pressure at 200 Torr, with a micro-hollow diameter around 178 μm. The purity of the film was found to increase with decreasing methane percentage in the gas mixture. However, the versatility of this device relies not just in the possibility of finely tuning different process parameters (such as pressure, temperature, substrate material, gas composition, plasma generating system), but also in the possibility of producing different carbon allotropes by properly varying the substrate temperature keeping fixed all the other parameters [97]. In this way, diamond films with different grain size, carbon nanotubes, graphite, few-layer graphene and amorphous carbon are successfully deposited. As a guide, a non-equilibrium non-dissipative thermodynamic model acting as a predictive model for process parameters have been extrapolated from PECVD deposition and proved to be suitable also for diamond deposition with DC-μP.

2.5.2 Thermodynamic model for diamond growth applied to DC-μP system

Diamond growth mechanism with CVD and PECVD has already been reported in section 2.2. Briefly, it is described by three cyclically recurring reactions, that can be summarized as follow: i) formation of unsaturated carbon-hydrogen clusters on the surface of a diamond seed, ii) hydrogenation of such clusters and conversion into saturated ones and iii) coalescence of saturated clusters into a layer with diamond structure. As mentioned above, the main role is played by the atomic hydrogen, found at

the energy and concentration expected when in thermal equilibrium with the other gas species. The gas temperature is around 2000 - 4000 °C and the substrate surface around 500 - 1200 °C. Independently from the activation source used for creating monoatomic hydrogen and radicals (hot filament, microwave, etc.), the concentration of monoatomic hydrogen (in equilibrium with respect to te source, being produced there) increases by a factor of 10^4 from 1000 to 2000 °C, and it is said to be super-saturated and in super-equilibrium with respect to the surface temperature.
Generally speaking, a deposition process can proceed only under out-of-equilibrium conditions, either kinetics and thermodynamics, and consists of a non-dissipative process. For this reason, to study the thermodynamic equilibrium and, in this specific case, find conditions for diamond to be stably grown, the minimization of entropy production can be applied that, when dealing with non-equilibrium non-dissipative processes, corresponds to the Gibbs free energy minimization principle [98, 99]. Additionally, for the case of CVD diamond, the following assumptions are taken:

- an adequate concentration of super-equilibrium atomic hydrogen H^* present at the gas-solid interface;
- activation temperature T_{act} of this super-equilibrium hydrogen (i.e. the monoatomic hydrogen temperature when hydrogen is produced by the hot filament or by the plasma) the same of the plasma phase;
- surface carbon interacting with hydrogen called C^*(gra) (i.e. "activated graphite").

Thus, the reactions 2.2 and 2.3 can be rewritten as follow:

$$C_{gra} \Leftrightarrow C_{dia},\ \Delta G_1 > 0,\ T = T_s,\ p \leq 10^5 Pa \tag{2.7}$$

$$2H^* \Leftrightarrow H_2,\ \Delta G_2 \ll 0,\ T_s \ll T_{act},\ p \leq 10^5 Pa \tag{2.8}$$

where C_{gra} is the surface carbon in sp^2 state, T_s the substrate temperature, G_i the Gibbs free energy and p the total pressure. These two equations can be coupled by a coupling parameter χ:

$$C_{gra} + \chi H^* \Leftrightarrow \frac{\chi}{2} H_2 + C_{dia},\ \Delta G_3 = \Delta G_1 + \chi \Delta G_2,\ T = T_s,\ p \leq 10^5 Pa \tag{2.9}$$

When χ is such that $\Delta G_3 < 0$, the diamond formation is favored upon graphite deposition. For the sake of simplicity, the last equation can be rewritten as:

$$C^*(gra) \Leftrightarrow C_{dia},\ T_{act} \gg T_s,\ p \leq 10^5 Pa,\ \Delta G_{T,p} \leq 0, \Delta S > 0 \tag{2.10}$$

where $C^*(gra) = C(gra) + \chi(H^* + \frac{1}{2} H_2)$ is named as "activated graphite", with a contribution in Gibbs free energy higher than the original graphite

in these conditions. The difference in Gibbs free energy is furnished by the super-equilibrium atomic hydrogen when forming equilibrium molecular hydrogen.
If represented in this way, the power of this process relies in the use of substances with properties all available in literature, and thus it becomes suitable for a thermodynamic analysis. If applied to the DC-μP, the three step model proposed allows to separately minimize diamond and graphite contributions, and simply superimpose the diagrams to obtain a global graph reporting conditions for a stable deposition of diamond. Additionally, thermodynamic properties of activated graphite are influenced by the pressure p, the substrate temperature T_s, the activation temperature T_{act}, the carbon concentration in the gas x(C) and the coupling parameter χ, and all these parameters with except of χ can be controlled during the CVD deposition process. Choosing $\chi = 0.28$ as a value for the coupling parameter (as suggested in literature), phase relations between gas, diamond, activated graphite and regular graphite can be easily represented by classical phase diagrams [97], and stable conditions for diamond growth can be identified, see fig. 2.3. In this graph,

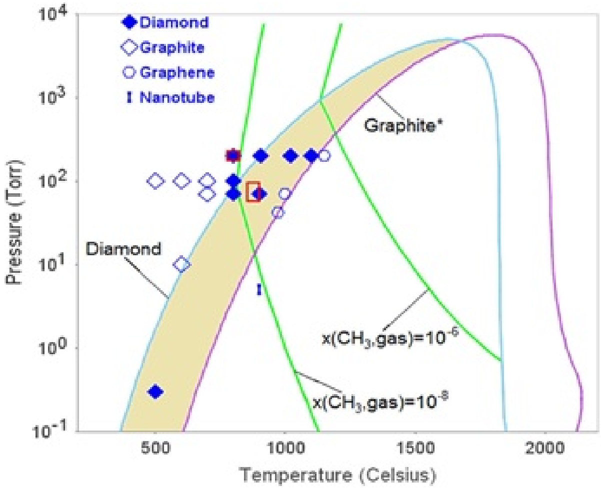

Figure 2.3: *Pressure - temperature C - H phase diagram calculated for a* H_2/CH_4 *flux ratio of* $5 \cdot 10^{-3}$*, with* $T_{act} = 2400$ *K and* $\chi = 0.28$*. Conditions favorable for diamond growth correspond to the shaded area. The blue symbols represent previous experimental data obtained from the DC-*μ*P method described in this work. The red squares represent experimental data obtained from [96, 100, 101], that confirm the model.*

conditions favorable for diamond growth are represented for a substrate temperature range admissible for most of metals. The bell-shaped curves are boundary for stability regions of solid compounds (both diamond and graphite*) with respect to the gas phase: particularly, diamond is stable in solid form under the light-blue bell-shaped curve, and graphite* is stable as solid phase under the pink curve. Outside these regions, they are stable in gas phase. This permits to identify a region (the shaded one) in which diamond is stable in a solid form, whereas graphite is stable in the gaseous phase. Blue symbols represent data from [97] whereas red symbols represent experimental data from [96, 100, 101], that confirm the model. Additionally, green curves define the area where the mole fraction of the CH_3 species in the gas is in the range 10^{-6} - 10^{-8}, a favorable condition to enhance diamond deposition kinetics [102].

2.6 Diamond characterization

Once grown, several characterization techniques can be used, to evaluate diamond features. Both morphological and structural information can be acquired, and an extensive and complete characterization is essential to classify diamond with regards to crystalline quality, grain size, type of chemical bonding, structural disorder and so on. This is the topic of this section, where the main characterization techniques employed for diamond will be presented.

2.6.1 Morphological characterization

The morphological characterization is essential in order to get a visible evidence of the morphology and surface roughness of diamond. Several characterization techniques can be used, depending on the degree of details required.

Scanning electron microscopy. Scanning electron microscopy (SEM) is among the most used characterization techniques for diamond, as for every kind of material. It is based on the interaction between electrons from a primary beam focused on a fine probe and moved on the sample as a scanning tool, and atoms of the sample surface. The result of the interaction is a bundle of *secondary electrons* (SE) acquired by a specific detector and converted into an electric signal. In this way it is possible to reconstruct a black and white picture of the sample surface. Also *back-scattered electrons* (BSE) can be used, and X-rays emitted by the sample. Information about the morphology can be deduced, the thickness of the film when measurements are made in cross-section and, if accompanied by an electron-dispersive X-ray spectroscopy (EDXS) tool (acquiring the X-rays from the sample), also qualitative informations about elemental composition and impurities can be obtained. BSE are produced by elastic scattering events between primary electrons and atomic nuclei. Being back-scattering cross-section proportional to Z^2, the higher the

specimen atomic number is, the more BSE are produced. SE are the result of inelastic collision between primary electrons and electrons of sample atoms. Indeed, if the energy is sufficient, SE can be kicked-out. For being revealed by the detector, they need to have an energy higher than the material work function; for this reason, usually only SE generated in the first nm of the material can be detected. After inelastic scattering, atoms are in an excited state. Relaxation happens by emitting X-rays or Auger electrons. EDXS uses these emissions to identify elements present in the probed region.
With a resolution of about tens of nanometer, it represents a powerful surface characterization techniques. Since it is user friendly, with immediate impact and non-destructive, it finds large use for materials characterization and it is also extensively exploited for diamond [79, 103–108].

Transmission electron microscopy. Another widely used morphological characterization technique is the transmission electron microscopy (TEM). During a TEM measurement, electrons from the primary bundle pass through the sample and hit a fluorescent screen behind the measured sample. The result is the projection of an image of the section of the measured sample. With respect to SEM, the investigated surface area is relatively small (thickness between 50 and 500 nm), but the resolution is far better, nearly atomic when an high-resolution TEM is used. TEM finds wide exploitation for the investigation of interfaces between different materials, since it permits to acquire information about atoms and subsequently understand interfaces bonds, and it is thus the preferred characterization technique for fine nucleation studies. However, this characterization technique is quite demanding with respect to sample preparation and results interpretation, and thus not so common as SEM [53, 61, 109, 110].

2.6.2 Characterization of the crystalline structure

Structural characterization in diamond is essential, especially for a polycrystalline structure. As already mentioned, a PCD is a material containing not just sp^3 crystalline phase (i.e. diamond) but also sp^2 phase located at the bulk and grain boundaries in the form of graphite, amorphous and disordered carbon. For this reason it is evident that, for such a complicated system as a PCD is, a detailed characterization about structure and hybridization of carbon atoms is even more useful than a morphological one.

X-ray diffraction. One of the most used structural characterization techniques is for sure X-ray diffraction (XRD). It is a non-destructive characterization technique based on the interaction between X-rays from a primary bundle that, because of the interaction with crystalline planes of the sample lattice, are diffracted. The diffraction angle is linked, through the Bragg's formula, to the distance between crystalline planes:

$$n\lambda = 2d_{hkl}\sin(\Theta_{hkl})$$

where λ is the incident radiation wavelength, d_{hkl} is the distance between crystals planes with Miller indexed (hkl) and Θ_{hkl} is the angle between planes and incident X-rays beam. The information obtained refers to the degree of cristallinity and stress state of the sample (i.e. inter-atomic distance), and thanks to a dedicated database also specific crystalline chemical compounds can be revealed [106, 111–114].

X-ray photoelectron spectroscopy. For analyzing diamond - substrate interface, X-ray photoelectron spectroscopy (XPS) is another powerful characterization technique. In a typical XPS measurement, the sample is irradiated with a monochromatic X-rays source. Photons in the material undergo several reactions i.e. photoelectric effect and Auger emission. As a result, an electron is ejected from the sample, with a kinetic energy linked to its binding energy. In this way it is possible to identify chemical elements in the material and hybridization status of atoms [61, 115–118].

Low-energy electron diffraction. Low-energy electron diffraction (LEED) is a characterization technique in which the surface structure of a material is irradiated with a collimated beam of low-energy electrons (usually electron energy lies in the range 20 - 200 eV). As a result of the interaction, electrons diffracted are observed as spots on a fluorescent screen. Once the diffraction pattern is recorded, the analysis of the spots position gives information about the symmetry of the investigated surface. Such kind of structural characterization technique presents a limitation: the sample must be a single-crystal with a well-ordered surface structure, otherwise a back-scattered electron diffraction pattern can not be generated. For this reason, it is widely used for the investigation of homoepitaxial growth of diamond on appropriate substrates (e.g. iridium) [119–121].

Electron energy loss spectroscopy. In a typical electron energy loss spectroscopy (EELS) measurement, the analyzed material is exposed to an electron beam with a narrow range of kinetic energy: as a result of the interaction, a certain fraction of electrons undergoes inelastic scattering and loses partially energy being simultaneously deflected in the trajectory. The energy loss is recorded through a spectrometer. With this technique it is possible to determine the types of atoms, and the number of atoms of each type, being struck by the beam. The scattering angle (i.e. how much the electron path is deflected) can be measured too, giving information about the dispersion relation of the sample [122–124].

Raman spectroscopy. Among the possible spectroscopic techniques used for structural characterization, Raman spectroscopy worths a special mention. Indeed, nowadays it represents the most used non-destructive characterization technique for carbon-based system [125–129], even for the specific case of diamond [54, 80, 97, 103, 105, 110, 111, 130–132]. Since it finds large use in this work, a special attention is paid, with a detailed description.

Generally speaking, several and complex effects can be observed when light interacts with matter. When using a conventional Raman spectrometer (equipped with visible or UV excitations), given a monochromatic light with frequency ν_0 and wavelength λ_0 incident on a material, three situations can be described, see fig. 2.4, that can all be measured with the same instrument and in the same measurement. The light can i) be elastically scattered, ii) be inelastically scattered with frequency higher or lower than the incoming one or iii) interact with the electronic bands of the solid being thus absorbed and giving rise to photoluminescence (PL) transitions.

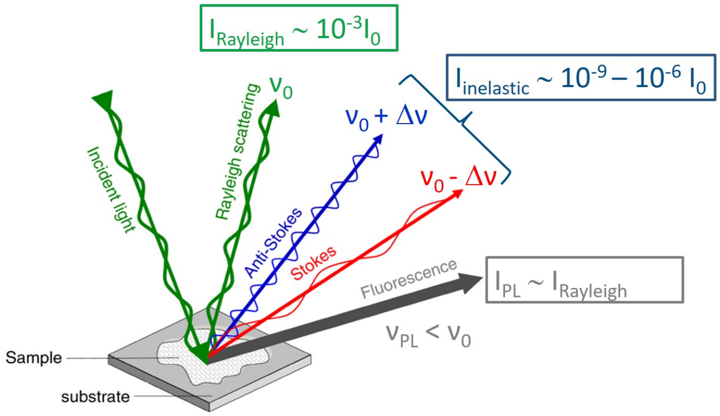

Figure 2.4: *A schematic sketch of the possible effects of the interaction between the light and a material, detectable with a Raman spectrometer.*

Particularly, when referring to light scattering, the various effects happening are the result of the interaction between a monochromatic incident light and the vibrational modes (phonons) of the material. To be thorough, either acoustic and optical phonons can be investigated: the first one with Brillouin spectroscopy, whereas the optical are the one involved in Raman scattering. For this reason, hereafter only interaction of light with optical modes will be described. After the interaction, in the resulting spectrum the intensity of the diffused light is distributed over a certain range of frequency centered on ν_0, see fig. 2.5.

The most intense contribution comes from the Rayleigh scattering, with

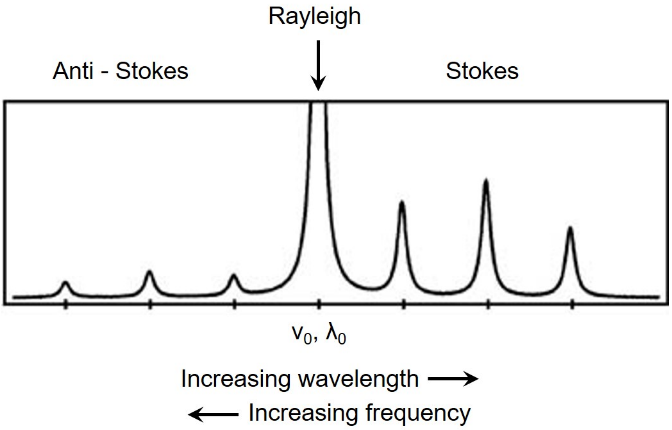

Figure 2.5: *Intensity of the diffused light after the scattering interaction with a material, as a function of both wavelength and frequency: the Rayleigh peak represents the most intense component, and Stokes and anti-Stokes contributions are disposed symmetrically with respect to the central Rayleight peak.*

photons elastically diffused: however, Raman spectrometer is equipped with a cut-edge filter excluding this component. Peaks with lower intensity, resulting from inelastic scattering, are symmetric with respect to the Rayleigh one, and two components can be identified: Stokes, with lower frequency than ν_0, and anti-Stokes, with higher frequency than ν_0. The frequency shift with respect to the incoming excitation is linked to the energy variation of the incoming photon. The nature of the Stokes and anti-Stokes components is described in the following. Inelastic light scattering can be described classically as the interaction between the light and a medium with dynamic fluctuations in its optical properties. These fluctuations couple with the incoming monochromatic electromagnetic field, by modulating its frequency. From a quantum-mechanical point of view, the process is an inelastic collision between incident photons and quanta of collective excitations, giving rise to creation or annihilation effects of photons and excitation quanta. Particularly, the incident photon (with energy $\mathrm{E}_0 = \hbar\nu_0$ and momentum $\mathbf{p} = \hbar\mathbf{k}_0$) is annihilated, and subsequently a scattered photon is created (with frequency Ω and wavevector $\mathbf{k}$), together with the creation or annihilation of a quantum of the medium collective excitations (with energy $\mathrm{E}_1 = \hbar\Omega$ and momentum $\mathbf{p}_1 = \hbar\mathbf{q}$). Within this framework, the scattering kinematics is expressed by the energy and momentum conservation:

$$\hbar\nu_0 - \hbar\nu = \pm\hbar\Omega \tag{2.11}$$

$$\hbar\boldsymbol{k_0} - \hbar\boldsymbol{k} = \pm\hbar\boldsymbol{q} \tag{2.12}$$

where the plus sign identifies the Stokes process, corresponding to the loss of energy of the scattered photon and the creation of an excitation quantum in the material, whereas the minus sign indicates the anti-Stokes process, where the observation of higher frequency scattered photons reveals the annihilation of an excitation quantum in the medium. The scheme of the interaction is sketched in fig. 2.6.

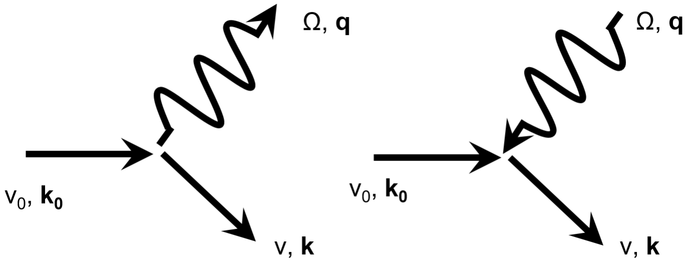

Figure 2.6: *Schematic representation of the Stokes (on the left) and anti-Stokes (on the right) processes occurring while light inelastically interacts with a material.*

The process can be thought as the crystal absorbing the incoming photon $\hbar\nu_0$, reaching a higher, non-stationary level (i.e. a virtual level, introduced only to easily describe the process) and emitting a photon $\hbar\nu$, finally coming back to a stationary state, see fig. 2.7. However, the two processes

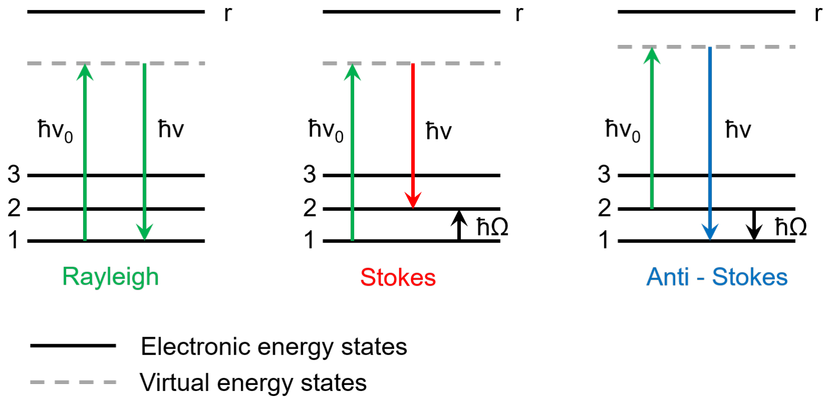

Figure 2.7: *In this picture, a schematic sketch of the simultaneous processes of absorption and emission of a photon are shown, for either the case of elastic (i.e. Rayleigh) and inelastic (Stokes and anti-Stokes) scattering.*

of absorption and emission happen simultaneously, and can not be separate in time. When the ground state before and after the perturbation is the same, is the case of Rayleigh scattering. However, even if with lower probability, the photon can lose energy or even increase its initial energy if finding the crystal in an initial excited vibrational state. In the first situation a Stokes process is promoted, whereas in the second case an anti-Stokes process happens. However, the probability of finding the system in an already excited state is lower, and for this reason the Stokes contribution has a higher intensity. Additionally, a resonance effect can be achieved when using an incoming radiation with frequency close to that of a real electronic transition of the medium (in fig. 2.7 labeled as r): as a result, the intensity of the diffused radiation increases, since a more efficient perturbation of the medium is achieved. This fact further explains the experimental evidence of different intensities between the Stokes and anti-Stokes line (I_s and I_{as} respectively), since the ratio between the electronic populations is proportional to the exponential factor exp $\frac{\hbar\Omega}{kT}$, and thus the $\frac{I_s}{I_{as}}$ ratio can be written as follow:

$$\frac{I_s}{I_{as}} \propto (\frac{\nu_0 - \Omega}{\nu_0 + \Omega})^4 exp\frac{\hbar\Omega}{kT}$$

A restriction exists on the range of wavevectors analyzable with the light scattering, that implies a selection rule for the Raman scattering to exist. Indeed, referring to equations 2.11 and 2.12, it is generally true that:

$$\boldsymbol{q} = |\boldsymbol{k} - \boldsymbol{k_0}|$$

This means that, for an incoming photon belonging to the visible range of the electromagnetic spectrum, $\mathbf{q} \approx 10^{-5}$ cm^{-1}. Being the lattice constant a usually on the order of 10^{-10} m, then $\mathbf{q} \ll \frac{\pi}{a}$. It this therefore clear that this method investigates modes with wavelength definitely higher with respect to the lattice constant, and thus belonging only to the first Brillouin zone. Thus, for a first-order light scattering event, only modes having q $\cong$ 0 can be excited. From a classical wave interpretation, the light is an electromagnetic wave bringing an oscillating electric field that can interact with the electrons of the medium by virtue of its polarizability. The perturbation of the electron cloud brings to a periodic charge separation called induced dipole moment. In light of this, the Raman selection rule can be reformulated: a Raman transition between two states is allowed only if the polarizability of the states is different. The dipole momentum induced by the electric field **E** is expressed as:

$$\mathbf{M} = \alpha\mathbf{E} + \frac{1}{2}\beta\mathbf{E}^2 + ... \tag{2.13}$$

where α is the electronic polarizability and β is a third-order tensor taking into account all effects with higher order than the first one. This means that the dipole induced momentum oscillates not just at the frequency ν_0 of the incoming light, but also at frequencies $\nu_0 \pm \Omega$, resulting in peaks in the spectrum located either at ν_0 (Rayleigh scattering) and $\nu_0 \pm \Omega$ (Raman scattering). Depending on the equilibrium configuration symmetry of either the crystal and the vibrational mode, it is possible to define active Raman modes (visible in the spectrum) and non-active Raman modes.

Finally, also a confinement effect can be observed in the Raman spectrum. This is a consequence of the relaxation of the selection rule when dealing with an amorphous or nanocrystalline material, due to reduction of the crystalline domain size. This results in peak broadening and shifting. In general, as the crystallites size decreases, a larger region of the dispersion relation in the Brillouin zone takes part in the scattering, thus all excitations with all wavevectors can be involved in the Raman process.

As mentioned at the beginning of the description of Raman spectroscopy, with the same instrumentation also the PL phenomenon can be observed. It is an electronic transition resulting from the interaction between the incident photon and the electronic bands of the material. In this process, the incident photon is truly absorbed by the medium, that is brought to a real stationary state with a proper lifetime. After a certain period, the system decays to a lower energy state and, if it is different from the initial energy state, a photon is emitted, with frequency lower than the excitation one. On the contrary of Raman scattering, two real consecutive events happen. This explains a quenching effect observable during the PL process, responsible for the removal of energy from the excited state in the period between the absorption and emission. The PL is extremely influenced by the presence of chemical elements in the physical environment interested in the transition. As an electronic transition happening in a bulk material, it is usually identify by the presence of broad bands in the spectrum. However, some specific case of impurities can be treated as atoms in a matrix, and thus have their own PL peak signature. Since the spectral region interested in such kind of interaction extends from IR to visible wavelength, it is common to observe PL bands along the whole spectrum, whereas Raman contributions are localized in the 0 - 3000 cm^{-1} range of the spectrum.

To conclude, Raman spectroscopy can be a very sensitive technique for characterization of several materials, and nowadays is among the most employed characterization techniques for carbon-based systems. Indeed, several features can be derived by a proper interpretation of Raman spectrum, regarding the hybridization of carbon atoms, the presence of stress states, impurities, the structural disorder of the system and so on. Also, the PL contribution in the spectrum brings important information about chemical impurities and defects of the crystalline structure in the carbon system. For a detailed description of Raman and PL spectrum of different kind of carbon systems refer to the Appendix A.

Chapter 3

Aims of the work

3.1 Motivations

Diamond is a promising material for different kind of technological applications. As anticipated in chapter 1, among the possible applications, diamond solid-state detectors are an appealing alternative to common silicon-based technology for radiation detection purposes, due to their better performance and higher resistance especially in harsh radiation fields. However, their reduced availability limits their use. As already introduced in chapter 1, diamond exceptional properties are directly linked to its unique crystalline structure. For this reason, the artificial synthesis of diamond is a topic of investigation by far. The understanding and control of diamond growth dynamics is essential to achieve a material with tailored and specific properties, especially on different substrate materials, that in turn allows its application in various fields. Both single-crystal and polycrystalline diamond can be synthesized, and are considered as interesting candidate materials for radiation detectors. Single-crystal diamond represents the ideal one, but due to expensive costs and very strict requirements in its synthesis, the availability is limited. Indeed, crystalline perfection is required, and limits in the choice of the substrate are found: as already introduced in chapter 2, diamond metastability condition (with respect to other carbon allotropes), its high surface energy and peculiar crystalline structure imply that there is a very few compatibility with other materials. For these reasons, polycrystalline diamond deposition is investigated too, since a lower crystalline perfection (and thus a lower performance) could be accepted for certain applications if costs are definitely reduced (e.g. where no spectroscopic purposes are pursued in radiation detection application). Additionally, polycrystalline diamond discloses the possibility of performing depositions on a wider range of substrate materials, thus opening the chance of applying this material in different fields. Depending on the grain size, different kind of polycrystalline diamond can be defined, each one with well-defined properties. Recently, nanocrystalline structures (grain size less than 100 nm) are attracting great attention for application in several fields, from the mechanical to the biomedical one. The typical nanocrystalline structure with sp^3 crystalline phase embedded in a matrix of sp^2 amorphous and disordered carbon provides this material a number of interesting properties. Regarding the nuclear applications, the idea of producing nanocrystalline diamond (NCD) devices whose performance, over long time exposure to radiation, are potentially supposed to be not far from that of single-crystal one, is an appealing approach, being polycrystalline (and thus even nanocrystalline) diamond synthesis cheaper and easier than that of single-crystal one. However, even if poly- and nanocrystalline diamonds permit flexibility regarding the choice of the substrate material (on the contrary to the single-crystal diamond), if a substrate different from diamond itsef is used, an intermediate step of nucleation is foreseen before diamond growth sets on, that is difficult to be achieved and can lead to unbearable incubation time. Several issues limit the understanding of the dynamics of the early stages of diamond growth on substrate materials with different properties, even for polycrystalline diamond. Indeed, different substrate materials can have a different interaction with carbon, and usually a substrate pre-treatment is required in order to achieve a uniform coverage of the substrate and satisfactory deposition time.

Plasma-enhanced chemical-vapor deposition (PECVD) is the main industrial process exploited to produce diamond, either as a single-crystal or polycrystalline. Additionally, microplasma devices are attracting great attention lately for a variety of applications, thanks to the unique properties of plasma created in specific conditions typical of these devices. Even if PECVD technology nowadays is quite consolidated, the coupling of this chemical deposition technique with the use of a microplasma opens to a new way for nanomaterials synthesis, where the properties of the peculiar plasma obtained deeply influence the deposition process. In this frame, microplasma devices have already proved to be easy, cheap, versatile and with a high growth rate with respect to common CVD processes. For these reasons, microplasma-based CVD techniques are particularly suitable for the investigation of NCD deposition and for the understanding of the dynamics behind this process. Additionally, the creation of proper electrodes in order to increase the charge collection is a fundamental topic of investigation. The performances of the device are dependent on the appropriate fabrication of electrodes at the diamond - electronic chain interface indeed. Normally, metal-based contacts are fabricated by means of several deposition methods (e.g. sputtering, evaporation, etc), but the concept of an all-carbon detector with graphitic contacts is earning much popularity, being graphite the stable allotropic form of carbon with excellent electrical properties. Finally, about single-crystal diamond for radiation detection, even if promising results have already been achieved about their performances, their behavior in specific radiation environments (e.g. high-energy particles accelerators, fusion reactors, etc) still needs to be deeply investigated, since a *polarization effect* has been observed, affecting the device collection properties. In light of these observations, the specific goals of this thesis work will be presented in the next section.

3.2 Specific goals of the thesis

The research activity of this work can be summarized in two main subjects:

a. investigation of the growth dynamics of NCD with a direct-current micro-plasma technique and specific characterization tools;
b. investigation of relevant issues related to diamond detectors, namely i) fabrication of appropriate carbon-based contacts on polycrystalline diamond substrates and ii) analysis of the *polarization effect* of single-crystal diamond detectors after α and fast neutron irradiation.

a. Regarding the investigation of NCD films growth, the aims are elucidated in the following.

- Identification of the appropriate deposition conditions for the investigation of the early stages of diamond growth mechanisms. Indeed, basing on available literature data about carbon structures grown with the DC-μP [97], it is already known how to select deposition parameters to achieve different diamond morphologies and structures. For this reason, process conditions pertinent to the aim of investigating the early stages of diamond growth mechanism have been chosen. Particularly, because of the scientific interest in NCD applications, process conditions able to obtain this structure have been selected.

- Investigation of the dynamics of the early stages of growth of NCD on various substrate materials showing different interaction with carbon, and thus potentially evoking various kind of mechanisms depending on carbon diffusivity in the substrate and tendency in chemically react with it. Particularly: molybdenum, silicon and tungsten were used, having a low solubility with carbon but, at the same time, high tendency in forming a carbide compound, nickel and iron because having high solubility with carbon and, finally, also a thin, nanostructured rhodium film deposited on silicon were employed as substrate material, being a never explored substrate for diamond deposition.

- Investigation of the dynamics of the early stages of growth of NCD without performing substrate pre-treatments in order to analyze the natural growth on the bare element.

- Characterization of the first stages of growth with suitable characterization techniques, in particular using Raman spectroscopy with a systematic approach. Indeed, even if several characterization tools have been used for the investigation of the first stages of diamond growth, a systematic study of this issue with Raman spectroscopy is still missing. Additionally, being NCD a complicated system with both sp^2 and sp^3 carbon phases that can have different Raman cross-section with respect to the laser wavelength used to excite (see Appendix A), the exploitation of different wavelengths for Raman spectroscopy allows to obtain a complete characterization of sample.

- Investigation of the possibility of producing NCD films with relevant thickness with the DC-μP, for application as radiation detectors.

b. The second subject regards a preliminary and methodological work aiming at investigating specific topics about diamond detectors devices, with a material science approach. Main goals of this work are:

- investigating the possibility of fabricating metal-less graphitic contacts on polycrystalline diamond substrates with a physical vapor deposition technique, i.e. the pulsed-laser deposition technique (PLD);

- introducing a characterization strategy of the crystalline structure of single-crystal diamond detectors in order to investigate the *polarization effect*. For this reason, α irradiations were performed on single-crystal diamond detector, and sample was characterized before and already after irradiation, being the *polarization effect* due to α particles subjected to recovery after a certain time that irradiation is stopped. Also, neutron irradiations were performed on single-crystal diamond, to evaluate the damage in the crystalline structure that, in turn, can induce a *polarization effect* in diamond that is known to be permanent as the structural damage. Again, sample was characterized before and after irradiation.

To achieve all the mentioned specific goals, a dedicated methodology was used. In particular, chapter 4 is devoted to describe the methodology employed for the first subject of the work, with the description of either the deposition set-up and the characterization tools used for NCD synthesis and characterization, and the justification of the choice of process parameters. Results about the investigation of the dynamics of the early stages on NCD growth are addressed in chapter 5, with a dedicated discussion at the light of literature about diamond synthesis. Regarding the second topic of the work, chapter 6 describes the approach exploited for the deposition of metal-less contacts on polycrystalline diamond with the PLD, and relevant results are shown. Chapter 7 presents the methodology behind the investigation of α and neutron irradiation exposure of single-crystal diamond, with a discussion of the results obtained. The conclusions and future perspectives of the work are presented in chapter 8.

Part II

Growth of nanocrystalline diamond (NCD) with DC-μP

Chapter 4

Methodology

4.1 Introduction

This chapter focuses on the methodology used to achieve the goal of the investigation of the dynamics of the early stages of PCD deposited with the DC-μP. In section 4.2 the deposition set-up is presented, justifying also the choice of process parameters in light of the thermodynamic model introduced in chapter 2, and in section 4.3 the characterization techniques used for diamond samples are shown.

4.2 DC-μP device for NCD deposition

The deposition of NCD was performed using a direct-current micro-plasma (DC-μP) device, belonging to the family of the plasma-assisted CVD techniques, and schematically depicted in fig. 4.1 [133]. It consists of an in-house designed vacuum chamber of stainless steel, a plasma generating system and a gas supply system. The vacuum chamber is evacuated by a primary rotary pump (Pfeiffer) and a turbomolecular pump (Varian V70). The chamber pressure is maintained at the desired pressure with a feedback control valve (MKS 250). The main feature of this experimental set-up is the stainless steel column with 178 μm inner diameter capillary tube that acts as the micro-hollow cathode allowing the gas inlet used to create the flow-stabilized micro-plasma jet. The anode and substrate holder is a 0.1 mm thick molybdenum strip placed about 1 mm far from the capillary tube, heated by joule effect and keeping the sample at the desired temperature. The substrate temperature is monitored by a thermocouple placed on the back of the substrate holder. The decision of such configuration for temperature measurement is justified in the following. First, placing the thermocouple on the substrate and near

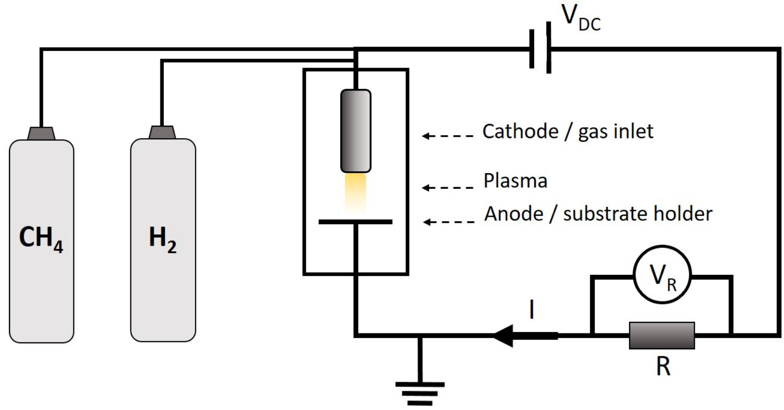

Figure 4.1: *A schematic representation of the DC-μP deposition set-up is shown: the plasma jet is confined under the micro-hollow cathode.*

the plasma-jet shows some technical problems because the thermocouple can act as a "virtual anode": this implies the formation of "parasitic discharge" between the thermocouple and the cathode. Second, experimental tests of temperature measurement have already been made, placing the thermocouple close to the plasma jet position, heating the substrate holder at the desired temperature and turning the plasma cyclically on and off: they showed a temperature difference of about 50 °C that is stricly dependent on the power supplied by the plasma on the substrate, i.e. on the I-V values set at the plasma generating system. This power is around 4 W, which is a small value with respect to the 120 W supplied by joule effect. Due to the fact that the total thickness of the sample plus the substrate is very thin (around fractions of mm), we estimate that the temperature gradient across the sample is less than the above 50 °C. In summary, placing the thermocouple on the back side of the substrate holder, just below the jet, permits a more reliable and practical measurement of the temperature. For all the relevant calculations see Appendix B. The carbon source is methane gas mixed with hydrogen. The plasma volume shows a dimension comparable to that of the micro-hollow cathode (i.e. 178 μm diameter x 1 mm thick): for this reason, any measurement related to plasma diagnostic is extremely difficult and needs specific dedicated facilities. The cathode shape is the result of an optimization study devoted to minimizing the pollution in the deposition due to the cathode erosion by the highly reactive plasma, and can be found in [94], together with the I-V characteristics curves experimentally obtained for the plasma. A photograph of the vacuum chamber and the plasma microjet set-up in reported in fig. 4.2.

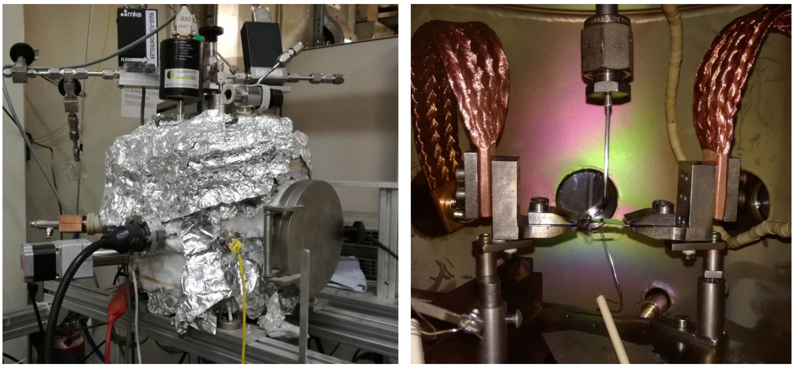

Figure 4.2: *Pictures of the experimental equipment used in this work for diamond deposition: the vacuum chamber on the left and the microplasma jet set-up on the right.*

4.2.1 Choice of process parameters

According with one of the goals of this thesis regarding the investigation of the first stages of NCD growth on different materials, the following substrates were used:

- Mo, Si and W because of the strong interaction they have with carbon, resulting in a marked tendency in forming spontaneously a carbide compound prior to diamond deposition at the interface, and low carbon diffusivity;

- Fe and Ni because of the weaker interaction they have with carbon but, at the same time, higher diffusivity than Mo, Si and W. Additionally, both these materials have a carbide form but it should not form at the chosen deposition conditions of pressure and temperature [134], and particularly Fe is widely considered a non ideal substrate for diamond deposition [104, 106, 135];

- Rh because a never used substrate for diamond deposition, with the intention to investigate this new material behavior. Moreover, whereas for the other substrates polycrystalline films and single-crystal raw materials were used, for Rh a 1 μm columnar film deposited on Si was used, to investigated the diamond growth even on nanostructured films.

Only conductive materials were chosen, because of the intrinsic limit of the dc plasma generating system. Values of substrates diffusivity with carbon are reported in tab 4.1. Unfortunately, for the case of Rh no available data were found. Taking into account all the considerations mentioned in the chapter 2 regarding diamond deposition, the gas mixture used in this work

Substrates	**Si**	**Mo**	**W**	**Fe**	**Ni**
Diffusivity [cm^{-2} s^{-1}]	$7 \cdot 10^{-15}$	10^{-11}	10^{-13}	$8 \cdot 10^{-7}$	$2 \cdot 10^{-8}$

Table 4.1: *Values of carbon diffusivity in different substrate materials calculated at 800* °C*. For Rh, no available data are found.*

is made of 0.5 sccm of methane gas mixed with 100 sccm of hydrogen, in order to create the "super-saturated" environment for hydrogen. To obtain the peculiar plasma typical of this device, together with favorable conditions for diamond growth kinetics regarding precursors mole fraction, the other process parameters must be chosen in order to be inside the four-sided shaded region of fig. 4.3, delimited by the activated graphite and diamond stability lines and the green curves identifying suitable mole fraction values for precursors. For these reasons, the "pd" couple of values

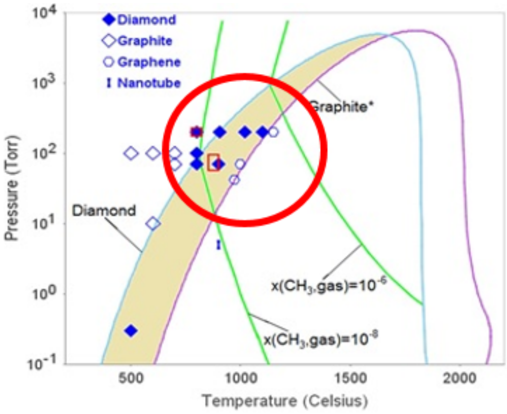

Figure 4.3: *Pressure - temperature C - H phase diagram introduced in chapter 2 and used to find the best process conditions for NCD deposition. Particularly, the four-sided region in which parameters were chosen is highlighed.*

was chosen with the micro-hollow dimension at 178 μm, and the pressure chamber fixed at 200 Torr. Additionally, a temperature of 960 °C were chosen for diamond deposition. Besides the reasons regarding the intention to obtain NCD rather than other solid forms of carbon (already anticipated in chap. 3), this value of temperature was chosen also because being not so high, thus avoiding thermal stresses to the machine components and being acceptable for most substrate materials. Finally, samples were grown with increasing deposition time, ranging from few minutes to hours in order to explore both the first stages of growth and the possibility of growing films of practical interest with the DC-μP. All substrates have been previously

cleaned with a sonic bath in hexane and deionized water, then placed under vacuum in the deposition chamber for several hours. No substrate pre-treatment was performed, since among the aim of these works there is the intention to investigate the natural diamond growth on several substrates.
The range of operating conditions and deposition time are summarized in tab. 4.2 and 4.3.

Substrates	Mo, Si, W, Rh, Fe, Ni
Feed Gas	CH_4, H_2
Excitation source	Micro-plasma direct-current discharge
Micro-hollow dimension	178 μm
Substrate temperature	960 °C
Total pressure	200 Torr
Φ CH_4	0.5 sccm
Φ H_2	100 sccm
Supply voltage	600 V
Plasma current	10-12 mA

Table 4.2: *Range of operating conditions adopted for diamond deposition with the DC-μP device.*

Substrate	**Deposition time**
Mo	2.5 min, 5 min, 10 min, 15 min, 30 min
Si	7 min, 15 min, 30 min, 1 hour, 2 hour
W	5 min, 15 min, 30 min, 1 hour
Fe	5 min, 15 min, 30 min, 1 hour
Ni	5 min, 15 min, 30 min, 1 hour
Rh	5 min, 15 min, 30 min, 1 hour

Table 4.3: *Substrates used for diamond deposition and deposition time.*

4.3 NCD characterization

The characterization of diamond was extensively performed for both morphology and structure, in order to give a complete panorama of samples features. Scanning electron microscopy (SEM) and Raman spectroscopy were used in this work as main characterization tools, for morphology and crystalline structure respectively. Also, as a source of additional information, X-ray diffraction (XRD) was used.

Morphological investigation. Scanning electron microscopy was used to derive morphological information about diamond samples. SEM micrographs were taken using a high resolution Field Emission ZEISS Supra 40 scanning electron microscope based on the Gemini column. The accelerating voltage ranges from 1 kV up to 30 kV. The sample holder can be moved thanks to five software-controlled motors (x, y, z, rotation and tilt).

Analysis of the crystalline structure. Among the various characterization techniques available, Raman spectroscopy represents one of the best when dealing with carbon-based materials [125, 126, 129], especially with a multi-wavelength approach and in specific combination with the DCμP deposition technique [136], allowing to identify the different allotropic forms of carbon. As already shown in chapter 2, many works in literature report the investigation of diamond growth with different surface characterization techniques such as XRD [62] or XPS [56, 61], but still a systematic characterization of the first stages of diamond growth with Raman spectroscopy is missing. In this work, Raman spectroscopy is performed at room temperature both for the UV and visible range, with two different systems. Visible Raman spectroscopy is performed by a Renishaw InVia micro-Raman spectrometer equipped with an Ar laser, tuneable on a green (514.5 nm, 2.41 eV) or blue (457 nm, 2.71 eV) line, two gratings (1800 and 2400 g mm^{-1}), two edge filters (cut-off at 100 cm^{-1} for the green line and at 150 cm^{-1} for the blue line) and a Peltier-cooled charge coupled device (CCD) camera, allowing spectral resolution of about 3 cm^{-1}. UV Raman measurements are acquired using a Renishaw 2500 microscope system, including a He-Cd laser, emitting at 325 nm (UV excitation) with edge filter cut-off at 150 cm^{-1}. Regarding XRD, measurements were performed using a Panalytical X'Pert PRO X-ray diffractometer working in Bragg-Bretano $\Theta/2\Theta$ configuration, and using monochromatic copper K_α radiation ($\lambda = 1.54$ Å).

Chapter 5

Investigation of the dynamics of NCD growth

5.1 Introduction

In this chapter, the results regarding the investigation of the early stages of NCD growth on different substrate materials are presented.
Following the temporal and logic development of this thesis project, the first results shown in section 5.2 are about diamond deposition on Si and Mo, two substrates widely used and of relevant interest for NCD deposition. Following these first results, in section 5.3 the investigation of the early stages of diamond growth on substrates with different interaction with carbon with respect to Si and Mo is presented. Section 5.4 is devoted to analysis of results. Finally, the first promising outcomes regarding the possibility of using the DC-μP for deposition of diamond films are discussed in section 5.5.

5.2 Early stages of NCD growth on widely used substrates: Mo and Si

In the first part of the work, the investigation of the dynamics of the early stages of NCD growth on Si and Mo is the main topic. Diamond samples were grown with increasing deposition time, ranging from few minutes to hours (see tab. 4.3 of the previous chapter). The deposition conditions adopted have already been justified in chapter 4. Thank to the unique feature of the DC-μP device to perform very small spot depositions (being the plasma confined into the micro-hollow dimension), it was possible to grow different diamond samples on the same substrate and while the same experiment was running, simply translating with a mechanical apparatus the substrate holder with respect to the micro-hollow cathode. A picture of a typical sample grown on Si is shown in fig. 5.1, together with a representative SEM top view of one of the deposits. The deposition appears to be higher in the center of the spot (i.e. where the plasma is, see right side of fig. 5.1), with deposition diameter increasing with growing time, even though the plasma plume diameter is always around 178 μm (as the micro-hollow cathode). We can thus assume that, outside the micro-hollow diameter, an ordinary thermal CVD deposition occurs. For this reason, all characterization data were collected in the central region of the deposition. The measurement procedure was such that several measurements were performed on different points of the same deposit. However, no significant differences were found from a point to another of the same deposit. For this reason, for the sake of simplicity, only one measurement for each deposition time is reported.

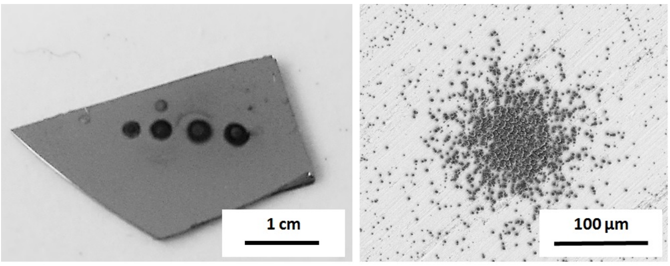

Figure 5.1: *On the left, picture of different deposits on Si substrate grown with increasing deposition times using the DC-μP set-up. On the right, SEM image of a top view of a deposit on Si substrate.*

5.2.1 Morphological characterization

SEM images of diamond deposited on Mo and Si raising deposition time are shown in fig. 5.2 and 5.3. On Mo substrate (see fig. 5.2), small and isolated aggregates showing dimensions around 1 - 2 μm with well-faceted features are visible already after few minutes of deposition. As the deposition time is increased, the aggregates grow up both in number and dimension till they coalesce after 15 minutes of deposition. Their final dimension is about 10 μm and their morphology appears to be rough. For diamond grown on Si substrate (fig. 5.3) the growth kinetics seems slower; few agglomerates with dimensions on the order of 200 nm start to appear after 7 minutes of deposition, and a micrometric dimension is revealed only after 15 minutes. The coalescence in a compact, polycrystalline film is reached within 1 hour, with final dimension of grains around 5 μm. The same result is achieved on Mo but after 30 minutes of deposition. As can be deduced from SEM images, the morphological evolution of diamond

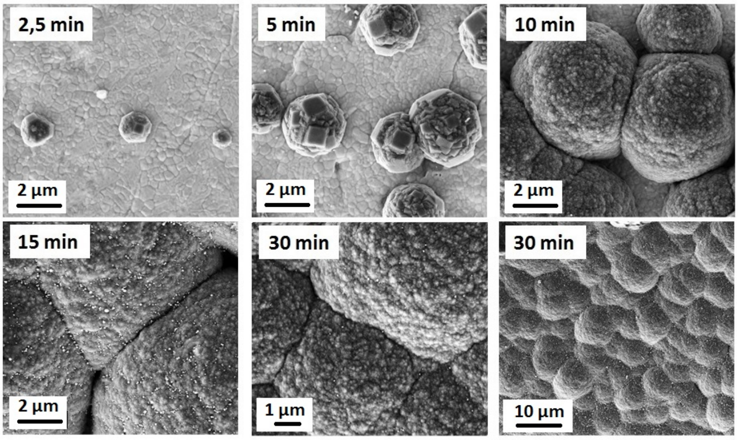

Figure 5.2: *SEM images of diamond samples grown on Mo increasing deposition time. The last picture is a magnification of the 30 minutes deposition.*

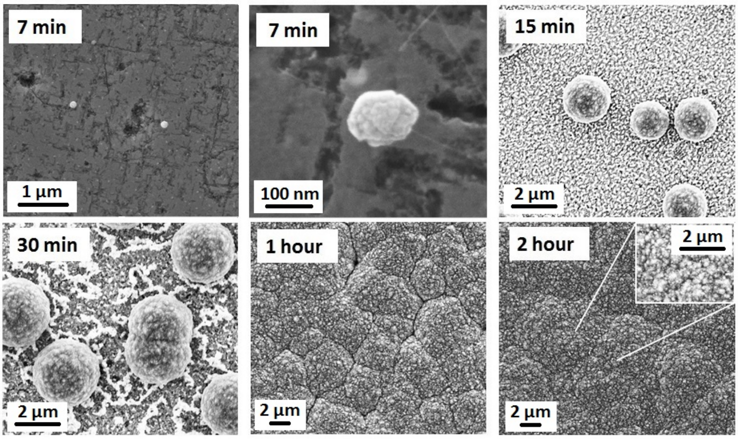

Figure 5.3: *SEM images of diamond samples grown on Si increasing deposition time. The second picture is a magnification of the 7 minutes deposition.*

films shows evident similarities between the two substrates, although a slower kinetics is found for diamond deposited on Si.

5.2.2 Characterization of the crystalline structure

Raman spectroscopy

Raman spectra of diamond deposited on Mo and Si with increasing deposition time and taken both with visible (λ = 457 nm) and UV laser wavelength are reported in fig. 5.4. Motivations justifying the choice of Raman wavelength can be found in Appendix A, together with a detailed description of main Raman features of carbon-based systems. Since the optical microscope of UV Raman permits a lower magnification than that of the visible one, it was impossible to find the 2.5 minutes of deposition on Mo, being extremely small.

For Mo substrate (inset a) of fig. 5.4), at 2.5 minutes of growth visible Raman spectrum reveals the presence of disordered graphite with a broad G peak less intense than the D peak. At 5 minutes of deposition, the spectrum is characterized by two, well-distinguishable D and G peaks with a Lorentzian shape: the higher intensity of the G peak with respect to D peak, together with its sharpness, are the signature of crystalline graphite. The small shoulder of the G peak is due to D' contribution. At 10 minutes of deposition, the graphite signal is superimposed by two broad bands typical of sp^2 amorphous carbon, and the first-order diamond line (here labeled "d") starts to appear. After 15 minutes, the spectra shape becomes typical of NCD film, with clearly visible contributions from *trans-polyacetylene* (t-pA) with ν_1 and ν_3 peaks. UV Raman spectra taken on Mo (inset c) of fig. 5.4) confirm the graphitic nature in the early stages of growth: the G peak is detected at the same Raman shift of visible Raman and the D peak is nearly absent. Moreover, the diamond line is easily appreciated already after 10 minutes. For sample deposited on Si (insets b) and d) of fig. 5.4), crystalline graphite is found at 7 minutes of growth. As deposition time increases, the D and G peaks are replaced by broader bands in both UV and visible Raman spectra, and the typical aspect of the NCD is revealed. Deposition were stopped at 30 minutes on Mo and 2 hours on Si. The criterion used is that, basing on Raman measurements observations, from 30 minutes of deposition on Mo and from 2 hours of deposition on Si the Raman spectra show no more evolution.

For the 7 minutes of deposition on Si, an additional feature is observed in the range 900 - 1000 cm^{-1}, that is ascribed to the second-order peak of Si substrate. However, since from literature it is quite common to attribute the nucleation of diamond on Si and Mo to the formation of carbide compounds, and since it is known that silicon carbide can be present in different polytypes [137], many of them showing a strong peak around 790 cm^{-1} accompanied by a second weak peak around 900 - 1000 cm^{-1}, a

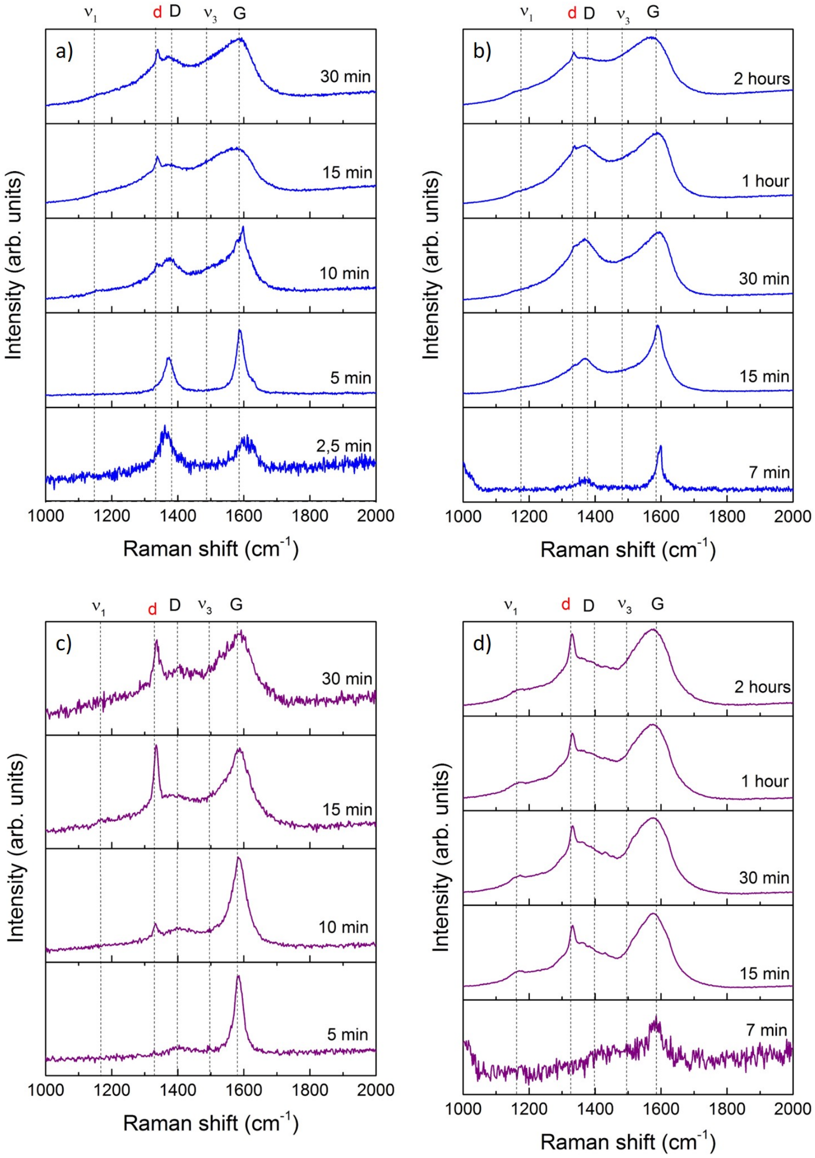

Figure 5.4: *Visible ($\lambda = 457$ nm) and UV ($\lambda = 325$ nm) Raman spectra of polycrystalline diamond grown with the DC-μP apparatus with increasing deposition time. Blue color is used for visible spectra and violet color is used for UV spectra. Particularly, insets a) and b) show visible Raman spectra of diamond on Mo and Si respectively, whereas insets c) and d) report UV Raman spectra of diamond grown on Mo (inset c)) and Si (inset d)). Typical carbon features are highlighted.*

dedicated analysis in the range 400 - 1100 cm^{-1} was performed, see fig. 5.5. From this measurement, the peak related to the first-order of Si is found in its expected position (521 cm^{-1}), whereas no evidence of silicon carbide Raman peaks is detected.

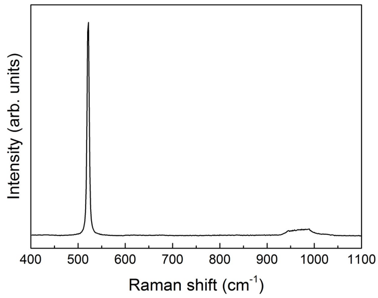

Figure 5.5: *Raman spectrum of diamond grown on Si for 7 minutes limited to the frequency range 400 - 1100 cm^{-1}.*

X-ray diffraction

With Raman measurements no signal of silicon carbide is found, whereas molybdenum carbide is known to be Raman inactive. For these reasons, XRD measurements were performed, in order to get evidence about carbides formation, also exploiting the higher depth sensitivity of XRD (several microns) compared to Raman spectroscopy (around hundreds of nanometers in presence of absorbing sp^2 phase). XRD spectra are reported in fig. 5.6, for samples deposited on Mo (on the left) and on Si (on the right) respectively. Measurements were taken on the whole sample and thus can not be referred to a specific deposition time.

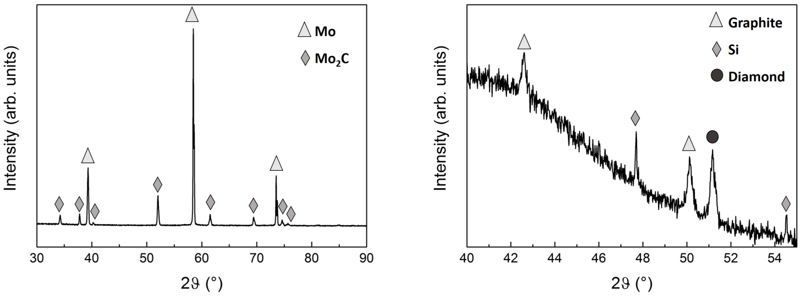

Figure 5.6: *XRD of diamond on Mo (on the left) and on Si (on the right).*

For the case of diamond deposited on Mo substrate, several sharp peaks attributed to molybdenum carbide are found, confirming the formation of a crystalline form of this compound. For sample deposited on Si instead, no signal related to silicon carbide is detected. Furthermore, two peaks at 42.6° and 50.1° and attributed respectively to graphite (1 0 0) and (1 0 2) are found, whereas the peak at 51.1° is assigned to diamond (2 0 0): this peak has already been attributed in literature to polycrystalline diamond films with a typical ballas morphology [107]. Using Scherrer's formula on the diamond (2 0 0) peak, it is possible to estimate a crystallite domain size of about 45 nm.

5.3 Expansion of the analysis on less favorable substrates: W, Ni, Fe and Rh

As anticipated, Mo and Si were not the only substrates taken under consideration for this project. Indeed, since one of the main goal is to generally investigate the first stages of diamond growth on several substrate materials with different behavior regarding carbon - substrate interaction, it seemed so much natural to extend the investigation to other materials, i.e. W, Ni, Fe and Rh. The reason why these materials were used is already justified in chapter 4.

For the considered substrates, the same deposition conditions used for Mo and Si were adopted. Different deposition spots were deposited on the same substrate, with increasing deposition time. SEM and Raman were used again as main characterization tools. Particularly, in this case only visible Raman measurements were performed. Indeed, in this part of the work the focus was on the early stages of growth, where graphite was found, and for this reason there was no need to highlight diamond features with the resonant behavior shown at UV wavelength.

5.3.1 Morphological characterization

SEM images of diamond deposited on Ni, Fe, W and Rh are shown in fig. 5.7. Since the aim of this work is to focus on what happens in the early stages, SEM pictures of depositions performed at 5 minutes are shown. However, since the use of these substrate materials with this deposition device represent something new and never explored, also pictures at 30 minutes are shown, as representative of the fact that diamond was deposited even on these less favorable substrates with the DC-μP. Thus, for W, Fe, Ni, and Rh, only diamond deposited at 5 minutes and 30 minutes were characterized. As for the case of Mo and Si, few and isolated agglomerates can be seen on all substrates for 5 minutes of deposition. The morphology is well-faceted but with different grains dimension, namely around 2 - 3 μm for W, slightly smaller and around 1 μm for the other

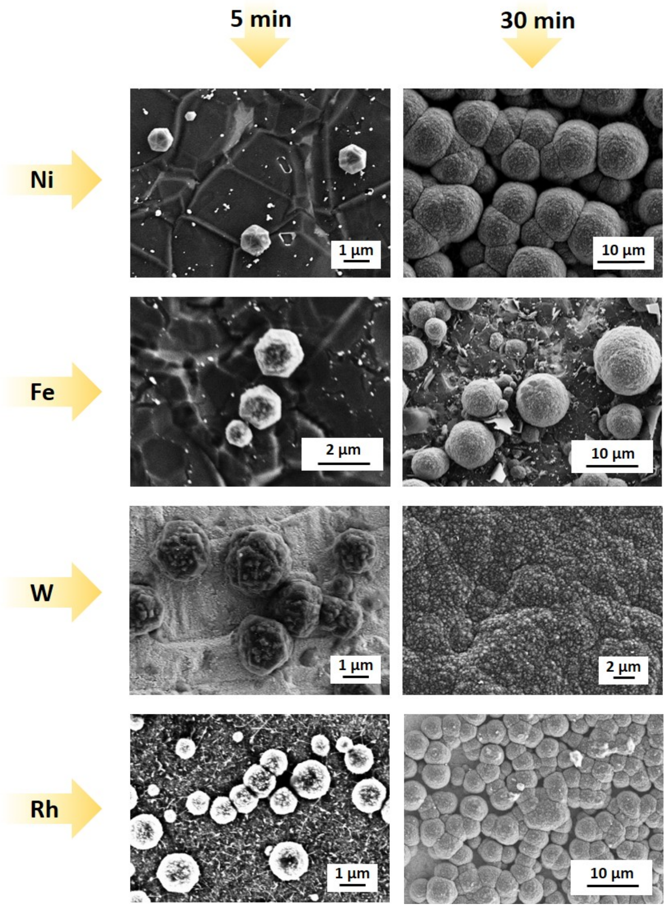

Figure 5.7: *SEM images of diamond grown on Ni, Fe, W and Rh for 5 minutes and 30 minutes.*

substrates (i.e. Ni, Fe and Rh). Looking at pictures taken at 30 minutes of deposition, the first evident conclusion regards the fact that a nearly continuous deposition was found on all substrates, with the only exception of Fe, where few and isolated aggregates are still visible at this time. However, by looking at SEM image of diamond deposited on Fe for 1 hour (see fig. 5.8 where a magnification of the central region of deposition is shown on the left and the top view of the deposit on the right), a nearly continuous ballas-like morphology was found even on Fe. For the specific case of Fe, it is worth noticing that no delamination occurred after substrate cooling. This can be attributed to the poor homogeneity of the deposit (see fig. 5.8 on the right): in such a case, stress can relax at voids and grain boundaries, preventing delamination from the substrate. This

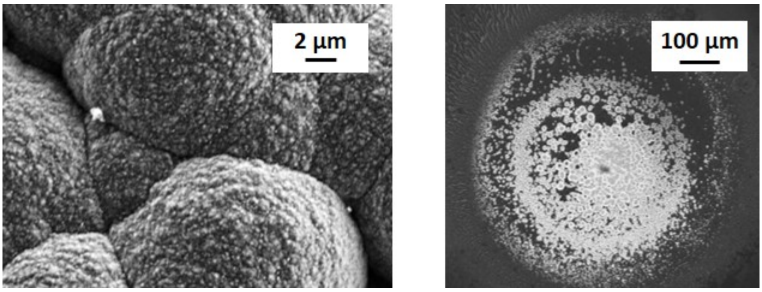

Figure 5.8: *SEM images of a magnification (on the left) and the top view (on the right) of NCD grown with DC-μP on Fe substrate for 1 hour of deposition time.*

result is significant for the specific case of iron, since Fe-based materials are extensively considered non-ideal material for direct coating of diamond without the deposition of an appropriate interfacial layer increasing diamond adhesion and preventing its peeling off after substrate cooling; Fe has indeed a catalytic behavior with respect to sp^2 formation, and this is worsened by the high diffusivity that carbon has in this material, leading to difficult and long-time formation of clusters with the critical size for diamond nucleation [104, 106, 135, 138, 139]. In literature some positive results have been conversely reported about direct coating of diamond on stainless steel: problems typical of diamond growth on ferrous materials such as graphitization, long incubation time, substrate softening and poor adhesion have been overcome by finely tuning a specific deposition process at low temperature [140, 141]. Considerably, in this work no interlayer deposition has been intentionally performed on Fe previously to diamond growth, and the process temperature used is in the range usually employed for diamond deposition with a PECVD technique.

5.3.2 Characterization of the crystalline structure

Raman spectra of diamond deposited on Ni, Fe, W and Rh for 5 and 30 minutes are shown in fig. 5.9. Again, as for Si and Mo, no diamond signal is detected at 5 minutes of growth, even if the lateral resolution of the instrument allows a direct measurement on the agglomerates shown in fig. 5.7 (the Raman laser spot has dimension comparable to that of the agglomerates): however, it is useful to recall that this result can be a combined effect of the scarce amount of diamond phase and the non-ideal (with respect to sp^3 resonance) Raman wavelength used to excite. Additionally, all spectra shows typical features of graphite, with G peak at 1582 cm^{-1} and D peak at 1370 cm^{-1} (as expected using λ = 457 nm), except for Ni substrate where no D peak is found. From the analysis of these peaks it is possible to characterize the defectivity of graphitic layers

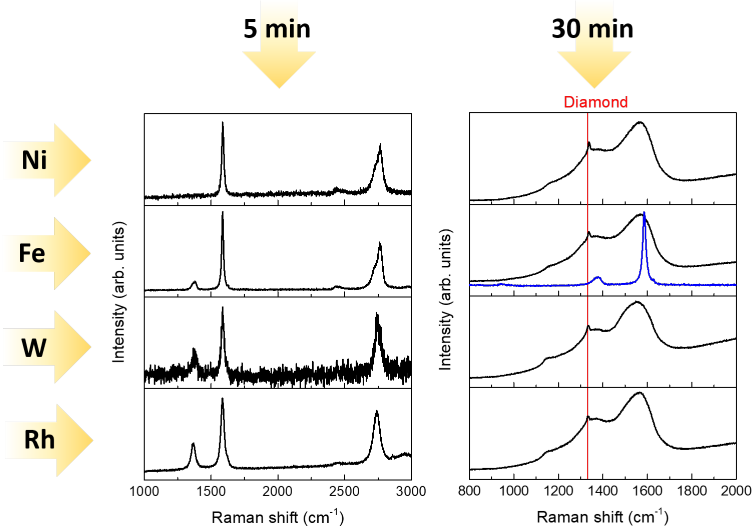

Figure 5.9: *Raman spectra of polycrystalline diamond grown on Ni, Fe, W and Rh for 5 minutes and 30 minutes. The blue spectrum for the 30 minutes diamond grown on Fe is a measurement taken directly on the substrate.*

[142]. The third Raman feature found at about 2740 cm^{-1} is the 2D peak, whose properties are related to the number and stacking order of graphitic layer, as already explained in Appendix A [136, 143, 144]. Regarding 30 minutes of growth, Raman spectra shows typical features of NCD: the d peak at 1332 cm^{-1} reveals the presence of sp^3 crystalline phase, and is accompanied by D and G bands, and also ν_1 and ν_3 contributions suggesting the presence of *trans-polyacetylene* at grain boundaries. This result agrees with the ball-shape morphology highlighted by SEM characterization (see fig. 5.7). For the case of Fe, which is the only one at 30 minutes where diamond agglomerates are still far from coalescence, Raman measurements directly on the substrate around diamond particles were possible: the result is the blue spectrum of fig. 5.9, that again confirms the presence of the graphitic system under the diamond agglomerates.

5.4 Discussion of results

5.4.1 Morphology evolution

Diamond agglomerates of the early first stages present well-faceted features, but with different dimensions: micrometric agglomerates on Mo, W, Fe, Ni and Rh and smaller agglomerates, on the order of hundreds of nanometers, on Si (fig. 5.2, fig. 5.3 and fig. 5.7). As the deposition time increases, the Raman spectra, together with the ball-shape of diamond agglomerates, are typical of the ballas diamond morphology [130]. Since diamond morphology is related to the deposition temperature [97], we assume that this evolution in morphology can be attributed to a small temperature gradient between the substrate, where the heating system is supplied, and the top of the diamond agglomerates. In this way, the deposition temperature detected on the top of the film may be slightly lower, and thus not sufficiently high for microcrystalline shaped diamond synthesis. Particularly, regarding the ballas morphology obtained, few considerations can be drawn. It is already known from literature [105, 145–147] that well-faceted diamonds grow under specific deposition parameters, but if these conditions are not respected, for example the above parameters are not maintained along the whole deposition, the favorable conditions for well-faceted growth are no longer respected and then the typical ballas morphology is found. Particularly, the growth of diamond (111) and (100) facet is controlled by C_2H_2 and CH_3 precursors, respectively. This means that, for a given CH_4/H_2 flux ratio and deposition pressure, the precursors mole fraction governs the obtained morphology over a wide range of temperature. In such a range, a temperature value exists in which an inversion of the main precursor contribution is achieved [148]. If the deposition temperature is around this "inversion value", an uncontrollable and continuous local change of the concentration of the two main precursors at the surface causes the known twinning effect [149], responsible for the ballas-like morphology. It is thus reasonable supposing that, for our case, the deposition temperature is near the inversion value at the chosen flux ratio and deposition pressure. Finally, once the ballas morphology is obtained, the growth proceeds radially up to the coalescence stage, where a continuous film is formed [114]. Finally, we exclude that the ballas morphology depends on the substrate material, since it would be reasonable expecting different diamond morphologies for substrate materials with different features such as lattice dimension or surface roughness. Additionally, being all substrate materials polycrystalline, as soon as the polycrystalline diamond starts to grow, the lattice structure of the substrate is forgotten and the diamond structure and morphology are governed only by the choice of other working parameters such as pressure and temperature. This fact is strengthened by the experimental observation that, changing the (p,T) couple, the diamond structure and morphology are different [97].

5.4.2 Dynamics of the early stages of growth

Regarding the first substrates used in this work, i.e. Si and Mo, according to morphological and structural characterizations, four main steps of diamond growth with the DC-μP can be identified: i) formation of a carbide compound, ii) spontaneous growth of a crystalline graphite layer, iii) formation of the first diamond agglomerates, and iv) agglomerates growth and coalescence in a compact film. In our observations, the first step regarding carbide formation is experimentally confirmed only for Mo substrate through XRD measurements, whereas no carbide compound is detected on Si, even if evidence of silicon carbide formation during PECVD of diamond in the same range of temperature used in this work is reported [52, 110]. In the explored conditions, the Gibbs Free Energy of formation of molybdenum carbide is more negative than the Gibbs Free Energy of formation of silicon carbide [134]. Hence, the chemical reaction between Mo and C is more favored. In addition, the C diffusivity on the surface of Mo is higher than in the case of Si [150]. In fact, once formed, the carbide layer is reported to have different thickness: around hundreds of angstroms or few nanometers for silicon carbide against few micrometers for molybdenum carbide [51, 61, 132]. All these observations suggest that, in our case, silicon carbide layer may be too thin and thus undetectable by both Raman spectroscopy and XRD, and this is validated by the fact that the carbide compound represents the chemical way for diamond to remain bonded to the substrate.

SEM images of samples on Si and Mo substrate materials in the early first stages show the formation of several agglomerates; visible Raman spectra analysis reveals the presence of a crystalline graphite layer, with clearly visible D and G peaks, and from UV Raman measurements it is possible to observe the non-dispersive behavior of these peaks, thus confirming the mainly crystalline nature of the sp^2 carbon (i.e. graphite) deposited in the first minutes. As the coalescence of diamond agglomerates is completed (i.e. from 30 minutes on Mo and from 1 hour on Si, see fig. 5.2 and fig. 5.3), the Raman graphite signal is covered by the stronger signal arising from the deposited diamond: taking into account also the limited depth sensitivity of Raman, this observation allows to localize the graphitic signal as coming mainly under the diamond film. By looking closely to SEM images of diamond deposited on the other substrates (see fig. 5.7), and coupling these pictures with results of visible Raman spectroscopy (see fig. 5.9), the same considerations as in the case of Mo and Si can be drawn. Thus, we attribute to the graphite layer the determining role of preferential site for diamond nucleation. Indeed, in the synthesis of diamond coatings on non-diamond substrates, the criteria that must be satisfied for spontaneous nucleation are i) carbon saturation of the substrate surface and ii) presence of high energy sites [51]. According to the nucleation model for diamond on graphite, diamond nuclei can grow preferentially on the prism planes of graphite, with kinetically preferential nucleation at the emerging graphite stacking faults [57]. This nucleation mechanism is proposed to be the dominant channel for spontaneous nucleation of diamond crystals in the absence of pre-existing diamond seeds [57]. Other works in literature confirm this model [43, 56, 60, 80], and show how the carbide interlayer can act as a temporary but critical host on which the carbon can accumulate until clusters of the appropriate size and structure required for diamond nucleation develop [61]. Once the graphitic layer is formed, the chemical steps leading to diamond deposition are governed by the role of the super-equilibrium atomic hydrogen in the plasma phase, and whose fundamental task has already been extensively explained in chapter 2 [97]. All these observations, together with the fact that the diamond signal in Raman spectra does not appear at the beginning of the synthesis, are coherent with the assumption that, in our case, the nucleation of diamond is occurring on the substrate materials and not in the plasma phase, even if experimental evidence of this process are reported in literature with the same deposition technique, but in different experimental conditions (i.e. pressure, temperature and feed gases) [69]. In our observations, there is a different growth kinetics between the used substrates. Since the diamond nucleation occurs when the carbon concentration on the substrate reaches its saturation value, it is reasonable to suppose that the formation of the graphite layer occurs with different timing.

To conclude, the fact that, in process conditions favoring diamond growth, a spontaneous layer of graphite is deposited on every substrate in the early stages of growth, and that acts as a trigger for diamond nucleation, is not a obvious issue. Additionally, the deposition of diamond and graphite happens simultaneously during diamond growth, but for thermodynamic stability the graphite etching is faster: the fact that only graphite is detected in the early stages confirms that this is the part of the whole diamond deposition process between the end of the nucleation and the start of the growth, and thus the chosen deposition times are suitable for the aim of the work. Finally, by looking closely to the graphitic systems found, their nature is different from substrate to substrate (see figs. 5.4 and 5.9). By a detailed analysis, some information can be deduced, and also considerations about how this graphitic system tends to influence diamond features. The analysis of these graphitic systems is extensively reported in the following sections.

5.4.3 Analysis of the early stages graphite

To acquire information about the graphitic systems found on all substrates, the corresponding Raman spectra were all fitted following a precise procedure: Lorentzian functions were used for all the peaks, and values about position and FWHM are reported in tab. 5.1, whereas relative intensities of peaks (calculated using areas under the peak) are all reported in tab. 5.2, together with a proposed classification of the graphitic systems. From data reported in tab 5.1, analyzing G and D peaks, information about the quality of the graphitic layers can be inferred. A general observation regards the position of the G peak, for all cases slightly

Substrates	**Pos G** $\mathbf{cm^{-1}}$	**FWHM G** $\mathbf{cm^{-1}}$	**Pos D** $\mathbf{cm^{-1}}$	**FWHM D** $\mathbf{cm^{-1}}$	**Pos 2D** $\mathbf{cm^{-1}}$	**FWHM 2D** $\mathbf{cm^{-1}}$
Mo	1588.5	28.6	1372.2	38.4	2745.3	56
Si	1595.3	22.4	1368.4	61.6	2718.2	56.7
W	1586.6	21.2	1372.1	28.5	2749.4	51.9
Rh	1585.6	29.5	1366.4	35.5	2739.9	57.5
Fe	1586.1	15.8	1374.5	35.1	2725.3 2765.5	52.3 34.7
Ni	1587.5	18.3	0	0	2730.7 2767.5	56.7 37.7

Table 5.1: *FWHM and position of the D, G and 2D peaks as derived from the fitting of visible Raman spectra of diamond grown for 5 minutes and reported in figs. 5.4 and 5.9.*

Substrates	$\mathbf{I}_D/\mathbf{I}_G$	$\mathbf{I}_{2D}/\mathbf{I}_G$	**Summary**
Mo	0.64	1.38	MLG
Si	0.58	0.74	TG
W	0.41	1.96	FLG
Rh	0.46	1.45	MLG
Fe	0.24	-	G
Ni	0	-	G

Table 5.2: *$I/_D/I_G$ and I_{2D}/I_G ratios as calculated from the areas of peaks as derived from the fitting of visible Raman spectra of figs. 5.4 and 5.9. For the case of Fe and Ni, where the 2D peak clearly present two contributions, the I_{2D}/I_G ratio is not meaningful. In the last column, a summary of the type of graphitic systems found on the substrates is reported (see Appendix A), where MLG, FLG, TG and G stand for multilayer graphene, few layer graphene, turbostratic graphite and graphite respectively.*

higher than the expected 1582 cm^{-1}, probably due to interaction with the substrate (stress, induced doping). Further the G width is slightly broadened indicating the presence of some amount of disorder, except on Fe and Ni substrates, where values close to crystalline graphite are found. The intensity ratio $\mathrm{I}_D/\mathrm{I}_G$, largely used in the carbon community to evaluate the defectivity of the layers, is reported in fig. 5.10 for all substrates, and generally confirms this trend, being very small or zero for Fe and Ni substrates. Additionally, for these two substrates we observe a double 2D peak, as expected for Bernal stacked graphite. In the end, it appears that on substrates such as Ni and Fe the grown graphitic material shows a better crystallinity with respect to the other investigated substrates, all belonging to the "carburizing family" (i.e. Mo, Si and W). For them the previous observation of misoriented stacking of graphitic layers can be completed by the quantitative analysis of the single Lorentzian 2D peak, namely of its width and intensity ratio with the G peak, see fig. 5.11. From the indication in the literature concerning these two parameters [136, 142], we may conclude that on W a FLG is formed, on Mo and Rh a MLG, while several layers are present on Si. Particularly, for the case of W, the highest value of the I_{2D}/I_G ratio is found among all the investigated materials, and this value is typical of the monolayer graphene; however, we exclude that this is the situation, since the FWHM value of the 2D peak of the typical monolayer graphene is definitely lower than the FWHM value of the 2D peak found in the graphitic system deposited on W (see Appendix A). Moreover, on Rh, which is the only substrate with a columnar nanostructure, the multilayer system appears to be more disordered than in the case of Mo, and this can be linked to the peculiar structure of the substrate. For Ni and Fe a double 2D peak reveals a Bernal stacking order, whereas a single-Lorentzian 2D peak for all the other substrates suggests a misoriented stacking of graphitic layers [136].

5.4.4 Correlation between the first stages graphite and the NCD

As for the case of the graphitic systems found in the early stages of growth, also the NCD grown has features different from sample to sample. Indeed, being the graphite layer different from substrate to substrate and also the responsible for diamond nucleation, it is reasonable to suppose that different graphitic features can imply different diamond features. For this reason, all Raman spectra of NCD were fitted, in order to acquire information about the diamond peak (position and FWHM) and evaluate qualitatively the $\mathrm{sp}^3/\mathrm{sp}^2$ content. Many papers can be found in literature reporting different procedures of spectra deconvolution, using mainly Lorentzian functions for crystalline components, a combination of Gaussian curves for amorphous and disordered sp^2 peaks and, in some cases, a unique, irregular-shaped Breit-Wigner-Fano function for the merging

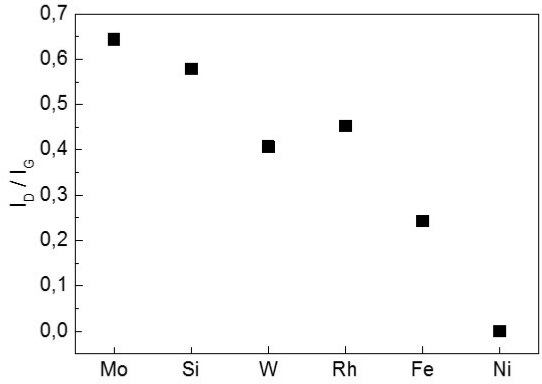

Figure 5.10: *I_D/I_G values derived from the fit of spectra of figs. 5.4 and 5.9 and represented as a function of the substrate.*

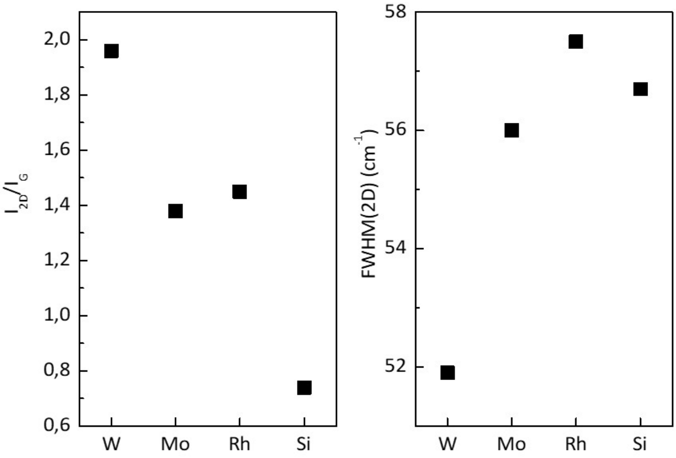

Figure 5.11: *I_{2D}/I_G ratio and FWHM values of the 2D peak represented as a function of the substrate, and only for single Lorentzian 2D peak, which explains the absence of Fe and Ni. A different sequence for substrates is adopted with respect to fig. 5.10.*

contributions of the ν_3 and the G peaks [110, 126, 151]. For this work, a single, Lorentzian function is chosen for the diamond peak, whereas four gaussian functions are used to fit the whole amorphous-carbon components (thus separating the ν_3 and G contributions). As already stated, diamond grown for 30 minutes on all substrates was chosen as a representative case, since at this time on almost all substrates a nearly continuous film was formed (with the only exception of Fe, as already showed), and spectra taken with 457 nm were used. An example of Raman spectrum deconvolution is reported in fig. 5.12. Three parameters were used, to evaluate main features of NCD: the position and the FWHM of the diamond peak, and the sp^3/sp^2 content. Position and FWHM are meaningful because directly linked to the presence of stress states in the samples and to the crystalline quality of the grain size: particularly, the lower the FWHM is, the better the crystallinity is, whereas the shift in the d peak refers to the presence of stress. For sp^3/sp^2 relative quantities, a dedicated parameter was used. Indeed, as explained in Appendix A, due to the difference in Raman cross-section between sp^2 and sp^3 a quantitative information about diamond/non-diamond ratio in the samples can not be directly related to Raman peaks intensities ratio. For this reason, a coefficient was used, which is defined as follow:

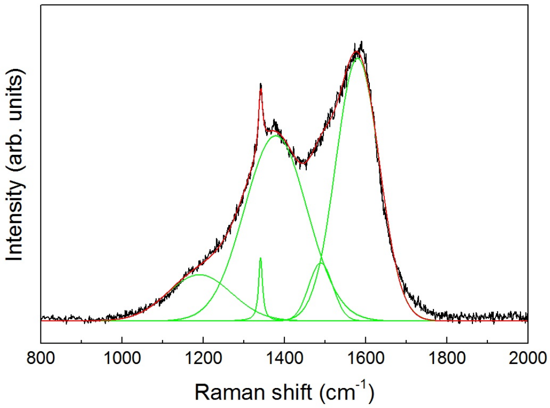

Figure 5.12: *An example of Raman spectrum deconvolution, where a Lorentzian function were used for the d peak whereas four gaussian functions were used for the other non-diamond contributions.*

$$f = 100\frac{75I_{diamond}}{75I_{diamond} + I_{non-diamond}}$$

where $I_{diamond}$ and $I_{non-diamond}$ are respectively the areas under the diamond and the non-diamond peaks. This ratio is weighted taking into account the difference in cross-section between the diamond and the amorphous carbon, and it is defined only for visible Raman measurements f [152, 153].

Values of d peak position and FWHM as a function of substrate and values of f coefficient as a function of the defectivity of the first stages graphite (i.e. I_D/I_G ratio) are reported in fig. 5.13. A slight shift in the diamond peak position with respect to its theoretical position is measured but also expected, since the substrate-diamond lattice mismatch induces a certain stress state in the film. Concerning the FWHM values, they are likely to be in the range of values of diamond with small grain sizes (i.e. nanocrystalline). Being the f coefficient linked to the sp^3/sp^2 content, a low value of this coefficient is symptomatic of diamond with a smaller grain size, being the sp^2 located mainly at the grain boundaries. Considering this, some observations can be derived. On Rh coated silicon, the d peak position is centered in its theoretical value, and thus a relaxation of the interface stresses can be deduced. It is worth noticing that, oh Rh, also the less stressed graphitic system was found (as deduced from the G peak position). At the same time, the high value of FWHM means a diamond with a very small grain size and low crystallinity, which is in accordance with the low value of the f coefficient. On Fe and Ni, that show similar values of all diamond features, the f factor is the higher among the analyzed substrates: this can be correlated to graphite properties that, with respect to other substrates, promote the growth of diamond films with a higher content of sp^3 phase with respect to sp^2 [56–58]. On Mo, Si and W instead, where a multilayer system is found in the early stages of

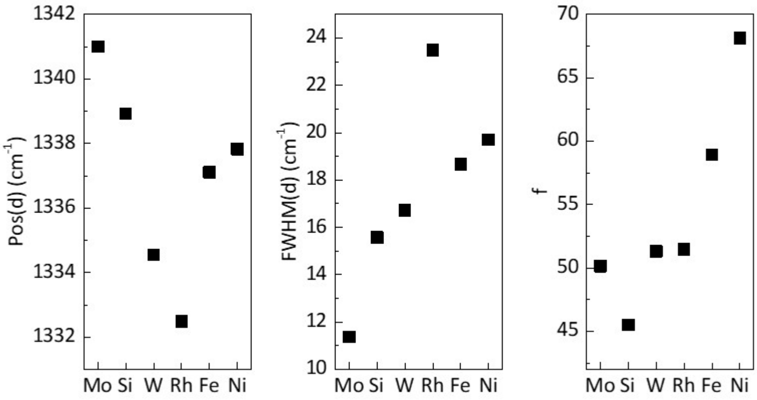

Figure 5.13: *Position and FWHM values of diamond peak as a function of the substrate material, for NCD deposited for 30 minutes. Values were derived from the visible Raman spectra fit. Also, the f coefficient values depending on the substrate material is reported.*

growth, diamond still grow but with a lower grain size (i.e. low sp^3/sp^2 content); at the same time, the crystallinity of the grain is slightly better (see FWHM values) than on the other substrates. The fact that a lower grain size is found on these substrates can be related to their high nucleation density tendency, that results in packed film formation [154]. In summary, the increasing in sp^3/sp^2 content (and thus in the grain dimension) we observed is linked to the crystallinity of the early stages graphite, and this is clearly shown in fig. 5.14, where the dependence of the f factor of NCD on the I_D/I_G ratio of graphite is reported.

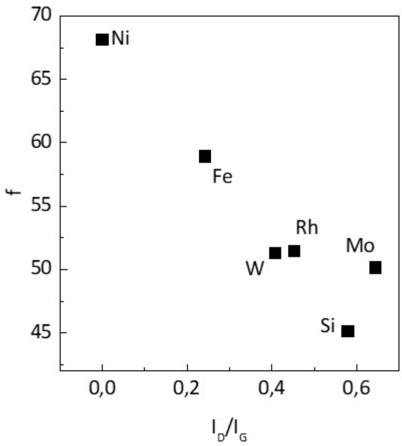

Figure 5.14: *f coefficient values (and thus a qualitative sp^3/sp^2 content evaluation) of diamond deposited for 30 minutes as a function of the graphite cristallinity.*

5.4.5 NCD features

Also, since Mo and Si were characterized step by step for each deposition time (see fig. 5.4), values of the f coefficient were used for these samples to evaluate the evolution of the sp^3/sp^2 content with the growth time, as representative for NCD growth with the DC-μP. These means that only visible spectra where the d peak is clearly visible were fitted, that is, in our case, for samples grown at 10 minutes, 15 minutes and 30 minutes on Mo and at 30 minutes, 1 hour and 2 hours on Si. The fitting procedure used is the same of the previous section.

Values of the f coefficient are reported in tab. 5.3, as a function of the deposition time.

This coefficient shows the same behavior for samples deposited on Mo and on Si substrate: the f value increases until coalescence of diamond

Dep. time [min]	10	15	30
f(Mo)	31.18	53.07	49.99
Dep. time [min]	30	60	120
f(Si)	45.51	50.24	47.82

Table 5.3: *Values of the coefficient f for diamond deposited on Mo and Si.*

agglomerates (happening at 15 minutes on Mo and 1 hour on Si, see figs. 5.2 and 5.3), then slightly decreases. This trend can be assigned to the morphology evolution. Indeed, taking into account the definition of the f coefficient, and assuming that: i) the agglomerates shape can be assimilated to a sphere, ii) the amorphous component in the samples is mainly present at the grain boundaries and thus restricted to the surface of the sphere, iii) the sp^3 crystalline phase is instead present in the bulk of the sphere, the increasing in the f coefficient for both samples is a consequence of the increased dimension of diamond agglomerates. As the diamond agglomerates blend together, the f coefficient follows the crystalline domain size reduction (and thus an increment in the grain boundaries density) with a slight decrease. The magnitude of f is a further indication that the growth of the deposit evolves towards a nanocrystalline morphology, as deduced from the analysis of Raman spectra.

5.5 Production of NCD films with the DC-μP

Even if extremely flexible and versatile with respect to process parameters and carbon allotropes deposition, cheap and user-friendly, the DC-μP set-up presents some limitations if thought as a deposition technique for continuous and large area films production.

First of all, the small volume of the plasma plume limits the dimension of surface area of deposited samples. Two possible solutions can be implemented in order to obtain a larger area covering. The first one regards the possibility of increasing the cathode diameter. However, cathode diameter can not be arbitrarily chosen: its dimension is linked to the chamber pressure, and their product must lay in a range of values such that the micro-hollow effect is achieved (as explain in chapter 2). Additionally, when changing pressure, also temperature must change in accordance to 2.3, verifying the (T,p) couple still lays in the diamond stability region and where the precursors favor the kinetics (see fig. 4.3). A second approach is the implementation of a dynamic deposition. Indeed, the translating apparatus equipping the DC-μP set-up can be properly used in such a way that during the deposition the cathode is kept in movement with respect to the substrate. Since the deposition spot shows a gaussian-like profile, the movement would allow to sum the tails of the gaussian curves in order to obtain a flat profile. Even if easy to be implemented and not too demanding, both these solutions require several experiments in order to optimize the new deposition conditions and, for the second solution, the translating velocity.

Another limitation of this set-up regards the direct-current excitation source. This implies that only conductive substrates can be used for deposition, as already explained. Additionally, being diamond an insulating material, it is reasonable to suppose that, over a certain thickness, the deposition stops and is not possible to proceed. However, the estimation of this "limit thickness" is definitively not easy, since a NCD with so much sp^2 content has for sure a different (and lower) resistivity with respect to the single-crystal one, and the sp^2 content directly influences it. A possible solution to overcome this problem is the implementation of a radio-frequency excitation source: it would allow to obtain more stable depositions over a prolonged time, and also on non-conductive substrates. However, such kind of device set-up is expensive and requires a dedicated optimization work in order to find appropriate process conditions. A less expensive and easily employable solution would rely in putting a "small net" made of conductive material between the cathode and the substrate, and extremely closed to the substrate: this net would be able to act as a new anode for the plasma. In such a way, the nucleation of diamond in the plasma phase could be explored and, once formed, diamond crystals could pass through the net and deposit themselves on the substrate that, at this point, could be made also of a non-conductive material.

All these possible upgrades and investigations are beyond the scope of this thesis project, where the main goal is to perform dedicated experiments to investigate the early stages of diamond growth on several materials using the actual deposition apparatus. However, some work have been devoted to the possibility of depositing thicknesses interesting for industrial-relevant applications with the actual set-up, in order to investigate the performance of this device, never used for this kind of work. Exploiting the extreme smoothness and flatness of Si substrate, thickness and deposition area of samples grown for 90 minutes, 3 hours, 5 hours and 7 hours (in the same deposition conditions presented in chapter 4) were measured, and values can be found in tab. 5.4. As an example, SEM cross-section and top view of the sample deposited for 90 minutes are shown in fig. 5.15. The deposit shows a circular shape (see inset c) of fig. 5.15), and a Gaussian-like profile (see inset a) of fig. 5.15), with the density of agglomerates decreasing from the center to the periphery region of the deposition. Nevertheless, it is worth noticing that, for higher thickness, a higher covering is achieved, even if the plasma plume dimension is fixed at 178 μm. From cross-section view (see inset b) of fig. 5.15), we clearly appreciate a columnar growth with diamond agglomerates starting coalescence after a thickness of few μm. From data reported in tab. 5.4, we note that the thickness is linear

Growth time	**90 min**	**3 h**	**5 h**	**7 h**
Area [mm^2]	≈ 0.19	≈ 0.22	≈ 0.28	≈ 0.28
Thickness [μm]	20	40	90	120

Table 5.4: *Areas and thicknesses values of diamond grown on Si with increasing deposition time.*

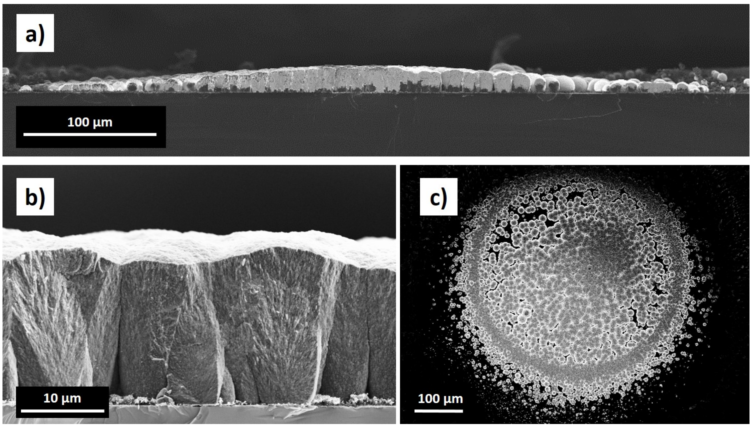

Figure 5.15: *Diamond grown on Si for 90 minutes: a) a cross-section view, b) a magnification of the cross-section taken in the center of the deposit and c) a top view of the deposition.*

with deposition time, with a growth rate of about 16 μm/h (R^2 = 0.9941 if fitted with a linear function), whereas the area of the deposition spot seems to already reach a saturation trend.

Part III

Diamond detectors performance: an investigation of electrodes fabrication and irradiation effects

Chapter 6

Fabrication of graphitic contacts on PCD substrates

6.1 Introduction

As already introduced in chapter 1, electrodes fabrication is a delicate and important aspect of the whole diamond device production, since the detector performance depends also upon the efficient collection of charge carriers. Conductive metal-based contacts are usually deposited as thin films on diamond front and rear surfaces via different methods (e.g. evaporation, sputtering, metalization, etc.) showing good charge collection performance. However, an interfacial layer to guarantee a good adhesion between diamond and the electrodes is always deposited, and can act as a dead layer significantly affecting the detection performance [34]. For these reasons, in the last years carbon-based electrodes have been evaluated as a possible alternative to common metal-based contacts, exploiting the conductive properties of graphite. Either planar "sandwich" graphitic electrodes deposited on opposite diamond surfaces or "3-D" graphitic electrodes written in the diamond bulk by means of laser are possible technological solutions, each one having advantages and disadvantages. For this reason, in this doctoral thesis project, an investigative work was performed about deposition of carbon-based films on PCD, subsequently graphitized with annealing procedures. Particularly, in this work carbon films were deposited by means of pulsed-laser deposition (PLD), that is a versatile technique extremely suitable for the deposition of various materials on different substrates, also controlling parameters such as stoichiometry and morphology of the deposited film. However, its exploitation for the deposition of carbon-based contacts on PCD substrates represents an innovative approach to this issue. Additionally, two different solutions for the annealing procedure were studied, based on thermal annealing and laser annealing processes, in order to graphitize the thin carbon film. This chapter is organized as follow: the methodology adopted for carbon deposition, samples characterization and annealing treatments is presented in sec. 6.2, whereas main results are presented in sec. 6.3.

6.2 Methodology

6.2.1 Carbon films deposition

For investigating this topic, polycrystalline diamond samples bought from Element Six Ltd. were used as substrate materials. Since the idea was to start an investigative and conceptual study about deposition of graphitic contacts on diamond substrate, of course some issues have to be verified, e.g. the adhesion and the graphitic nature of the coating. For this reason, different kinds of substrate were bought, i.e. Thermal Grade, Optical Grade and Detector Grade polycrystalline diamond. However, being the study preliminary, first depositions were made on the cheaper substrates, i.e. the Thermal Grade ones.

For the deposition of graphitic contacts, PLD technique was used. PLD is a physical vapor deposition technique in which the target material is brought into vapor phase by means of laser ablation (i.e. a physical process). In such a way, the ablated material (atoms, molecules, ions etc.) can expand in the vacuum chamber, assuming a plume shape, and be collected on a proper substrate. The plume expansion can occur either in vacuum or in the presence of a background gas, that in turn can be either chemically inert (e.g. helium, argon) or reactive (e.g. oxygen, nitrogen). The laser used has a ns pulse duration: in such regime, electron-lattice relaxation is so fast that allows to describe the system with a single temperature distribution. If the laser heating is sufficient to achieve an increase in the temperature, the laser ablation happens. It is therefore possible to define a threshold areal energy density (i.e. a fluence) above which ablation correctly occurs, depending on target properties and laser parameters. During plume expansion, the presence of background gases can induce collisions between plume species and atoms from the gas. In this way, plume species lose their energy by slow down. If the background gas is chemically reactive, chemical reaction with the ablated material are induced. Film morphology is strongly linked to plume confinement and collisional processes: indeed, at low pressure an atom-by-atom deposition is promoted, that leads to compact films formation, whereas at higher pressure the cluster growth is favored, leading to hierarchical and porous films.

In addition to the above mentioned ones, other process parameters can be controlled (e.g. laser wavelength, fluence, repetition rate, target-to-substrate distance, etc.), that make the PLD set-up an extremely

versatile and reliable technique for films deposition. Particularly, the deposition of carbon-based films with different sp^2/sp^3 content has already been proved [155–157], that justifies the use of this deposition technique for an investigative study about growth of carbon films for electrodes fabrication for diamond detector technology.
The PLD set-up used in this work is shown in fig. 6.1. It consists of a solid-state laser, optics to direct the laser beam to the target, a high vacuum chamber, a pumping system and a set of remote-controlled motors for the motion of either the target and the substrate. The laser source is a Q-Switched Nd:YAG laser, generating ns pulses at the fundamental wavelength $\lambda = 1064$ nm (IR). The maximum repetition rate is 10 Hz and through non-linear crystals it is possible to frequency-double and frequency-quadruple the fundamental wavelength, obtaining pulse wavelengths of 532 nm and 266 nm. The high vacuum chamber is a stainless steel cylinder equipped with a pumping system made up of a primary rotary scroll pump (working in a viscous flow regime allowing to reach a pressure of 10 Pa) and a TurboMolecular Pump (working in molecular flow conditions till a pressure pf 10^{-4} Pa). Manipulators are used in order to translate the target and the substrate both in horizontal and vertical directions and to rotate them around their axis. The motion of the target is such that a uniform ablation is achieved, whereas the substrate motion is calibrated in order to achieve film planarity over areas

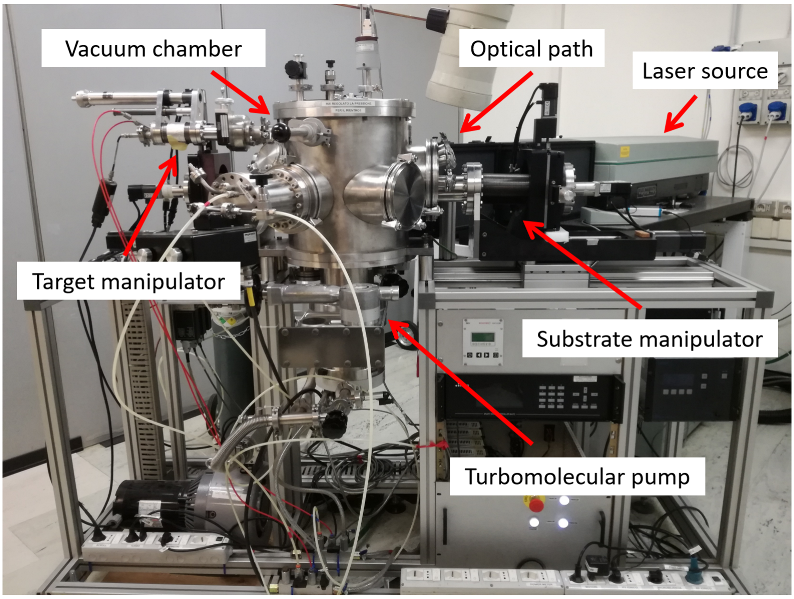

Figure 6.1: *A picture of the PLD equipment used for carbon films deposition. All main parts of the experimental set-up are highlighted.*

of several cm^2 (having the static deposition a gaussian profile).
In the present work, process parameters were set accordingly to previous results about deposition of carbon-based films with the PLD [158]. Green laser was used to ablate the target (λ = 532 nm) with a target-to-substrate distance of 5 cm. Laser energy was set at 180 mJ and helium was used as background gas, with a chamber pressure of 10 Pa. Deposition time was set at 10 minutes.

6.2.2 Annealing treatments and characterization set-up

Being carbon films produced by means of PLD with the chosen process parameters strongly amorphous in structure, laser annealing and thermal annealing treatments were made on samples after the deposition, in order to graphitize the deposited carbon films. For the thermal annealing, the experimental set-up consists of a high vacuum chamber, a heater stage and a pumping system. Two thermal annealing procedures were studied. In the first one, sample was heated at 500 °C for 1 hour in vacuum (pressure around 10^{-3} Pa) with a temperature ramp of about 10 °C/min. In the second procedure, sample was heated at 850 °C for 1 hour keeping pressure at 10^{-4} Pa, with a temperature ramp of 10 °C/min. For the laser annealing, the same apparatus of PLD was used. Briefly, the laser was focused directly on the sample and a single shot with ns pulse duration was performed. Chamber pressure was maintained at 10 Pa with laser energy around 180 mJ (λ = 532 nm).
Either bare substrates and carbon films deposited by PLD were characterized by means of SEM and Raman spectroscopy. Particularly, for Raman spectroscopy, λ = 514.5 nm was used. For the description of the characterization tools, refer to chapter 4.

6.3 Main results

6.3.1 PCD substrates characterization

Three kinds of PCD substrates were bought from Element Six Ltd., i.e. Thermal Grade, Optical Grade and Detector Grade polycrystalline diamond. In order to qualify these materials and acquire information about their chemical impurities and crystalline quality, Raman and PL spectra of these substrates were measured, and can be found in fig. 6.2.
Analyzing the Raman contribution (i.e. the part of the spectrum at lower wavelengths), all substrates show a very sharp Raman line of diamond with position and FWHM close to those of natural diamond, i.e. 1332 cm^{-1} and around 4 cm^{-1} respectively (thus being so sharp that in the global spectrum appears as a line). A magnification of the diamond Raman peak for Thermal Grade substrate is shown in the inset d) of fig. 6.2, but the same was found on all the other substrates. This allows to infer that these

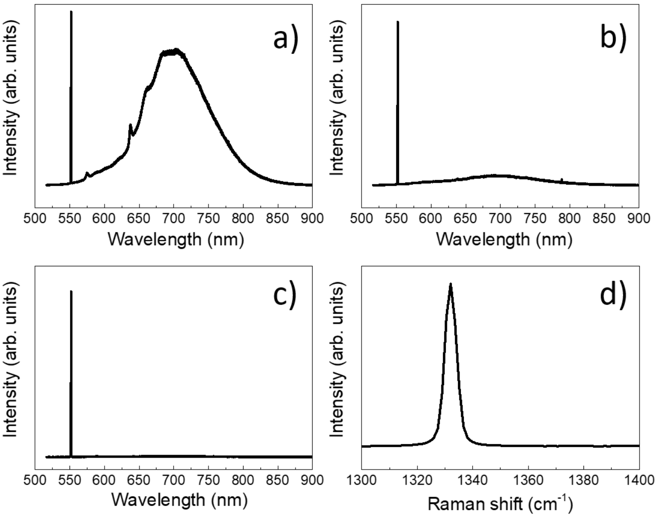

Figure 6.2: *Raman and PL spectra of the PCD substrates bought from Element Six Ltd.: a) Thermal Grade polycrystalline diamond, b) Optical Grade polycrystalline diamond, c) Detector Grade polycrystalline diamond and d) a magnification of the Raman line of the Thermal Grade diamond.*

PCD substrates surely have a crystalline structure with very good quality. The PL contribution is instead completely different from substrate to substrate. Particularly, for the case of the Thermal Grade substrate (inset a) of fig. 6.2) a strong PL background is found, extended even in the Raman scattering region of the spectrum, with peaks that can be assigned to nitrogen vacancy defect centers, either negatively charged or neutral (found at 575 and 640 nm respectively), and accompanied by the typical broad bands always found in such kind of PL transition. For the case of Optical Grade substrate, a weak PL contribution is found, with a broad band centered at around 700 nm: however, it represents a negligible contribution. Finally, for the case of Detector Grade substrate, the PL background is completely absent, revealing this substrate to have less chemical impurities than the Thermal Grade and Optical Grade.

6.3.2 Carbon films deposited on PCD substrates

Carbon-based films were deposited by means of PLD on either Si and Thermal Grade polycrystalline diamond substrates. All samples were characterized before and after deposition by means of Raman and PL spectroscopy and SEM. SEM images of a top view of the Thermal Grade polycrystalline diamond substrate and of the carbon film are shown in fig. 6.3. Since the growth rate of films deposited with PLD is dependent only upon process parameters such as pressure, laser energy, target-to-substrate distance and background gas atmosphere, the same experiment was run also on Si substrate, in order to exploit its smoothness and analyze the sample thickness in cross-section, as shown in fig. 6.4.

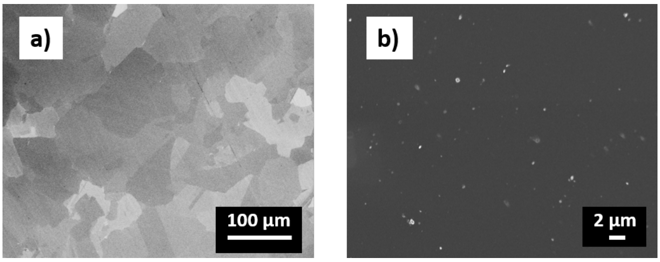

Figure 6.3: *SEM images of a) Thermal Grade polycrystalline diamond substrate bought from Element Six and b) carbon film deposited with PLD on the Thermal Grade diamond substrate.*

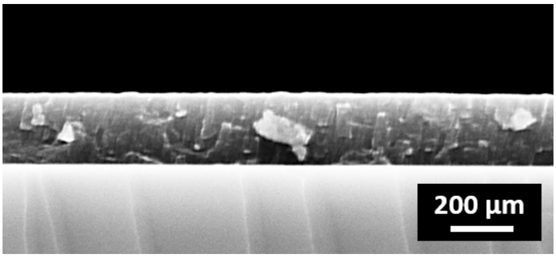

Figure 6.4: *SEM cross section of carbon film deposited on Si substrate for 10 minutes with PLD. A compact morphology with homogeneity in thickness (≈ 240 nm) is found.*

As it is possible to see, a compact carbon film was deposited, with a uniform thickness of about 240 nm after 10 minutes of deposition. Raman spectra of carbon-based films deposited on PCD substrate is shown in fig. 6.5. In this spectrum, the typical features of amorphous carbon are shown, with a broad G band merged with the D peak. Also, a contribution at higher frequency is found (around 2000 cm^{-1}), linked to the presence of some disordered metastable sp carbon, that rearranges and disappears after a certain time that sample is exposed to air.
To "graphitize" this film, a first thermal annealing procedure was made, heating sample at 500 °C for 1 hour in vacuum, as described in chapter 6. Carbon films deposited on both Si and polycrystalline diamond were annealed. Raman spectrum of the thermal annealed carbon film deposited on polycrystalline diamond is shown in fig. 6.6. The same spectrum was found for the thermal annealed carbon film deposited on Si. From the

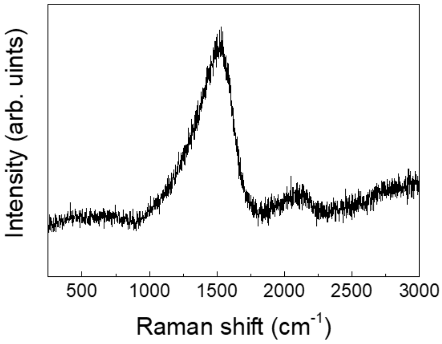

Figure 6.5: *Visible (λ = 514 nm) Raman spectrum of carbon film as deposited on PCD substrate.*

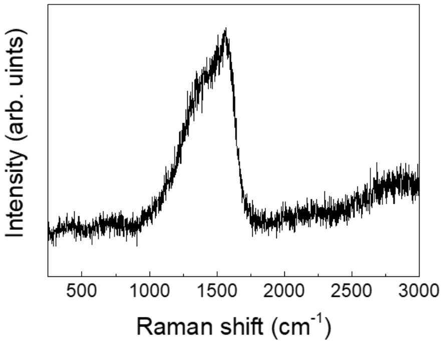

Figure 6.6: *Visible (λ = 514 nm) Raman spectrum of carbon film deposited on PCD substrate after 1 hour of thermal annealing @ 500* °C.

analysis of Raman spectrum shape, it is possible to infer that the D and G contributions are starting splitting in two peaks, revealing an evolution towards polycrystalline graphite. However, still a strong degree of amorphization exists in this sample, meaning that the thermal procedure was not sufficient to completely graphitize it. Additionally, this thermal annealing led to film delamination on both Si and PCD. For this reason, two different strategies were tested, in order to find the best solution. In the first case, a film with reduced thickness (around 100 nm) was deposited only on Si, keeping fixed all the other process parameters, and then it was subsequently annealed at 850 °C for 1 hour in vacuum. In the second case, film thickness was maintained, and laser annealing was performed on carbon films deposited either on Si and on PCD. In both cases, no delamination occurred after the annealing treatments. Raman spectra of carbon film deposited on polycrystalline diamond annealed with laser and of carbon film deposited on Si thermally annealed at 850 °C are shown in fig. 6.7. As it is possible to see, in both cases the broad, merged band starts splitting separating the two contributions of D and G, getting closer to the typical spectrum of polycrystalline graphite. This is more evident for the laser annealed case than for the thermal annealed sample, where the two peaks are still quite merged together. Additionally, this time no delamination occurred on all substrates. However, for the laser annealing case, the annealing occurred only on an superficial area with the dimension of the laser spot (around few mm^2).

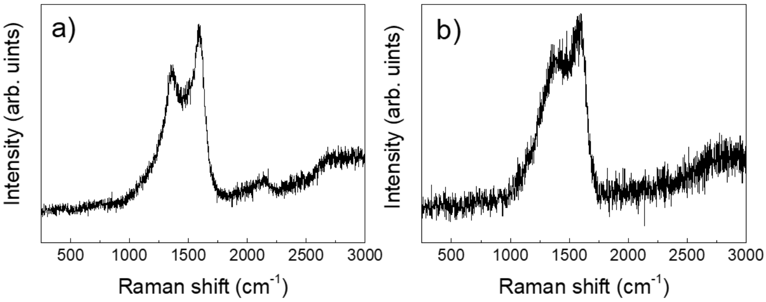

Figure 6.7: *Visible (λ = 514 nm) Raman spectra of a) carbon film deposited on PCD substrate after laser annealing and b) deposited on Si after thermal annealing at 850* °C *for 1 hour.*

To extrapolate information about exact positions of peaks, a fitting procedure is necessary, as defined in [127]. Several fitting procedures are accepted in literature, where Lorentzian curves are used for crystals, arising from finite lifetime broadening, and also accepted for disordered graphite, and Gaussian line shapes are employed for random distribution of phonon lifetimes in disordered materials. In amorphous carbon systems, as an alternative to the Gaussian curve, the Breight-Wigner-Fano (BWF) line can be used, having an asymmetric line shape suitable to describe the coupling of discrete modes to continuum. For these reasons, in our case a BFW function is used for the G peak, and a Lorentzian function for the D peak. Also, a Gaussian function was used for the sp contribution, where present. However, from as obtained results, still some calculations are essential, since the BWF function overestimates the G peak position. The actual G peak position x is indeed given by:

$$x = x_0 + \frac{w}{Q} \tag{6.1}$$

where x_0 represents the BWF peak position as derived from the fitting procedure, w the BWF FWHM, and the Q factor is the asymmetric

parameter taking into account the shape of the BWF function. Additionally, as in the case of graphitic system, the I_D/I_G ratio brings information about the amount of disorder, and can be calculated using the peak intensities.
Results from Raman spectra fitting and calculations (i.e. x_0, w, Q factor, x and I_D/I_G ratio) are reported in tab. 6.1.

Samples	**Substrate**	**x_0 cm^{-1}**	**w cm^{-1}**	**Q**	**x cm^{-1}**	**I_D/I_G**
As deposited	PCD	1547.9	95.2	-8.3	1536.4	0.49
Laser annealed	PCD	1597.5	58.4	-7.1	1589.3	0.7
Thermal @ 500 °C	PCD	1579.2	75.0	-5.6	1565.8	0.69
Thermal @ 850 °C	Si	1597.0	63.0	-6.4	1587.2	0.84

Table 6.1: *Raman features of the carbon film as derived from the fitting of Raman spectra of figs. 6.5, 6.6 and 6.7 and subsequent calculations.* x_0, *w*, *Q* *and* *x* *are the BWF parameters defined above.*

To describe the graphitization trajectory and classify these samples, the phenomenological three-stage model theorized by Ferrari can be used [125–127], as reported in fig. 6.8.

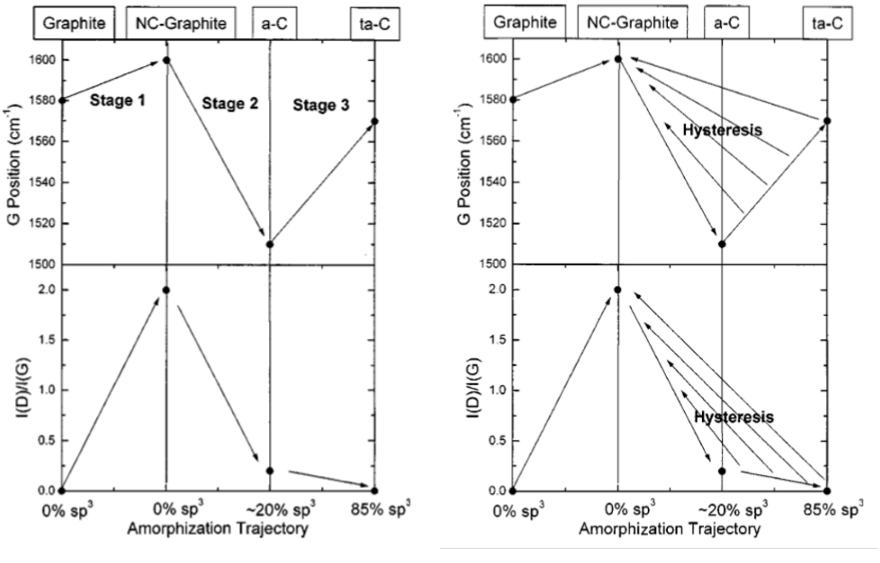

Figure 6.8: *Representation of the three stage model: particularly, the amorphization trajectory is reported on the left whereas the ordering trajectory is represented on the right, with the hysteresis cycle highlighted [127].*

Given a perfect, infinite sheet of graphite, as the introduction of a series of defects (e.g. bond-angle and bond-length disorder, hybridization) starts, the Raman spectrum is modified. Neglecting the role of hydrogen (not giving contribution to the D and G peaks), the Raman spectrum is thus dependent on i) clustering of sp^2 phase, ii) bond disorder, iii) presence of sp^2 chains and iv) sp^2/sp^3 ratio, and an *amorphization trajectory* (fig. 6.8, on the left) ranging from graphite to tetrahedral amorphous carbon (i.e. amorphous carbon with sp^3 content exceeding the 85%) can be defined, where G peak position and I_D/I_G ratio change values passing from graphite to nanocrystalline graphite (I stage), to amorphous carbon (II stage) and finally to tetrahedral amorphous carbon (III stage). This *amorphization trajectory* describes really well what happens when a relatively ordered carbon is disordered. Of course, also an *ordering trajectory* (fig. 6.8, on the right) can be defined, from tetrahedral amorphous carbon to graphite: this happens when an amorphous carbon sample is ordered through, for instance, a post-deposition annealing treatment, as in our case. Processes responsible for re-organization are mainly two: sp^3 sites converting into sp^2, and sp^2 clusters increasing in size and eventually ordering in rings. However, during an annealing treatment, these two processes are separated and happen at different temperatures: this causes an *hysteresis* in the cycle. The net effect of this *hysteresis* is the lack of an unique relation between sp^3 content, I_D/I_G ratio and G peak position (that, for the *amorphization trajectory*, on the contrary is present). Basing on the analysis of Raman spectra and of the parameters reported in tab. 6.1, some conclusions can be sketched:

- the as deposited carbon sample has G peak position and I_D/I_G ratio values typical of amorphous carbon composed by disordered sp^2 carbon rings, with a low content of sp^3 bonds (around 20 %);
- both thermal annealing treatments induce a non-complete graphitization of samples, resulting in films belonging to the II stage of the three-stage-model. i.e. between nanocrystalline graphite and amorphous carbon; additionally, the thermal treatment for 1 hour at 500 °C of the 240 nm thick carbon film led to delamination of sample on both Si and polycrystalline diamond, that on the contrary was not observed for the case of thermal treatment for 1 hour at 850 °C of the 100 nm thick film deposited on Si;
- the laser annealing treatment led to the best graphitization degree, since the post-annealed sample lies in the region identified by the I stage of the model. i.e. between graphite and nanocrystalline graphite; considerably, no delamination occurred after laser treatment.

Chapter 7

Single-crystal diamond under α and neutron irradiations: an investigative study

7.1 Introduction

As anticipated in chapter 1, the employment of SCD as radiation detector is appealing, because of the incredible performance of this material predicted by its electrical and structural properties. However, diamond detector technology is not free of drawbacks. Particularly, diamond behavior under irradiation is still under study, since for certain irradiation conditions some negative effects have been recorded, for instance the *polarization effect* resulting from α and fast neutron irradiations, that afflicts the charge collection efficiency. For these reasons, part of this doctoral thesis work was devoted to introduce a material characterization methodology to investigate modifications in the crystalline structure of diamond before and after irradiation, in order to find a correlation with the *polarization effect*. In section 7.2 a methodology for the investigation of irradiation effects by α and neutrons on SCD is presented, whereas in section 7.3 results coming from this approach are shown.

7.2 Methodology and characterization strategy

As already introduced in chapter 1, both α particles and fast neutrons are responsible for the *polarization effect* recorded in diamond detectors during irradiation, that in turn implies a decrease in the charge collection distance and efficiency. For this reason, since the goal of this work is to investigate this effect, two samples were chosen, to perform both α and fast neutrons irradiations. Regarding the Raman and PL measurements, three parameters were analyzed in the spectra: position of the diamond peak (symptomatic of stress states in the sample), FWHM of the diamond peak (linked to the cristallinity degree) and the presence of PL bands (sign of the presence of chemical impurities changing the crystalline structure of the sample).

Fast neutrons irradiation

A bare SCD substrate brought from Element Six Ltd (Detector Grade quality, here labeled as DIA) 5 x 5 x 0.5 mm was used to investigate fast neutrons irradiation. Exposure to neutron flux was performed at the ChipIR beamline of the ISIS spallation source, where neutron fluxes up to 10^6-10^7 cm^{-2} s^{-1}, with energy above 10 MeV and up to 800 MeV can be produced. Neutron at ISIS are produced on two Target Stations by a pulsed 800 MeV proton beam. Each pulse consists of two proton bunches about 320 ns apart, both having a pulse width of 100 ns. Protons impinge on a tungsten-tantalum target and produce high energy neutrons through spallation reactions [7]. In our experiment, DIA was irradiated for a time sufficient to obtain a neutron fluence of 4.5 x 10^{12} n cm^{-2}.

α irradiation

To investigate diamond behavior under α irradiation, a single-crystal diamond detector (here labeled as DET) was used. It is composed by a 5 x 5 x 0.5 mm SCD (again, bought from Element Six Ltd and of the same quality of DIA), fixed on a support, with metallic contacts of 1 x 1 mm size on front surface and with unknown geometry on rear surface, and encapsulated in a metallic casing. This sample has already been used in past experiments for neutron and α irradiations, showing a *polarization effect* arising during radiation exposure. In our experiment, irradiation of DET was performed by means of α particles by a laboratory Americium source ($E_\alpha \approx 5.5$ MeV) for 280 h. Particularly, Am source was positioned on the top of the detector with the metallic casing opened, but decentralized with respect to the upper central electrode, in such a way that a specific part of the detector (2 x 2 mm size) was exposed to direct and more intense irradiation, whereas the other part of the detector was not affected by the Am source exposure. A picture of DET together with a sketch of the single-crystal diamond with region irradiated highlighted is presented in fig. 7.1. By doing this, a fine and localized characterization of the diamond detector was possible, with focus on the directly irradiated region and on a region far from this point, to find potential differences linked to the irradiation exposure. The description of the characterization procedure is reported in the next paragraph.

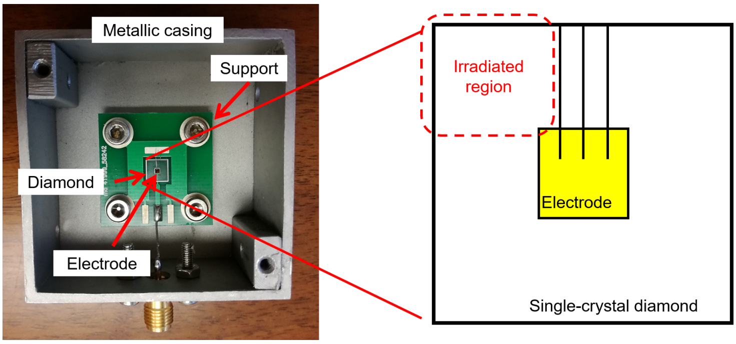

Figure 7.1: *A picture of the single-crystal diamond detector on the left, with a schematic sketch of the single-crystal diamond on the right, and region exposed to α source delimited by the red dashed box.*

Characterization of samples

Both samples were characterized by means of Raman and PL spectroscopy before and after irradiation. A precise procedure was set for the characterization methodology. Being Raman and PL spectroscopy a localized measurement (acquired with the same instrument described in chapter 4, with a laser spot micrometric), for both samples the characterization was performed on several points of the material, and the measurement was repeated for each point, to verify the repeatability of the measurement and the reliability of results. Particularly, for the sample DIA, being a substrate without contacts or encapsulation, characterization was possible on both front and rear surfaces. A sketch of the characterization procedure used is presented in fig. 7.2. Points of measurements are identified by capital letters. Regarding the sample DET,

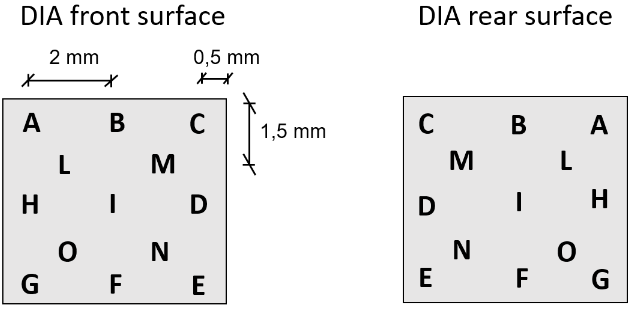

Figure 7.2: *Schematic representation of the front and rear surface of the single-crystal diamond exposed to neutron flux at ChipIR: the capital letters identify points of Raman and PL characterization.*

characterization was possible only on the front surface. However, by doing a selective exposure of DET to the Am source, it was possible to finely characterize the region directly exposed to radiation and a selected region far from the exposed one. A picture of characterization procedure is given in fig. 7.3, where a sketch of the SCD is shown with points of measurements highlighted by letters d-i. Red dashed box identifies the region subjected to direct irradiation, whereas green dashed box identifies the region far from the irradiated one. Raman and PL spectroscopy was performed with the same instrument presented in chapter 4, using green line ($\lambda = 514$ nm).

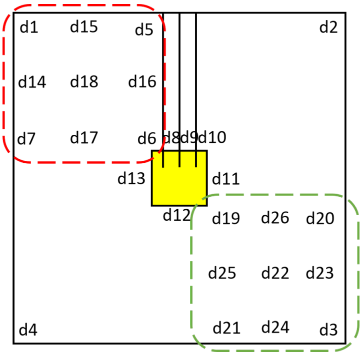

Figure 7.3: *A schematic sketch of the diamond detector: the d-i points identify where the characterization measurements were performed before and after irradiation. Particularly, points delimited by the red dashed box represent a region of the detector directly irradiated, whereas points delimited by the green dashed box represent a region far from the irradiated one.*

7.3 Experimental results

7.3.1 Fast neutrons irradiation

Sample DIA was characterized before and after irradiation with neutrons. An example of the Raman and PL spectra of DIA before the irradiation is shown in fig. 7.4, with a magnification on the Raman line of diamond in the inset. Being diamond an homogeneous material, the same spectrum was recorded in all the points of measurement.

As expected, the spectrum is typical of a SCD (see Appendix A), with the diamond first-order peak centered in its theoretical position (1332 cm^{-1}) and a FWHM close to that of natural diamond (in this case, around 4 cm^{-1}). No PL contribution is detected. All these features indicate a very good quality of the SCD substrate. Spectra recorded after the irradiation are reported in fig. 7.5 for both front and rear surface. Also, a

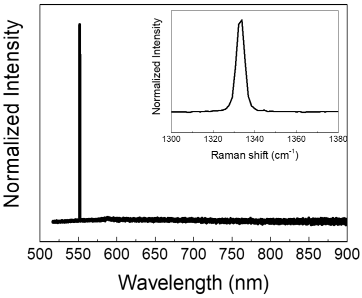

Figure 7.4: *Raman and PL spectrum of one of the point of measurements of the single-crystal diamond before the exposure to neutrons. Also, a magnification on the Raman line of diamond is shown in the inset. The same spectrum was found on all the other measurement points.*

magnification of the Raman first-order diamond peak is reported for each set of spectra.

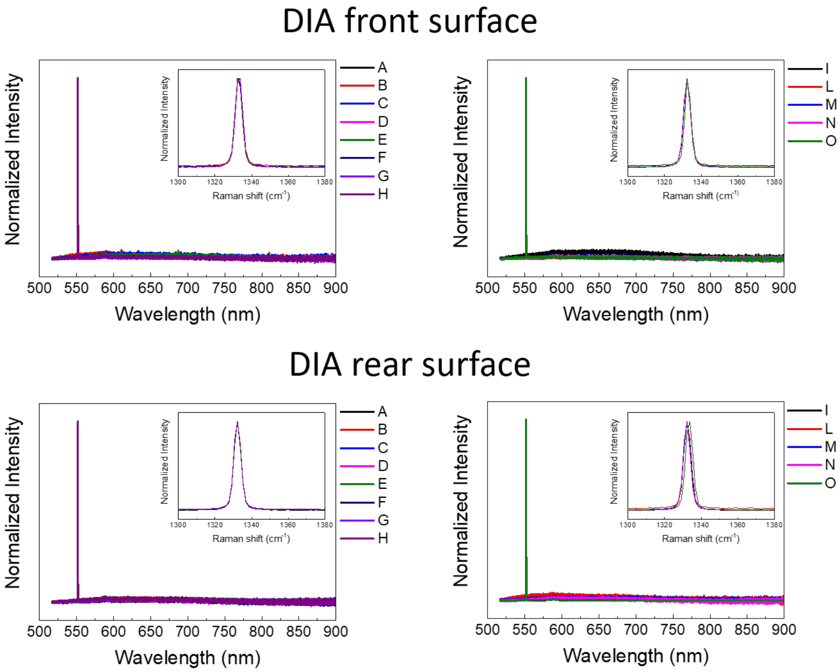

Figure 7.5: *Raman and PL spectra of the single-crystal diamond taken after the neutron irradiations, on both the front and rear surface of the sample, together with a magnification of the Raman peak of diamond.*

As can be seen, no actual variation occurs oh both position and FWHM values of the diamond peak, and also no PL increasing background was found. At the chosen neutron fluence, sample DIA seems not to be affected by irradiation. Basing on available literature data, this is not obvious. Since diamond-based detectors started to be considered as interesting candidates for high neutron fluxes, in the last years several experiments were programmed to test the diamond detectors performance and also its radiation hardness compared to that of common silicon-based detectors, and the arising of the *polarization effect*. Either experimental and theoretical works proved that, at high energy neutrons (above few hundreds of MeV), the radiation damage is dominated by the inelastic cross section, that is smaller for the case of carbon and additionally lighter nuclear fragments are created: this implies for diamond to be around an order of magnitude more radiation hard than silicon [159]. To meet the needs of available and cheap material with good detection capability, also silicon carbide detectors were tested, showing good performance overall over a wide range of temperature conditions and different radiation fields, but less capability in discriminating neutron and gamma contributions than diamond-based detectors was found, and additionally silicon carbide detectors showed to be subjected to a paralysable *polarization effect* [17, 160]. For these reasons, diamond detectors suggest to be the best candidates, and several experiments were made exposing single-crystal and polycrystalline diamond to high neutron fluxes with different energy spectra. In general, single-crystal diamond detectors start to show a decrease in the detection performance and the formation of defects in the crystalline structure from fast neutron fluences around 10^{14} - 10^{15} n cm^{-2}, with neutron energies varying from few keV [15], to few MeV [14, 161] and even above 14 MeV [162, 163]. In our experiment, the obtained fluence is around 2 - 3 orders of magnitude lower than the one commonly found in literature as a threshold value to induce tangible effects in the diamond crystalline structure and thus in its detection performance. However, it is worth noticing that a different neutron energy spectrum is found in the above examined works, and exposure to neutron fluxes and energy spectra such that of ISIS is an interesting topic of investigation, since the detector response function (and thus its interaction cross-section) at the considered neutron energies is still not known [34]. In general, the single-crystal diamond detector proved its capability to work in a neutron field such that produced at ISIS [28, 164–166] despite the *polarization effect*, and a stable response function of the detector was observed up to fluences of 10^{11} n cm^{-2} [167]. Our result allows to define a new threshold value for diamond detector to work in such kind of radiation fields, confirming the radiation hardness of this material.

7.3.2 α irradiation

The first and preliminary results about Raman and PL spectroscopy characterization of single-crystal diamond detector before and after α irradiation are presented in this dedicated section. As already anticipated, several spectroscopic analysis were performed before and after α irradiation on the same points on the detector, with particular focus on two regions: one directly exposed to the Am source, and the other one far from it.
In fig. 7.6 a schematic sketch of the directly irradiated region is shown on the left (the red dashed box of fig. 7.3), whereas Raman and PL measurements performed before (in black) and after (in red) irradiation in this region are shown on the right. Also, a schematic sketch of the region far from the α source and of Raman and PL measurements performed before (the black ones) and after (the green ones) irradiation in this region are presented in fig. 7.7. If referring to the canonical Raman and PL spectrum of a single-crystal diamond (refer to fig. A.1 of Appendix A), some considerations can be deduced. All the spectra show the diamond peak in its theoretical position (1332 cm^{-1}), with a FWHM close to that of natural diamond ($\approx$ 4 cm^{-1}), either before and after the irradiation. A magnification of the Raman line of diamond is shown in fig. 7.8 before (black) and after (red) irradiation for a selected point, namely d1, but the same was found on all the other measurement points. However, in some

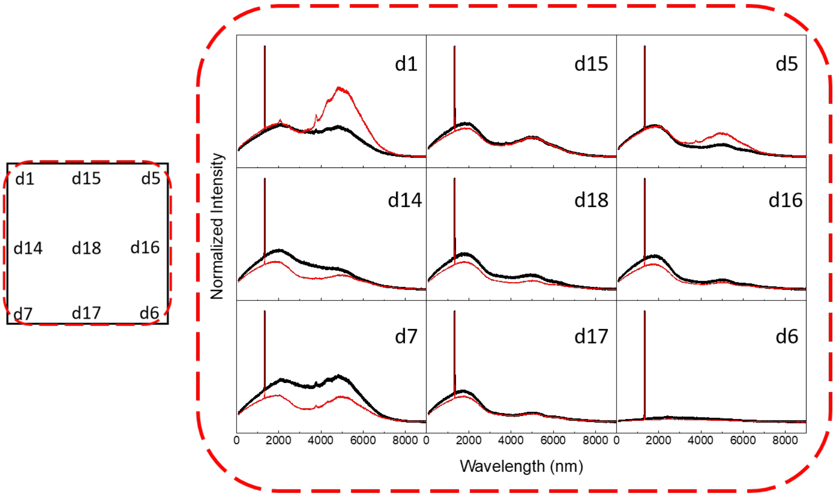

Figure 7.6: *A schematic sketch of the more intensely irradiated region on the left (i.e. red dashed box of fig. 7.3) with Raman and PL spectra of the measured points on the right. Black lines represent the measurements before irradiation whereas red lines represent the measurements after irradiation.*

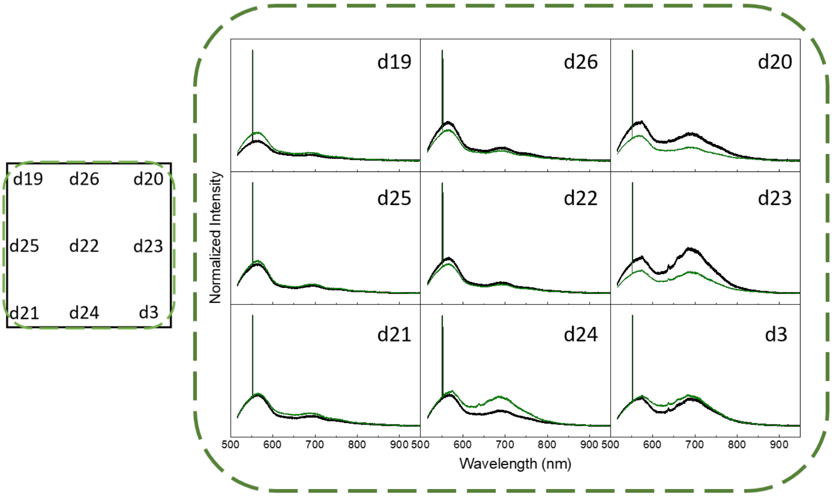

Figure 7.7: *A schematic sketch of the less intensely irradiated region on the left (i.e. green dashed box of fig. 7.3) with Raman and PL spectra of the measured points on the right. Black lines represent the measurements before irradiation whereas green lines represent the measurements after irradiation.*

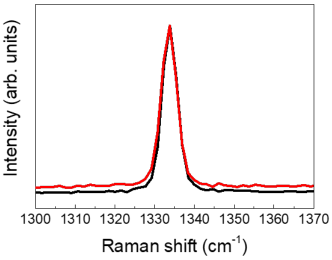

Figure 7.8: *Magnification of the Raman peak of diamond taken on the d1 point of sample DET, where black like represents the characterization before the irradiation and red line is the characterization after neutron irradiation. The same was found on all the other points of measurements.*

parts of the detector this peak emerges from three broad bands: a first band (called band A) centered at 570 nm, a second band in the range 600 - 670 nm (here labeled band B) and a third band centered at around 700 nm (called band C). In fig. 7.9 one of the spectra taken before the irradiation is shown, with a focus on the part of the spectrum with the bands. Regarding the nature of these bands, both their shape and their position in the spectra exclude to assign them to a Raman contribution from the

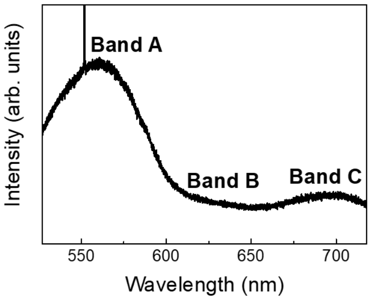

Figure 7.9: *A magnification of the three PL bands found in some points of measurement of sample DET, before the irradiation: band A centered at 570 nm, band B in the range 600 - 670 nm and band C centered at 700 nm..*

single-crystal diamond (see fig. A.1). For this reason, it is reasonable to suppose that they derive from PL transitions, and some hypothesis can be drawn:

- bands A and B are, by literature, not ascribable either to diamond lattice vibrations and other carbon features [168–170]. Indeed, being single-crystal diamond an homogeneous material, one would expect to find them in every part of the sample. On the contrary, not all the spectra show their contribution, as it is possible to see from figs. 7.6 and 7.7. Additionally, single-crystal diamond is a transparent material, and the fabrication of either the whole device (diamond, electrodes, support and metallic casing) under industrial patent; thus, a valid hypothesis would attribute these contributions to the unknown technology adopted for the detector fabrication and encapsulation, and detectable behind the single-crystal diamond;
- band C can be attributed to a weak PL contribution from diamond, as can be seen comparing fig. 7.9 with the Raman and PL spectrum of a typical Optical Grade polycrystalline diamond as bought from Element Six (inset b) of fig. 6.2). Normally, a single-crystal diamond should not have this PL contribution (as also shown by the characterization of sample DIA before neutron irradiation, see fig. 7.3). The fact that, in our measurements, band C is detectable even before the irradiation, can be attributed to crystalline defects induced by past irradiation experiments and giving a PL contribution.

Also, a measurement on the front electrode was performed, to verify whether these bands contribution could derive from the rear electrode with unknown dimension and geometry, and the electrode spectrum was superimposed to the spectrum of fig. 7.9, where the bands are clearly visible. Measurements are reported in fig. 7.10.

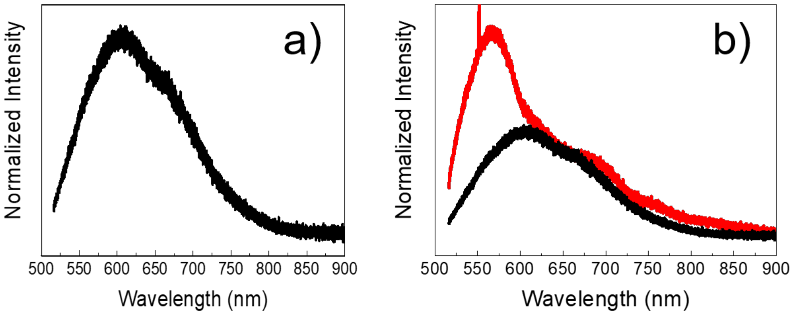

Figure 7.10: *a) PL spectrum of the front electrode on the left and b) superimposition of the front electrode spectrum with the spectrum of fig. 7.9.*

Being the electrode composed by a metal-based material, broad PL bands appear in the spectrum (see inset a) of fig. 7.10), with no Raman signals. By superimposing its spectrum to a Raman and PL spectrum of DET (see inset b) of fig. 7.10), it is possible to observe that, in the range where the band B is found, the DET spectrum has a shape similar to that of the electrode. Thus, we attribute the band B contribution to the presence of the rear electrode with a specific geometry, diverse from the one of the front electrode. Additionally, also measurements taken in the other points of the detector (i.e. not belonging to the selected regions) are shown in fig. 7.11. Particularly, orange dashed box identify measurements on the corners of DET, whereas blue dashed box identify measurements around the front electrode.

The fact that, in characterization measurements taken around the front electrode, the A and B bands are weak or almost absent (on the contrary of the measurements taken in the corners and according to measurements near the front electrodes in the red and green dashed box, see figs. 7.6 and 7.7), further confirms that a certain and unknown geometry is found under the single-crystal diamond. Being the material transparent, this geometry has a PL contribution detected while measuring the diamond and thus influencing the global shape of the Raman and PL spectra.

However, besides the influence in the spectra of this unknown geometry, at a first glance some information can be deduced regarding spectra before and after irradiation:

- as already shown, before and after irradiation no shift or broadening are measured on the Raman diamond peak, see fig. 7.8. This means that, in general, the crystalline quality of the single-crystal diamond is not noticeably affected by the α irradiation;
- the global shape of the spectra of the A and B bands, where present, does not change. In light of previous observations regarding the nature

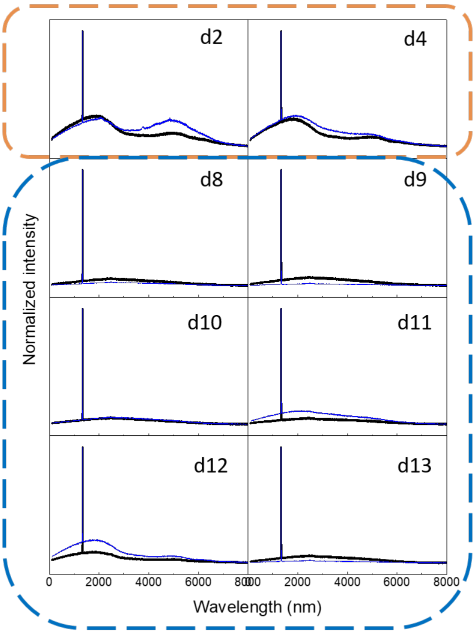

Figure 7.11: *Raman and PL spectra of the other points of measurements before (black) and after (blue) irradiation are shown. Particularly, the orange dashed box identifies the two corner points of the detector, whereas the blue dashed box identifies measurement points around the upper electrode.*

of these bands as belonging to device components placed behind the single-crystal diamond, this fact can be easily explained: having α particles a short range in the material (around 13 μm, as reported in chapter 1), and being the detector 500 μm thick, irradiation can not affect the components placed behind the single-crystal diamond;

- some points of measurements show a more marked difference in the spectrum near the band C before and after irradiation, mainly points located at the borders and corners of the detector, i.e. points d1, d5, d7, d20, d23 and d24. A magnification of this part of the spectrum for these measurement points is shown in fig. 7.12: being a PL contribution, in such picture the x-axis has been converted from wavelength to the respective energy values, as explained in Appendix A. Since band C is the only PL contribution ascribable to the SCD, the fact that only this part of the spectrum in some points of measurement undergoes a shape change is ascribable to modifications in the crystalline structure of the diamond it-self. Particularly, features found in these spectra are in accordance with typical

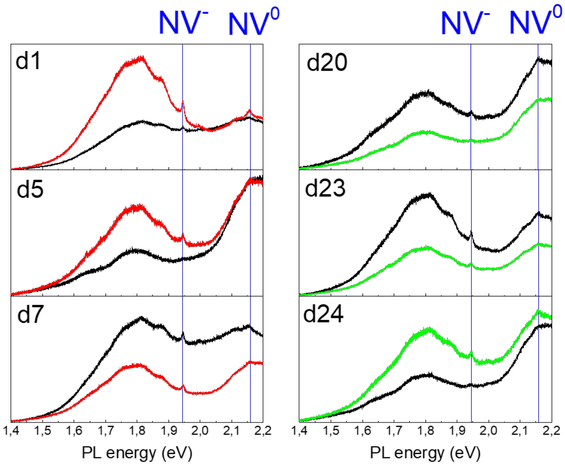

Figure 7.12: *PL spectra of DET before (black) and after (red and green) irradiation and belonging to selected points of measurement, namely d1, d5, d7, d20, d23 and d24.*

nitrogen vacancy defect center contribution, both in its neutral (NV^0) and negatively charged (NV^-) form. This is not surprising, since it is quite recorded in literature that, after irradiation, this defect can be induced in diamond, that already has some nitrogen diluted as impurity into the bulk [171]. From the spectra of fig. 7.12 it is possible to appreciate how in some parts the directly irradiated region seems to present a higher contribution, after the irradiation, coming from NV^- and NV^0 centers, with the exception of the d7 point, where the spectrum changes in intensity but maintains basically the same shape (so no actual difference is found). On the other side, the NV^- and NV^0 contributions tend to decrease in the region far from the irradiated one. However, in the d24 point again an increase in the signal coming from the NV^- center is detected. A first hypothesis suggests that, even if far from the irradiated region, being the α source emission isotropic, some lattice damage has been recorded even in this region. The fact that, even before irradiation, signals coming from NV^- and NV^0 defects are found, is ascribable to lattice damage due to irradiations performed previous to this study.

Part IV

Conclusions and perspectives

Chapter 8

Conclusions and perspectives

8.1 Brief summary

Nowadays diamond solid-state detectors represent an appealing technology for radiation detection. Their extreme radiation hardness and excellent electrical properties are justifying the slow substitution of common silicon-based technology in harsh radiation environments. However, as every new technology, there are still several issues that must be overcome in order to spread their use and make them competitive. Particularly, three different features can be identified, strongly influencing the diamond solid-state detector performance. First of all, the material, that has to be either of good quality for the purposes and cost competitive. Artificial synthesis of diamond has always been a challenging task, especially if the intention is to produce a single-crystal diamond, where several strict requirements on the fabrication process imply expensive costs. As free of defects, a single-crystal material shows better detection properties with respect to a polycrystalline one. However, if a polycrystalline diamond can be produced with a less expensive process and lower crystalline quality but showing detection properties closed to that of a single-crystal material, this would represent a good compromise. For doing this, the deposition process must be finely controlled, and diamond growth behavior and dynamics must be widely known. Second, the fabrication of proper conductive electrodes is fundamental, since their task is to collect the charge carriers generated by the diamond - radiation interaction in order to produce a measurable signal bringing information about the incoming radiation. Metallic contacts have been investigated so far, but in the last years the idea of an all carbon-based detector is earning much attention, and several procedures for graphitic electrodes production are under study. Indeed, either than being an excellent electrical conductor, graphite is also the stable carbon allotrope phase, easily obtainable with common deposition techniques. Two graphitic electrodes configurations are proposed in literature, the standard "sandwich" one with two electrodes deposited on two opposite faces of the diamond, and the "3D" solution where graphitic micro-channel are written in the diamond bulk by means of laser. Even if showing a better efficiency, the 3D configuration fabrication process can produce cracks in the material, thus deteriorating it. Finally, if the general idea is to use diamond for intense radiation fields and wherever its radiation hardness allows more accurate and long-lasting performance with respect to other solid-state detectors, of course its behavior under irradiation must be deeply known and verified, since a *polarization effect* has been recorded under certain irradiation conditions, with a net effect of charge collection efficiency reduced.

Basing on all these aspects, in this doctoral thesis project a dedicated work about all the above mentioned features influencing diamond detectors performance have been done, and the conclusions drawn will be the main subject of this chapter, together with the analysis of the possible future perspectives of this work.

8.2 Conclusions

As introduced in the chapter 3, this work addresses two main subjects. The first one is about the investigation of the dynamics of the first stages of nanocrystalline diamond growth, and the second one regards more general issues related to the diamond detector technology, i.e. the fabrication of graphitic contacts and the investigation of diamond detector behavior under irradiation.

In the first subject of the work, the dynamics of the first stages of polycrystalline diamond growth was investigated, with an experimental approach involving the use of a peculiar, not common but, at the same time, suitable deposition technique, i.e. the DC-μP, and the exploitation of appropriate material characterization techniques such as SEM, Raman and XRD, with a detailed analysis of the obtained results. The general approach involved the use of various substrates materials, having different tendency in interacting with carbon, and without performing substrate pre-treatment, in order to investigate the growth on the bare element. Nanocrystalline diamond was deposited increasing deposition time, and the growth was followed and characterized step by step. Basing on the results presented in chapter 5, the following conclusions can be given.

- Nanocrystalline diamond were deposited on different substrates and without substrate pre-treatment. Particularly, Mo, Si, W, Ni, Fe and Rh were used. Diamond samples were obtained with relative fast depositions (coalescence of diamond grains in a continuous layer obtained within 1 hour on all substrates).

- A general common mechanism of growth in the early stages of diamond grains formation was found on all substrates. Indeed, there is experimental evidence that the formation of a graphite layer prior to diamond growth triggers the nucleation of diamond. Additionally, we observe this graphitic layer even if deposition conditions such that only diamond phase is stable were chosen.
- A deep analysis of the Raman spectra of graphite formed in the first stages of growth and of the Raman spectra of nanocrystalline diamond obtained for longer deposition time suggests that a correlation between graphite features and the quality and sp^3/sp^2 content of nanocrystalline diamond are linked. The features of the graphitic layer influence the subsequently grown nanocrystalline diamond. For instance, on substrates as Ni and Fe, with the highest carbon diffusivity among the substrate materials analyzed, a crystalline graphite was formed in the first stages of growth, and nanocrystalline diamond with the highest sp^3/sp^2 content was subsequently grown. On Rh, the only nanostructured substrate, the less stressed graphitic system was grown and also the less stressed diamond. These are important observations for achieving a deep knowledge and control of the deposition process.
- A Raman characterization of the first stages of growth was performed, also with a double-wavelength approach. No similar works are found in literature regarding the characterization and investigation of the first stages of diamond growth.
- An investigative study about the deposition of thick nanocrystalline diamond films with the DC-μP were performed. Particularly, the deposition of diamond spots with thickness relevant for detectors application were achieved, even if with a lack of uniformity either in thickness and substrate covering. However, this represents a first, encouraging result towards the feasibility of exploiting this deposition technique not just for material science studies, but also for diamond film production. Of course, some dedicated improvements in the device set-up and deposition procedure must be accurately evaluated.

Regarding the graphitic electrodes production, an introductory study was made with the aim of producing graphite contacts on polycrystalline diamond substrates by means of a physical vapor deposition technique, namely the PLD. At this purpose, it is possible to conclude that:

- compact films of carbon were successfully deposited on polycrystalline diamond, showing good adhesion and uniform thickness along the whole deposited area;
- these films were characterized by means of Raman spectroscopy, showing an amorphous, homogeneous structure;

- different annealing procedures were tested, with the aim of graphitizing the amorphous films, involving thermal annealing and laser annealing treatments; particularly, the last one proved to be the most suitable for the aim of the work, either avoiding film delamination and producing the higher graphitization degree of the initial sample;

- thanks to some tests made also on amorphous carbon deposited on Si substrate, the experimental evidence that decreasing the film thickness the delamination can be avoided was obtained.

The last part of the work was devoted to introduce a material characerization strategy aiming at investigating modifications in the crystalline structure of the diamond bulk after exposure to irradiation. To this aim, neutron and α irradiations were performed on single-crystal diamond. Samples were characterized with a mapping approach by means of Raman and PL spectroscopy before and after exposure. The following observations can be deduced.

- In general, the proposed characterization strategy proved to be efficient and sensitive with respect to the aim of the work.

- Regarding fast neutrons irradiation, the characterization measurements show that diamond crystalline structure is not affected by the neutron fluence used in this work (i.e. 4.5 x 10^{12} n cm^{-2}), thus confirming the radiation hardness of this material.

- Regarding α irradiation, the spectroscopic characterization shows that the diamond crystalline quality is not affected by the irradiation (diamond peak position and FWHM do not change noticeably), however a PL background increases in some measurement points, confirming that a local variation in the diamond crystalline structure occurred during irradiation.

- The introduction of nitrogen vacancy defect centers were observed as a result of α irradiation, either in the neutral or negatively charged form. A role for these optical centers can be hypothesized in the *polarization effect*, since they introduce levels in the diamond band gap potentially acting as traps for charge carriers. However, this supposition have to be verified with dedicated experiments.

8.3 Future perspectives

Basing on the above mentioned main results, different possible future perspectives for this work can be evaluated. Particularly, about the first subject of the work:

- depositions moving the substrate can be implemented. Indeed, the DC-μP device is equipped with a translating apparatus that can keep the substrate in movement with respect to the hollow-cathode. With an optimized procedure, it would be possible to perform depositions where the "tales" of the quasi-gaussian profile of the deposition spots can sum. It this way, a uniform thickness and covering of the substrate would be achieved.

- An RF plasma source can be thought as a valid investment for the DC-μP device upgrade. In this way, also depositions on non conductive substrates would be possible. Additionally, homoepitaxial deposition on single-crystal diamond substrates could be implemented.

- Exploiting the extreme versatility of the DC-μP set-up regarding the deposition of different kind of carbon samples, the production of graphitic electrodes on single-crystal and polycrystalline diamond films would represent a valid and interesting continuation of this work.

- Since the deposition of diamond with this device is preceded by the spontaneous deposition of a graphitic layer, it would be surely interesting to optimize the process of diamond films deposition with the DC-μP in order to produce, with the DC-μP, a polycrystalline diamond detector: the graphitic layer would represent one of the planar electrodes, the polycrystalline diamond the active volume of the material. The other electrode could be finally deposited on the top surface of the diamond film simply changing process parameters in order to produce a graphitic film.

As the deposition of graphitic electrodes with PLD technique revealed first, promising results, the following works would be of interest:

- the optimization of the laser-graphitization procedure, in order to have a graphite film with a better crystalline quality and also to achieve a graphitization of the whole sample and not just in a spot with the laser dimension;

- the possibility of verifying the ohmic behavior of the as-produced electrodes with I-V characteristics measurements.

Finally, about the characterization strategy proposed for the understanding of the *polarization effect*, a natural continuation of the study would be:

- to perform prolonged α irradiation in order to confirm the correlation between the formation of nitrogen vacancy defect centers and the *polarization effect*;

- to perform prolonged neutron irradiation in order to create a measurable damage in the diamond bulk and evaluate the *polarization effect*;
- also, to perform prolonged neutron irradiation to quantify the radiation hardness of single-crystal diamond;
- to exploit this strategy before and after irradiation of diamond samples grown with the DC-μP, in order to analyze their performance and investigate the feasibility of using these samples for radiation detection purposes.

Appendix A

Main Raman and PL features of carbon materials

Every atom has its own unique vibrational signature, determined not only by the atom itself, but also by the characteristics of the individual bonds. Particularly, Raman spectroscopy is extremely sensitive to carbon-based compounds. This technique allows to identify the various allotropic forms of carbon, also thanks to a dispersive and resonant behavior that the various carbon allotropes have with different wavelengths, resulting in spectra where the same peak, mark of a specific vibrational mode, can be found in different positions when changing the excitation wavelength. Information about lattice disorder, presence of impurities, stress states and amorphous phases, cristallinity degree and qualitative sp^3/sp^2 ratio can be obtained. Additionally, with the same spectrometer, also photoluminescence (PL) spectra can be measured, acquiring information about chemical defects and impurities of samples.
All carbon samples present some common features in Raman spectra, all located in the 0 - 3000 cm^{-1} range of the spectrum, and some of them are shown in fig. A.1.

Graphite

The typical Raman spectrum of graphite, i.e. sp^2 crystalline phase, is revealed by the presence of the sharp G peak at 1582 cm^{-1}, associated with in-plane symmetric C-C stretching (see fig. A.1). This is one of the two Raman active modes for crystalline graphite, since at this frequency there is a peak in the phonon density of states (PDOS) and, at the same time, the Raman selection rule $\mathbf{q} = 0$ is satisfied, see fig. A.2. The other active mode is found at 42 cm^{-1} and it is not detectable by the Raman spectrometer

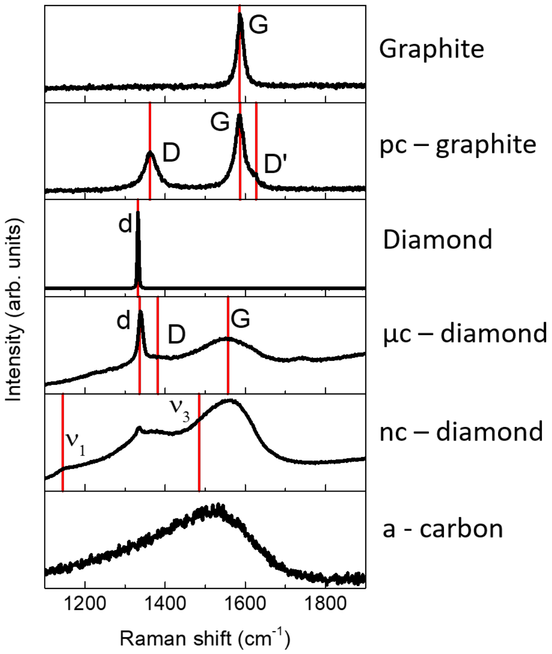

Figure A.1: *Typical Raman spectra of different carbon systems. From the top to the bottom, respectively: graphite, polycrystalline graphite, diamond, microcrystalline diamond, nanocrystalline diamond and amorphous carbon.*

used in this work, so it will not be considered for further analysis.
However, if a certain degree of disorder is present in the carbon material, the description get more complicated, and other Raman modes become active. In the case of polycrystalline graphite, two dispersive, defect-activated peaks, known as D (green circle of fig. A.2) and D', appear in the spectrum, whose position depends on the wavelength used to excite (respectively at 1370 cm^{-1} and 1626 cm^{-1} when using $\lambda = 457$ nm, i.e. blue excitation) and both explained by a double resonant Raman process and strictly related to the presence of sp^2 aromatic rings [172]. A third Raman feature at about 2740 cm^{-1} (again when using $\lambda = 457$ nm) is the second-order graphite peak, known as 2D, whose properties are related to the number and stacking order of graphitic layers [136, 143, 144]. For the peculiar case of monolayer graphene, the 2D peak is composed by a single-Lorentzian curve at 2720 cm^{-1} (when using $\lambda = 457$ nm), about 24 cm^{-1} wide and with an intensity higher than the G peak. As the number of layers increases, the 2D peak undergoes a modification in shape, position, width and intensity, depending specifically on the stacking order among layers. The split in two distinct

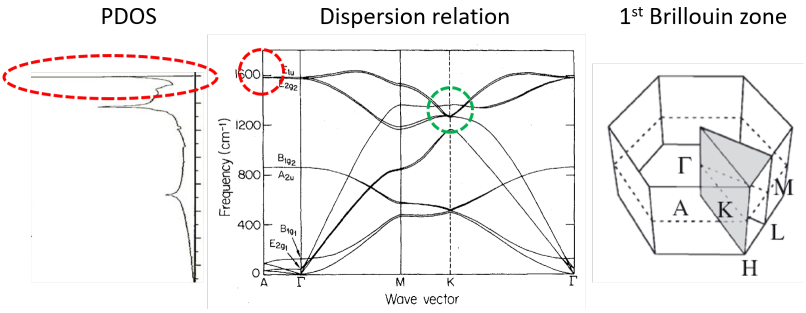

Figure A.2: *Dispersion relation of graphite with phonon density of states (PDOS) as a function of frequency (cm^{-1}). The only first-order Raman active mode of crystalline graphite is highlighted by the red dashed circle, whereas the blue circle identify the D mode. Also, a sketch of the first Brillouin zone is reported on the right.*

components is the signature of crystalline graphite with Bernal stacking order (i.e. ABA stacking of layers), while for turbostratic graphite (TG), in which layers are randomly oriented, the 2D peak still has a single-Lorentzian shape as in the case of monolayer graphene, but with a reduced intensity and a larger width (up to 100 cm^{-1}). Generally speaking, the accepted nomenclature [173] refers to Few-Layer Graphene (FLG) when the number of layers ranges between 2 and 5, Multi-Layer Graphene (MLG) up to 10 layers, and graphite (G) for more than 10 layers. Decreasing grain size, both G and D peaks broaden and shift [174], finally merging in a two-bands spectrum for amorphous carbon (a-C), also in its hydrogenated form (a-C:H) [127, 175]. The analysis of position, width, relative intensities and dispersive behavior of the D and G bands allows to interpret this kind of spectrum, and requires the exploitation of some fitting models [54, 110, 127].

Diamond

For single-crystal diamond (i.e. sp^3 crystalline phase), Raman spectrum shows a single, non-dispersive, well-defined, first-order peak centered at 1332 cm^{-1}, which corresponds to the vibrations of the two interpenetrating cubic sub-lattices of the diamond structure (see fig. A.1). This is the only Raman active mode for single-crystal diamond, since for such frequency the Raman selection rule is satisfied (see fig. A.3).

For the case of polycrystalline diamond, the Raman spectrum is still characterized by the diamond peak at 1332 cm^{-1} (that, in this work, will be labeled as "d"), that can show a slight broadening and red-shift due to grains dimension reducing, presence of residual stress or other imperfections. The d peak is always accompanied by the D and G bands described above, revealing the existence of non-diamond carbon

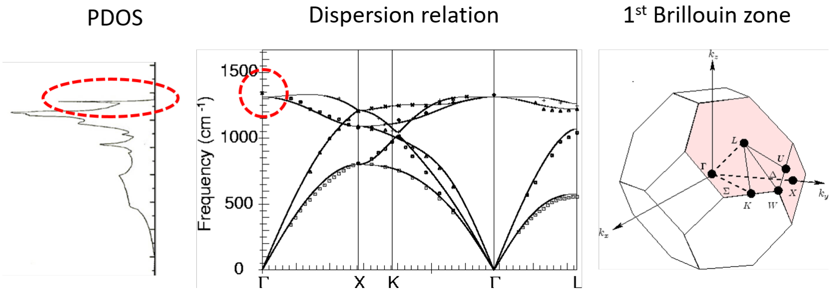

PDOS

Dispersion relation

1st Brillouin zone

Figure A.3: *Dispersion relation of diamond with phonon density of states (PDOS) as a function of frequency (cm^{-1}). The only Raman active mode of single-crystal diamond is highlighted by the red dashed circle.*

(amorphous carbon a-C or hydrogenated amorphous carbon a-C:H), which is expected to reside at the grain boundaries [125, 127]. With decreasing grain size, moving to nanocrystalline diamond or ultra-nanocrystalline diamond [125, 176], the Raman spectrum is further modified: the d peak is strongly reduced in intensity, and a wide structure band dominates, composed by the G and D bands of the amorphous carbon and by other two features called ν_1 and ν_3 and centered at about 1150 cm^{-1} and 1480 cm^{-1} respectively, and associated to vibration modes of *trans-polyacetylene* (t-PA). Again, both amorphous carbon and fragments of *trans-polyacetylene* are expected to be located at the grain boundaries of the diamond nano-crystallites [126, 177].

Effect of excitation wavelength

The fact that sp^2 presents a higher Raman cross-section and stronger absorption in the wavelength visible range justifies the predominance of this fraction in the Raman spectrum of polycrystalline diamond, and this is even more true if a nanocrystalline structure is present [127]. Additionally, hydrogen saturation of non-radiative recombination centers in a-C:H is responsible for a PL increasing background in the visible spectrum [178]. However, one of the power of this characterization technique relies in the possibility of tuning the excitation wavelength, taking in this way advantage from the dispersion and resonant behavior of some Raman features mentioned above. Indeed, moving to UV excitation wavelength, the following phenomena are expected [105, 128, 129, 179]: i) decreasing of the dominant resonance deriving from sp^2 carbon atoms, together with an increase of the resonance of the sp^3 carbon atoms, ii) suppression of the PL background, iii) decreasing in intensity and shift towards higher wavenumber of the D peak, iv) decreasing of the t-PA contribution. As a consequence, the UV Raman spectrum allows to easily appreciate the d peak. On the other hand, the combined use of visible and UV Raman spectroscopy is essential for characterizing both diamond and non-diamond fractions of polycrystalline samples. As an example, Raman spectra of polycrystalline diamond taken at different wavelengths (514.5, 457 and 325 nm) for a typical deposit by DC-μP in the process conditions that have been used in this work are reported in fig. A.4. For a detailed description and interpretation of this spectra, refer to chapter 5. To now, this image is just sufficient to show that the diamond peak is present but superimposed by the two D and G bands previously mentioned. Additionally, the PL contribution almost obscure Raman signal when using the green line, while moving to the blue line it becomes distinguishable, even though a slight and nearly linear background is still present. With UV excitation, the PL contribution is completely absent, the d peak is more visible and the D and G bands shift towards higher wave numbers and decrease in intensities.

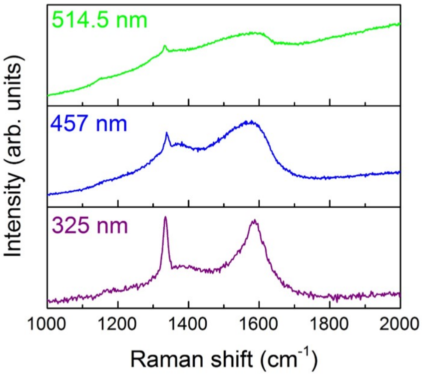

Figure A.4: *Raman spectra of polycrystalline diamond deposited on Mo substrate taken at three different wavelengths: as can be seen, the PL backgroud is gradually suppressed when moving from visible to UV excitation.*

As can be deduced, for such a complicated system as polycrystalline diamond is, where coexistence of different carbon phases and allotropes is found, Raman spectroscopy represents an essential tool to investigate the material.

Photoluminescence of diamond

As introduced in chapter 2, also the PL contribution can be acquired when performing a Raman spectroscopic measurement, linked to the presence of chemical defects in diamond. There are more than 100 defects that can be found in diamond, the most abundant one due to nitrogen impurity in the crystal lattice. Since this is the case found in this work, an example of the PL spectrum of a polycrystalline diamond with a non-negligible PL contribution from such kind of defect is found in fig. A.5.

In this picture, the part of the spectrum where Raman frequencies are found has been cut-off. Also, the x-axis has been converted from Raman shift to wavelength, but also energy values are admitted to describe a PL spectrum. Using letters x, y,z and λ to define the Raman shift (cm^{-1}), the wavelength (nm), the energy value (eV) and the laser wavelength used to excite respectively, the conversion is:

$$y = \frac{10^7}{\frac{10^7}{\lambda} - x}$$

$$z = \frac{1240}{y}$$

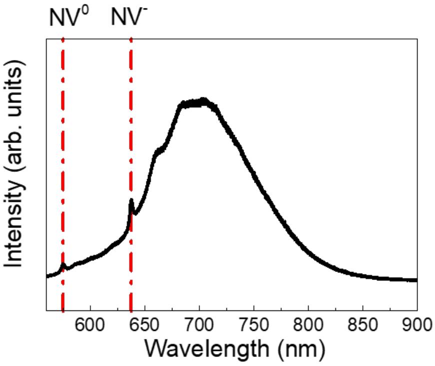

Figure A.5: *Example of the PL spectrum of a single-crystal diamond with nitrogen vacancy defect centers.*

In this spectrum, broad bands are found along the whole spectrum wavelengths, related to electronic band-to-band transitions in the material as a consequence of the absorption of incoming light. Particularly, nitrogen atoms can be found in bulk diamond as chemical impurities absorbed (either intentionally or not) during the growth process. These atoms produce strains in the diamond lattice, and thus can efficiently bond to a vacancy, giving rise to the so-called nitrogen vacancy defect center [171]. In such kind of defect, a nitrogen atom and its vacancy substitute two nearest carbon atoms. It can exists in two states, the negatively charged (in fig. A.5 labeled as NV^-) that shows an absorption peak at 640 nm and the neutral form (in fig. A.5 labeled as NV^0) with the respective absorption peak around 575 nm. The NV^0 has one unpaired electron and is thus paramagnetic. Both NV^- and NV^0 are immobile at room temperature, and an annealing process is required to move them. Also, an important property of the nitrogen vacancy defect centers is the temporal stability. Because of their features, these defects can confer diamond a certain number of desirable properties that allow to use it in various fields.

Appendix B

Temperature gradient across the substrate holder during diamond deposition with DC-μP

Referring to the DC-μP set-up, the electrical equivalent circuit is represented in fig. B.1. This sketch is useful to calculate the temperature gradient across the Mo substrate holder strip. On the basis of the voltage V_s and current I_s supplied, known the resistance circuit R_c, it is possible to calculate the voltage at the micro-hollow cathode $V_{\mu hc}$ as:

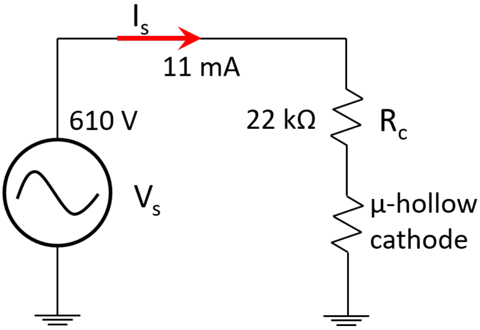

Figure B.1: *Electrical equivalent circuit of the DC-μP set-up.*

$$V_{\mu hc} = V_s - (I_s \times R_c) = 368\ V$$

and thus the power P_s*ubs* supplied to the substrate holder as:

$$P_{subs} = V_{\mu hc} \times I_s = 4\ W$$

At this point, three hypothesis can be drawn, to calculate the temperature gradient across the substrate holder.

1^{st} hypothesis

The whole substrate holder dissipates the incoming P_{subs} power.

In such a case, having the substrate holder a rectangular dimension with 3 cm length and 1 cm width, and a thickness of about 0.1 mm, and being the Mo thermal conductivity k around 1300 K (i.e. near the deposition temperature) about 100 W m^{-1} K^{-1}, the following thermal balance can be written:

$$\frac{k \times \Delta T}{s} = \frac{P_{subs}}{A}$$

where ΔT represents the temperature gradient across the substrate holder with thickness s and surface area A. Thus, the temperature gradient is estimated to be around 0.013 °C.

2^{nd} hypothesis

Adiabatic solution: the P_{subs} power is dissipated only at the microhollow dimension.

In this case, being the power dissipated only in the deposit region with the dimension of the plasma (diameter of 178 μm), the area A is calculated as:

$$A = \pi \times (\frac{178}{2} \times 10^{-6})^2 = 2.5 \times 10^{-8}\ m^2$$

and the temperature gradient, estimated with the same formula of the 1^{st} hypothesis, becomes 160 °C.

3^{rd} hypothesis

Intermediate situation: the P_{subs} power is dissipated along the deposited area (0.28 mm^2).

As can be seen from SEM images presented in chapter 5, and from results of section 5.5, the deposition proceeds also outside the plasma plume diameter, till a dimension of 0.28 mm^2 for 7 hours of deposition, that seems to be a saturation value (being the same at 5 hours of deposition). For this reason, also this situation was considered, being intermediate among the first two hypothesis. In such a case, the temperature gradient can be estimated as equal to 14.3 °C.
Of course the first two hypothesis represent limit configurations and thus it is reasonable to suppose that none of the calculated values is realistic. The third hypothesis seems more realistic and furnishing a reasonable order of magnitude for the temperature gradient across the substrate holder (and

thus for the measurement mistake made when placing the thermocouple in the configuration described in chapter 4).

List of Figures

List of Tables

Bibliography

(1) Zhu, Y.; Murali, S.; Cai, W.; Li, X.; Suk, J. W.; Potts, J. R.; Ruoff, R. S. *Advanced Materials* **2010**, *22*, 3906–3924.

(2) May, P. W. *Philosophical Transactions of the Royal Society of London Series a-Mathematical Physical and Engineering Sciences* **2000**, *358*, 473–495.

(3) Gracio, J. J.; Fan, Q. H.; Madaleno, J. C. *Journal of Physics D-Applied Physics* **2010**, *43*, 374017.

(4) Hess, P. *Journal of Applied Physics* **2012**, *111*, 051101.

(5) Behnke, T.; Oh, A.; Wagner, A.; Zeuner, W.; Bluhm, A.; Klages, C. P.; Paul, M.; Schafer, L. *Diamond and Related Materials* **1998**, *7*, 1553–1557.

(6) Mainwood, A. *Diamond and Related Materials* **1998**, *7*, 504–509.

(7) Giacomelli, L.; Andreani, C.; Fazzi, A.; Frost, C. D.; Gorini, G.; Cippo, E. P.; Pietropaolo, A.; Rebai, M.; Schuhmacher, H.; Tardocchi, M.; Verona, C.; Rinati, G. V.; Zimbal, A. *Nuclear Physics B-Proceedings Supplements* **2011**, *215*, 242–246.

(8) Adam, W. et al. *Nuclear Instruments & Methods in Physics Research Section a-Accelerators Spectrometers Detectors and Associated Equipment* **2003**, *511*, 124–131.

(9) Knoll, G. F., *Radiation Detection and Measurement*, Google-Books-ID: HKBVAAAAMAAJ; Wiley: 2000; 826 pp.

(10) Brambilla, A; Bergonzo, P; Foulon, F; Jany, C; Pochet, T *Nuclear Instruments and Methods in Physics Research Section A: Accelerators, Spectrometers, Detectors and Associated Equipment* **1996**, *380*, 446–449.

(11) Kumar, A.; Singh, A.; Kumar, A.; Topkar, A. *Nuclear Instruments and Methods in Physics Research Section A: Accelerators, Spectrometers, Detectors and Associated Equipment* **2015**, *785*, 55–60.

(12) Giacomelli, L.; Rebai, M.; Perelli Cippo, E.; Tardocchi, M.; Fazzi, A; Andreani, C.; Pietropaolo, A.; Frost, C.; Rhodes, N.; Shooneveld, E.; Gorini, G. *FUNFI Workshop on Fusion for Neutrons and Sub-critical Nuclear Fission*, Varenna (12 - 15 September 2011).

(13) Karkin, A. E.; Voronin, V. I.; Berger, I. F.; Kazantsev, V. A.; Ponosov, Y. S.; Ralchenko, V. G.; Konov, V. I.; Goshchitskii, B. N. *Physical Review B* **2008**, *78*, 033204.

(14) Allers, L.; Howard, A. S.; Hassard, J. F.; Mainwood, A. *Diamond and Related Materials* **1997**, *6*, 353–355.

(15) Mainwood, A.; Allers, L.; Collins, A.; Hassard, J.; Howard, A.; Mahon, A.; Parsons, H.; Sumner, T.; Collins, J.; Scarsbrook, G.; Sussmann, R.; Whitehead, A. *Journal of Physics D-Applied Physics* **1995**, *28*, 1279–1283.

(16) Angelone, M.; Pillon, M.; Balducci, A.; Marinelli, M.; Milani, E.; Morgada, M. E.; Pucella, G.; Tucciarone, A.; Verona-Rinati, G.; Ochiai, K.; Nishitani, T. *Review of Scientific Instruments* **2006**, *77*, 023505.

(17) Hodgson, M.; Lohstroh, A.; Sellin, P.; Thomas, D. *Nuclear Instruments & Methods in Physics Research Section a-Accelerators Spectrometers Detectors and Associated Equipment* **2017**, *847*, 1–9.

(18) Manfredotti, C.; Polesello, P.; Truccato, M.; Vittone, E.; Lo Giudice, A.; Fizzotti, F. *Nuclear Instruments & Methods in Physics Research Section a-Accelerators Spectrometers Detectors and Associated Equipment* **1998**, *410*, 96–99.

(19) `https://physics.nist.gov/cgi-bin/Star/ap_table.pl`.

(20) Hodgson, M.; Lohstroh, A.; Sellin, P. *Diamond and Related Materials* **2017**, *78*, 49–57.

(21) *Semiconductor Radiation Detectors - Device Physics | Gerhard Lutz | Springer*.

(22) Kozlov, S. F.; Stuck, R.; Hage-Ali, M.; Siffert, P. *IEEE Transactions on Nuclear Science* **1975**, *22*, 160–170.

(23) Rebai, M.; Fazzi, A.; Cazzaniga, C.; Croci, G.; Tardocchi, M.; Perelli Cippo, E.; Frost, C. D.; Zaccagnino, D.; Varoli, V.; Gorini, G. *Diamond and Related Materials* **2016**, *61*, 1–6.

(24) Chynoweth, A. G. *Physical Review* **1951**, *83*, 254–263.

(25) Lohstroh, A.; Sellin, P. J.; Wang, S. G.; Davies, A. W.; Parkin, J. M. *Journal of Applied Physics* **2007**, *101*, 063711.

(26) Marinelli, M.; Milani, E; Paoletti, A; Pucella, G; Tucciarone, A; Verona Rinati, G.; Angelone, M; Pillon, M *Diamond and Related Materials* **2003**, *12*, 1733–1737.

(27) Cazzaniga, C.; Sunden, E. A.; Binda, F.; Croci, G.; Ericsson, G.; Giacomelli, L.; Gorini, G.; Griesmayer, E.; Grosso, G.; Kaveney, G.; Nocente, M.; Cippo, E. P.; Rebai, M.; Syme, B.; Tardocchi, M. *Review of Scientific Instruments* **2014**, *85*, 043506.

(28) Rebai, M.; Andreani, C.; Fazzi, A.; Frost, C. D.; Giacomelli, L.; Gorini, G.; Milani, E.; Cippo, E. P.; Pietropaolo, A.; Prestopino, G.; Schooneveld, E.; Tardocchi, M.; Verona, C.; Rinati, G. V. *Nuclear Physics B-Proceedings Supplements* **2011**, *215*, 313–315.

(29) Donato, M. G.; Faggio, G.; Marinelli, M.; Messina, G.; Milani, E.; Paoletti, A.; Santangelo, S.; Tucciarone, A.; Verona Rinati, G. *Diamond and Related Materials* **2001**, *10*, 1788–1793.

(30) Girolami, M.; Bellucci, A.; Calvani, P.; Trucchi, D. M. *Physica Status Solidi a-Applications and Materials Science* **2016**, *213*, 2634–2640.

(31) Sellin, P. J.; Lohstroh, A.; Davies, A. W.; Galbiati, A.; Parkin, J.; Wang, S. G.; Simon, A. *Nuclear Instruments and Methods in Physics Research Section B: Beam Interactions with Materials and Atoms* **2007**, *260*, 293–298.

(32) Lagomarsino, S.; Bellini, M.; Brianzi, M.; Carzino, R.; Cindro, V.; Corsi, C.; Morozzi, A.; Passeri, D.; Sciortino, S.; Servoli, L. *Nuclear Instruments & Methods in Physics Research Section a-Accelerators Spectrometers Detectors and Associated Equipment* **2015**, *796*, 42–46.

(33) Wang, Y. Y.; Zhen, C. M.; Yan, Z. J.; Guo, Q. F.; Chen, G. H. *International Journal of Modern Physics B* **2002**, *16*, 927–931.

(34) Cazzaniga, C.; Frost, C. D.; Minniti, T.; Schooneveld, E.; Cippo, E. P.; Tardocchi, M.; Rebai, M.; Gorini, G. *Journal of Instrumentation* **2016**, *11*, P07012.

(35) Kononenko, T.; Ralchenko, V.; Bolshakov, A.; Konov, V.; Allegrini, P.; Pacilli, M.; Conte, G.; Spiriti, E. *Applied Physics A* **2014**, *114*, 297–300.

(36) Picollo, F.; Monticone, D. G.; Olivero, P.; Fairchild, B. A.; Rubanov, S.; Prawer, S.; Vittone, E. *New Journal of Physics* **2012**, *14*, 053011.

(37) Sellin, P. J.; Galbiati, A. *Applied Physics Letters* **2005**, *87*, 093502.

(38) Oh, A.; Caylar, B.; Pomorski, M.; Wengler, T. *Diamond and Related Materials* **2013**, *38*, 9–13.

(39) Alemanno, E.; Martino, M.; Caricato, A. P.; Corrado, M.; Pinto, C.; Spagnolo, S.; Chiodini, G.; Perrino, R.; Fiore, G. *Diamond and Related Materials* **2013**, *38*, 32–35.

(40) Lagomarsino, S.; Bellini, M.; Corsi, C.; Gorelli, F.; Parrini, G.; Santoro, M.; Sciortino, S. *Applied Physics Letters* **2013**, *103*, 233507.

(41) Lagomarsino, S.; Bellini, M.; Corsi, C.; Fanetti, S.; Gorelli, F.; Liontos, I.; Parrini, G.; Santoro, M.; Sciortino, S. *Diamond and Related Materials* **2014**, *43*, 23–28.

(42) Lattanzi, D.; Angelone, M.; Pillon, M.; Almaviva, S.; Marinelli, M.; Milani, E.; Prestopino, G.; Tucciarone, A.; Verona, C.; Verona-Rinati, G.; Popovichev, S.; Montereali, R. M.; Vincenti, M. A.; Murari, A. *Fusion Engineering and Design* **2009**, *84*, 1156–1159.

(43) Angus, J. C. *Diamond and Related Materials* **2014**, *49*, 77–86.

(44) Zhu, W.; Stoner, B. R.; Williams, B. E.; Glass, J. T. *Proceedings of the IEEE* **1991**, *79*, 621–646.

(45) Piekarczyk, W. *Journal of Materials Science* **1998**, *33*, 3443–3453.

(46) Lee, S. T.; Lin, Z.; Jiang, X. *Materials Science and Engineering: R: Reports* **1999**, *25*, 123–154.

(47) Williams, O. A. *Diamond and Related Materials* **2011**, *20*, 621–640.

(48) Piekarczyk, W. *Crystal Research and Technology* **1999**, *34*, 553–563.

(49) Piekarczyk, W.; Prawer, S. *Diamond and Related Materials* **1993**, *2*, 41–47.

(50) Das, D.; Singh, R. N. *International Materials Reviews* **2007**, *52*, 29–64.

(51) Liu, H.; Dandy, D. S. *Diamond and Related Materials* **1995**, *4*, 1173–1188.

(52) Polo, M. C.; Cifre, J.; Esteve, J. *Diamond and Related Materials* **1994**, *3*, 492–494.

(53) Kato, Y.; Goto, M.; Sato, R.; Yamada, K.; Koga, A.; Teii, K.; Srey, C.; Tanaka, S. *Surface and Coatings Technology* **2011**, *206*, 990–993.

(54) Long, F.; Wei, Q.; Yu, Z. M.; Luo, J.; Zhang, X.; Long, H.; Wu, X. *Journal of Alloys and Compounds* **2013**, *579*, 638–645.

(55) Faggio, G.; Donato, M. G.; Lagomarsino, S.; Messina, G.; Santangelo, S.; Sciortino, S. *Carbon: The Future Material for Advanced Technology Applications* **2006**, *100*, 329–343.

(56) Waite, M. M.; Shah, S. I. *Applied Physics Letters* **1992**, *60*, 2344–2346.

(57) Lambrecht, W. R. L.; Lee, C. H.; Segall, B.; Angus, J. C.; Li, Z.; Sunkara, M. *Nature* **1993**, *364*, 607–610.

(58) Belton, D. N.; Schmieg, S. J. *Thin Solid Films* **1992**, *212*, 68–80.

(59) Ong, T. P.; Xiong, F.; Chang, R. P. H.; White, C. W. *Journal of Materials Research* **1992**, *7*, 2429–2439.

(60) Li, X. J.; He, L. L.; Li, Y. S.; Yang, Q.; Hirose, A. *Acs Applied Materials & Interfaces* **2013**, *5*, 7370–7378.

(61) Stoner, B. R.; Ma, G.-H. M.; Wolter, S. D.; Glass, J. T. *Physical Review B* **1992**, *45*, 11067–11084.

(62) Morrish, A. A.; Pehrsson, P. E. *Applied Physics Letters* **1991**, *59*, 417–419.

(63) Singh, J.; Vellaikal, M. *Journal of Applied Physics* **1993**, *73*, 2831–2834.

(64) Ravi, K. V.; Koch, C. A. *Applied Physics Letters* **1990**, *57*, 348–350.

(65) Muller, J.; Antoni, F.; Fogarassy, E.; Le Normand, F. *Carbon* **1998**, *36*, 565–568.

(66) Goodwin, D. G. *Journal of Applied Physics* **1993**, *74*, 6888–6894.

(67) Goodwin, D. G. *Journal of Applied Physics* **1993**, *74*, 6895–6906.

(68) Butler, J. E.; Woodin, R. L.; Brown, L. M.; Fallon, P. *Philosophical Transactions of the Royal Society of London A: Mathematical, Physical and Engineering Sciences* **1993**, *342*, 209–224.

(69) Kumar, A.; Lin, P. A.; Xue, A.; Hao, B.; Yap, Y. K.; Sankaran, R. M. *Nature Communications* **2013**, *4*, 2618.

(70) Park, J.-W.; Kim, K.-S.; Hwang, N.-M. *Carbon* **2016**, *106*, 289–294.

(71) Shima-Edelstein, R.; Gouzman, I.; Hoffman, A. *Carbon* **2001**, *39*, 337–342.

(72) Shima, R.; Chakk, Y.; Hoffman, A. *Carbon* **2000**, *38*, 1839–1843.

(73) Chiang, M.-J.; Hon, M.-H. *Journal of Crystal Growth* **2000**, *211*, 211–215.

(74) Lee, S.-F.; Yeh, C.-S.; Chang, Y.-P.; Wang, D.-C.; Huang, B.-R. *Carbon* **2010**, *48*, 314.

(75) Mitsuda, Y.; Kojima, Y.; Yoshida, T.; Akashi, K. *Journal of Materials Science* **1987**, *22*, 1557–1562.

(76) Sawabe, A.; Inuzuka, T. *Thin Solid Films* **1986**, *137*, 89–99.

(77) Angus, J. C.; Wang, Y; Sunkara, a. M. *Annual Review of Materials Science* **1991**, *21*, 221–248.

(78) Yugo, S.; Kanai, T.; Kimura, T.; Muto, T. *Applied Physics Letters* **1991**, *58*, 1036–1038.

(79) Sun, C.; Zhang, W. J.; Wang, N.; Chan, C. Y.; Bello, I.; Lee, C. S.; Lee, S. T. *Journal of Applied Physics* **2000**, *88*, 3354–3360.

(80) Feng, Z.; Komvopoulos, K.; Brown, I. G.; Bogy, D. B. *Journal of Applied Physics* **1993**, *74*, 2841–2849.

(81) Yang, J.; Su, X.; Chen, Q.; Lin, Z. *Applied Physics Letters* **1995**, *66*, 3284–3286.

(82) Matsumoto, S.; Sato, Y.; Tsutsumi, M.; Setaka, N. *Journal of Materials Science* **1982**, *17*, 3106–3112.

(83) Cappelli, M. A.; Paul, P. H. *Journal of Applied Physics* **1990**, *67*, 2596–2602.

(84) Badzian, A. R.; Badzian, T.; Roy, R.; Messier, R.; Spear, K. E. *Materials Research Bulletin* **1988**, *23*, 531–548.

(85) Kurihara, K.; Sasaki, K.; Kawarada, M.; Koshino, N. *Applied Physics Letters* **1988**, *52*, 437–438.

(86) Kurihara, K.; Sasaki, K.; Kawarada, M.; Goto, Y., *Formation of Functionally Gradient Diamond Films*; Tzeng, Y., Yoshikawa, M., Murakawa, M., Feldman, A., Eds.; Elsevier Science Publ B V: Amsterdam, 1991; Vol. 73.

(87) Sankaran, R. M.; Giapis, K. P. *Journal of Physics D: Applied Physics* **2003**, *36*, 2914.

(88) Lin, L.; Wang, Q. *Plasma Chemistry and Plasma Processing* **2015**, *35*, 925–962.

(89) Becker, K. H.; Schoenbach, K. H.; Eden, J. G. *Journal of Physics D-Applied Physics* **2006**, *39*, R55–R70.

(90) Feng, H.; Shoujie, H.; Xiaofei, Z.; Bingang, G.; Jiting, O. *Plasma Science and Technology* **2012**, *14*, 1079.

(91) Schoenbach, K. H.; Moselhy, M.; Shi, W.; Bentley, R. *Journal of Vacuum Science & Technology A* **2003**, *21*, 1260–1265.

(92) Lazzaroni, C.; Chabert, P. *Journal of Physics D: Applied Physics* **2013**, *46*, 455203.

(93) Schoenbach, K. H.; ElHabachi, A.; Shi, W. H.; Ciocca, M. *Plasma Sources Science & Technology* **1997**, *6*, 468–477.

(94) Causa, F.; Ghezzi, F.; Dellasega, D.; Caniello, R.; Grosso, G. *Journal of Applied Physics* **2012**, *112*, 123302.

(95) Kim, G. J.; Iza, F.; Lee, J. K. *Journal of Physics D: Applied Physics* **2006**, *39*, 4386.

(96) Sankaran, R. M.; Giapis, K. P. *Journal of Applied Physics* **2002**, *92*, 2406–2411.

(97) Ghezzi, F.; Cacciamani, G.; Caniello, R.; Toncu, D. C.; Causa, F.; Dellasega, D.; Russo, V.; Passoni, M. *The Journal of Physical Chemistry C* **2014**, *118*, 24714–24722.

(98) Wang, J.-T.; Wan, Y.-Z.; Liu, Z.-J.; Wang, H.; Zhang, D. W.; Huang, Z.-Q. *Materials Letters* **1998**, *33*, 311–314.

(99) Zhang, D. W.; Wan, Y.-Z.; Liu, Z.-J.; Wang, J.-T. *Journal of Materials Science Letters* **1997**, *16*, 1349–1351.

(100) L. Regel, L.; R. Wilcox, W. *Acta Astronautica* **2001**, *48*, 129–144.

(101) Kadlečíková, M.; Vojs, M.; Breza, J.; Veselý, M.; Frgala, Z.; Michalka, M.; Matějková, J.; Vojačková, A.; Daniš, T.; Marton, M. *Microelectronics Journal* **2007**, *38*, 20–23.

(102) Hsu, W. L. *Applied Physics Letters* **1991**, *59*, 1427–1429.

(103) Wang, W. L.; Liao, K. J.; Fang, L.; Esteve, J.; Polo, M. C. *Diamond and Related Materials* **2001**, *10*, 383–387.

(104) Kundrat, V.; Zhang, X.; Cooke, K.; Sun, H.; Sullivan, J.; Ye, H. *Aip Advances* **2015**, *5*, 047130.

(105) Rudigier, M.; Haubner, R. *Analytical and Bioanalytical Chemistry* **2012**, *403*, 675–681.

(106) Sikder, A. K.; Sharda, T.; Misra, D. S.; Chandrasekaram, D.; Selvam, P. *Diamond and Related Materials* **1998**, *7*, 1010–1013.

(107) Wako, H.; Abe, T.; Takagi, T.; Ikohagi, T. *Applied Surface Science* **2009**, *256*, 1466–1471.

(108) Williams, O. A.; Daenen, M.; D'Haen, J.; Haenen, K.; Maes, J.; Moshchalkov, V. V.; Nesládek, M.; Gruen, D. M. *Diamond and Related Materials* **2006**, *15*, 654–658.

(109) Lee, S. T.; Peng, H. Y.; Zhou, X. T.; Wang, N.; Lee, C. S.; Bello, I.; Lifshitz, Y. *Science* **2000**, *287*, 104–106.

(110) Nistor, L. C.; Van Landuyt, J.; Ralchenko, V. G.; Obraztsova, E. D.; Smolin, A. A. *Diamond and Related Materials* **1997**, *6*, 159–168.

(111) Ferreira, N. G.; Abramof, E.; Leite, N. F.; Corat, E. J.; Trava-Airoldi, V. J. *Journal of Applied Physics* **2002**, *91*, 2466–2472.

(112) *Japanese Journal of Applied Physics* **2005**, *44*, 4122.

(113) Sun, X.; Li, Y.; Wan, B.; Yang, L.; Yang, Q. *Surface and Coatings Technology* **2015**, *284*, 139–144.

(114) Silva, F.; Bénédic, F.; Bruno, P.; Gicquel, A. *Diamond and Related Materials* **2005**, *14*, 398–403.

(115) Muller, J.; Antoni, F.; Fogarassy, E.; Le Normand, F. *Carbon* **1998**, *36*, 565–568.

(116) Yang, L.; Jiang, C.; Guo, S.; Zhang, L.; Gao, J.; Peng, J.; Hu, T.; Wang, L. *Nanoscale Research Letters* **2016**, *11*, 415.

(117) Buchkremer-Hermanns, H.; Ren, H.; Kohlschein, G.; Weiss, H. *Surface & Coatings Technology* **1998**, *98*, 1038–1046.

(118) Chiang, M.-J.; Hon, M.-H. *Journal of Crystal Growth* **2000**, *211*, 211–215.

(119) Gsell, S.; Berner, S.; Brugger, T.; Schreck, M.; Brescia, R.; Fischer, M.; Greber, T.; Osterwalder, J.; Stritzker, B. *Diamond and Related Materials* **2008**, *17*, 1029–1034.

(120) Aoyama, T.; Amano, N.; Goto, T.; Abukawa, T.; Kono, S.; Ando, Y.; Sawabe, A. *Diamond and Related Materials* **2007**, *16*, 594–599.

(121) Kono, S.; Shiraishi, M.; Plusnin, N. I.; Goto, T.; Ikejima, Y.; Abukawa, T.; Shimomura, M.; Dai, Z.; Bednarski-Meinke, C.; Golding, B. *New Diamond and Frontier Carbon Technology* **2005**, *15*, 363–371.

(122) Dideikin, A. T.; Eidelman, E. D.; Kidalov, S. V.; Kirilenko, D. A.; Meilakhs, A. P.; Shakhov, F. M.; Shvidchenko, A. V.; Sokolov, V. V.; Babunz, R. A.; Vul, A. Y. *Diamond and Related Materials* **2017**, *75*, 85–90.

(123) Mertens, M.; Lin, I.-N.; Manoharan, D.; Moeinian, A.; Bruehne, K.; Fecht, H. J. *Aip Advances* **2017**, *7*, 015312.

(124) Ershova, A.; Eizenbraun, A. *Materials Research Bulletin* **2012**, *47*, 3681–3690.

(125) Ferrari, A. C.; Robertson, J. *Physical Review B* **2001**, *64*, 075414.

(126) Ferrari, A. C.; Robertson, J. *Philosophical Transactions of the Royal Society of London A: Mathematical, Physical and Engineering Sciences* **2004**, *362*, 2477–2512.

(127) Ferrari, A. C.; Robertson, J. *Physical Review B* **2000**, *61*, 14095–14107.

(128) Casiraghi, C.; Pisana, S.; Novoselov, K. S.; Geim, A. K.; Ferrari, A. C. *Applied Physics Letters* **2007**, *91*, 233108.

(129) Prawer, S.; Nemanich, R. J. *Philosophical Transactions of the Royal Society of London A: Mathematical, Physical and Engineering Sciences* **2004**, *362*, 2537–2565.

(130) Bühlmann, S; Blank, E; Haubner, R; Lux, B *Diamond and Related Materials* **1999**, *8*, 194–201.

(131) Li, D.; Qin, Q. H.; Zuo, D.; Boswell, R. W.; Lu, W.; Stachurski, Z. *Plasma Chemistry and Plasma Processing* **2014**, *34*, 767–784.

(132) Buijnsters, J. G.; Shankar, P.; van Enckevort, W. J. P.; Schermer, J. J.; ter Meulen, J. J. *physica status solidi (a)* **2003**, *195*, 383–395.

(133) Inzoli, F.; Dellasega, D.; Russo, V.; Caniello, R.; Conti, C.; Ghezzi, F.; Passoni, M. *Diamond and Related Materials* **2017**, *74*, 212–221.

(134) Shatynski, S. R. *Oxidation of Metals*, *13*, 105–118.

(135) Sun, X.; Ma, H. T.; Yang, L. Z.; Sanchez-Pasten, M.; Craig Penner, D.; Li, Y. S.; Yang, Q. *Corrosion Science* **2015**, *98*, 619–625.

(136) Passoni, M.; Russo, V.; Dellasega, D.; Causa, F.; Ghezzi, F.; Wolverson, D.; Bottani, C. E. *Journal of Raman Spectroscopy* **2012**, *43*, 884–888.

(137) Nakashima, S.; Harima, H. *physica status solidi (a)* **1997**, *162*, 39–64.

(138) Chen, H.; Nielsen, M.; Gold, C.; Dillon, R.; Digregorio, J.; Furtak, T. *Thin Solid Films* **1992**, *212*, 169–172.

(139) Fayer, A.; Glozman, O.; Hoffman, A. *Applied Physics Letters* **1995**, *67*, 2299–2301.

(140) Varga, M.; Potocky, S.; Tesarek, P.; Babchenko, O.; Davydova, M.; Kromka, A. *Applied Surface Science* **2014**, *312*, 220–225.

(141) Tsugawa, K.; Kawaki, S.; Ishihara, M.; Hasegawa, M. *Japanese Journal of Applied Physics* **2012**, *51*, 090122.

(142) Pimenta, M. A.; Dresselhaus, G.; Dresselhaus, M. S.; Cançado, L. G.; Jorio, A.; Saito, R. *Physical Chemistry Chemical Physics* **2007**, *9*, 1276–1290.

(143) Reina, A.; Jia, X.; Ho, J.; Nezich, D.; Son, H.; Bulovic, V.; Dresselhaus, M. S.; Kong, J. *Nano Letters* **2009**, *9*, 30–35.

(144) Malard, L. M.; Pimenta, M. A.; Dresselhaus, G.; Dresselhaus, M. S. *Physics Reports* **2009**, *473*, 51–87.

(145) Haubner, R.; Rudigier, M. *Physics Procedia* **2013**, *46*, 71–78.

(146) Bogus, A.; Gebeshuber, I. C.; Pauschitz, A.; Roy, M.; Haubner, R. *Diamond and Related Materials* **2008**, *17*, 1998–2004.

(147) Lai, W. C.; Wu, Y.-S.; Chang, H.-C.; Lee, Y.-H. *Applied Surface Science* **2010**, *257*, 1729–1735.

(148) Zhang, J.-Y.; Wang, P.-F.; Ding, S.-J.; Wei Zhang, D.; Wang, J.-T.; Liu, Z.-J. *Thin Solid Films* **2000**, *368*, 266–268.

(149) E. Wilks, J. W., *Properties and Application of Diamond*; Buttherworth Heinneman: 1994, p 137.

(150) Liu, H. M.; Dandy, D. S. *Journal of the Electrochemical Society* **1996**, *143*, 1104–1109.

(151) Ballutaud, D.; Jomard, F.; Kociniewski, T.; Rzepka, E.; Girard, H.; Saada, S. *Diamond and Related Materials* **2008**, *17*, 451–456.

(152) Silva, F.; Gicquel, A.; Tardieu, A.; Cledat, P.; Chauveau, T. *Diamond and Related Materials* **1996**, *5*, 338–344.

(153) Gicquel, A.; Hassouni, K.; Silva, F.; Achard, J. *Current Applied Physics* **2001**, *1*, 479–496.

(154) Williams, O. A.; Hees, J.; Dieker, C.; Jäger, W.; Kirste, L.; Nebel, C. E. *ACS Nano* **2010**, *4*, 4824–4830.

(155) Zani, A.; Dellasega, D.; Russo, V.; Passoni, M. *Carbon* **2013**, *56*, 358–365.

(156) Murray, P. T.; Peeler, D. T. *Journal of Electronic Materials* **1994**, *23*, 855–859.

(157) Yoshitake, T.; Nishiyama, T.; Aoki, H.; Suizu, K.; Takahashi, K.; Nagayama, K. *Diamond and Related Materials* **1999**, *8*, 463–467.

(158) Maffini, A. "Laser cleaning of diagnostic first mirrors for nuclear fusion machines", PhD Thesis, Politecnico di Milano, Ph.D. Program in Nuclear, Energetic Science, and Technologies, 2015.

(159) De Boer, W.; Bol, J.; Furgeri, A.; Müller, S.; Sander, C.; Berdermann, E.; Pomorski, M.; Huhtinen, M. *physica status solidi (a)* **2007**, *204*, 3004–3010.

(160) Hodgson, M.; Lohstroh, A.; J Sellin, P.; J Thomas, D. *Measurement Science and Technology* **2017**, *28*, DOI: `10.1088/1361-6501/aa7f8b`.

(161) Bentele, B.; Cumalat, J. P.; Schaeffer, D.; Wagner, S. R.; Riley, G.; Spanier, S. *Nuclear Instruments and Methods in Physics Research Section A: Accelerators, Spectrometers, Detectors and Associated Equipment* **2016**, *838*, 74–81.

(162) Pillon, M.; Angelone, M.; Aielli, G.; Almaviva, S.; Marinelli, M.; Milani, E.; Prestopino, G.; Tucciarone, A.; Verona, C.; Verona-Rinati, G. *Journal of Applied Physics* **2008**, *104*, 054513.

(163) Oh, A.; Moll, M.; Wagner, A.; Zeuner, W. *Diamond and Related Materials* **2000**, *9*, 1897–1903.

(164) Pietropaolo, A.; Verona Rinati, G.; Verona, C.; Schooneveld, E. M.; Angelone, M.; Pillon, M. *Nuclear Instruments and Methods in Physics Research Section A: Accelerators, Spectrometers, Detectors and Associated Equipment* **2009**, *610*, 677–681.

(165) Giacomelli, L.; Rebai, M.; Fazzi, A.; Cippo, E. P.; Tardocchi, M.; Frost, C. D.; Pietropaolo, A.; Rhodes, N.; Schooneveld, E.; Gorini, G. *Nuclear Instruments & Methods in Physics Research Section a-Accelerators Spectrometers Detectors and Associated Equipment* **2013**, *720*, 125–127.

(166) Rebai, M.; Giacomelli, L.; Andreani, C.; Fazzi, A.; Frost, C. D.; Cippo, E. P.; Pietropaolo, A.; Rhodes, N.; Tardocchi, M.; Schooneveld, E.; Gorini, G. *Journal of Instrumentation* **2012**, *7*, C05015.

(167) Pilotti, R.; Angelone, M.; Marinelli, M.; Milani, E.; Verona-Rinati, G.; Verona, C.; Prestopino, G.; Montereali, R. M.; Vincenti, M. A.; Schooneveld, E. M.; Scherillo, A.; Pietropaolo, A. *EPL (Europhysics Letters)* **2016**, *116*, 42001.

(168) Dilawar, N.; Kapil, R.; Vankar, V. D.; Avasthi, D. K.; Kabiraj, D.; Mehta, G. K. *Thin Solid Films* **1997**, *305*, 88–94.

(169) Kalish, R.; Reznik, A.; Nugent, K. W.; Prawer, S. *Nuclear Instruments and Methods in Physics Research Section B: Beam Interactions with Materials and Atoms* **1999**, *148*, 626–633.

(170) Deslandes, A.; Guenette, M. C.; Corr, C. S.; Karatchevtseva, I.; Thomsen, L.; Lumpkin, G. R.; Riley, D. P. *Nuclear Fusion* **2014**, *54*, 073003.

(171) Jelezko, F.; Wrachtrup, J. *Physica Status Solidi a-Applications and Materials Science* **2006**, *203*, 3207–3225.

(172) Thomsen, C.; Reich, S. *Physical Review Letters* **2000**, *85*, 5214–5217.

(173) Bianco, A.; Cheng, H.-M.; Enoki, T.; Gogotsi, Y.; Hurt, R. H.; Koratkar, N.; Kyotani, T.; Monthioux, M.; Park, C. R.; Tascon, J. M. D.; Zhang, J. *Carbon* **2013**, *65*, 1–6.

(174) Tuinstra, F.; Koenig, J. L. *The Journal of Chemical Physics* **1970**, *53*, 1126–1130.

(175) Casiraghi, C.; Ferrari, A. C.; Robertson, J. *Physical Review B* **2005**, *72*, 085401.

(176) Ferrari, A. C.; Robertson, J. *Physical Review B* **2001**, *63*, 121405.

(177) Kuzmany, H.; Pfeiffer, R.; Salk, N.; Günther, B. *Carbon* **2004**, *42*, 911–917.

(178) Robertson, J. *Physical Review B* **1996**, *53*, 16302–16305.

(179) Calizo, I.; Bejenari, I.; Rahman, M.; Liu, G.; Balandin, A. A. *Journal of Applied Physics* **2009**, *106*, 043509.